A Detector Block-Pairwise Dead Time Correction Method for Improved Quantitation Accuracy for a Dedicated BrainPET Scanner

von

Ahlam Said Mohamad Issa

A Detector Block-Pairwise Dead Time Correction Method for Improved Quantitation Accuracy for a Dedicated BrainPET Scanner

Von der Medizinischen Fakultät der Rheinisch-Westfälischen Technischen Hochschule Aachen zur Erlangung des akademischen Grades einer Doktorin der Theoretischen Medizin genehmigte Dissertation

vorgelegt von

Ahlam Said Mohamad Issa

aus Ramallah (Palästina)

Berichter:

Universitätsprofessor Dr. rer. nat. Nadim Joni Shah

Universitätsprofessor Dr. med. Irene Neuner

Tag der mündlichen Prüfung: 02.11.2023

Diese Dissertation ist auf den Internetseiten der Universitätsbibliothek online verfügbar.

"I dedicate this work to whom I loved…

“It is dedicated to God (In the name of God and praise be to God, Lord of the worlds),

to my mother (for all her love and care),

to my father's soul (whose I miss a lot),

to my brothers (for much love and respect),

to my beloved hometown (free Palestine and glory to the martyrs),

and for you all (who believe in their dreams to the end)”.

Printed with Forschungszentrum Jülich GmbH C-SG
Grafische Medien

Part of the work presented in this dissertation was previously published in Physics in Medicine & Biology, 2022 Phys. Med. Biol. 67 235004, as A detector block-pairwise dead time correction method for improved quantitation with a dedicated BrainPET scanner by Ahlam Said Mohamad Issa, Jürgen Scheins, Lutz Tellmann, Alejandro Lopez-Montes, Joaquin L Herraiz, Cláudia Régio Brambilla, Hans Herzog, Irene Neuner, N Jon Shah and Christoph Lerche.

TABLE OF CONTENTS

LIST OF FIGURES

LIST OF TABLES

LIST OF ABBREVIATIONS

Abbreviation	Definition
[^{11}C]ABP688	3-(6-methyl-pyridin-2-ylethynyl)-cyclohex-2-enone-O-[^{11}C]-methyl-oxime
AC	Attenuation Correction
ACC	Anterior Cingulate Cortex
AIF	Arterial Input Function
AMIDE	A Medical Imaging Data Examiner
APDs	Avalanche Photodiodes
ASL	Arterial Spin Labeling
BGO	Bismuth Germanate ($Bi_4Ge_3O_{12}$)
BLUT	Block Lookup Table
BP_{ND}	Non-displaceable Binding

	Potential
CBF	Cerebral Blow Flow
CBM	Continuous-bed-motion
CFD	Constant Fraction Discriminator
CO_2	Carbon Dioxide
COV	Coefficient of Variation
CPM	Counts Per Minute
CS 27	Cylindrical Source
CT	Computed Tomography
CTV	Clinical Volume
CZT	Cadmium Zinc Telluride
DT	Dead Time
DTC	Dead Time Correction
DTCf	Dead Time Correction Factor
FDG	[^{18}F]-fluoro-deoxyglucose
FET	O-(2-[^{18}F]fluoroethyl)-L-tyrosine
FOV	Field of View
^{68}Ge	Germanium
GAGG	Cerium-doped (Ga, Al)$_5O_{12}$
GM	Gray Matter
^{99}mTc-HMPAO	^{99m}Tc-D-L-

	hexamethylpropylene
	Amine Oxime
ID	Identification
IDH	Isocitrate Dehydrogenase
	Genotype
IDS	Inter-detector Scattered
IF	Input Function
ISO	Isocenter
IV	Fourth
^{176}Lu	Natural Lutetium
LLD	Lower Level Discriminator
LOR	Line of Response
LOS	Lutetium Oxyorthosilicate
LYSO	Cerium Doped Lutetium-based
	(Lu_2SiO_5:Ce)
mGluR5	Metabotropic Glutamate
	Receptor Type 5
MBq	MegaBecquerel
ML	Maximum Likelihood
ML-EM	Maximum-likelihood
	Expectation-maximization
MNI	Montreal Neurological Institute
MR	Magnetic resonance

MRI	Magnetic resonance Imaging
NaI(Tl)	Sodium Iodide
NEMA	National Electrical Manufacturers Association
NP_{DT}	Non-paralyzable Dead Time
NU	three-compartment phantom (NEMA NU 2-994)
3D OP-OSEM	3D Ordinary Poisson Ordered-Subset Expectation Maximization
p.i.	Post injection
pCASL	Pseudo-continuous ASL
PC-PET	Phase-contrast Positron Emission Tomography
P_{DT}	Paralyzable Dead Time
PET	Positron Emission Tomography
PKIN	General Kinetic Modeling Tool
PMT	Photomultiplier Tube
PNEURO	PMOD Neuro Tool
P_P	Prompts fitted with Paralyzable
PTV	Planning Volume
PVE	Partial Volume Effects
PXMOD	Pixel-wise Modeling Tool of

	PMOD
Tx/Rx RF	Transmit–receive Radiofrequency
ROI	Region of Interest
RWTH	Rheinisch-Westfälische Technische Hochschule
SCR	Singles-to-coincidences Ratio
SE	Standard Error
SPECT	Single-photon Emission Computerized Tomography
SSS	Single Scatter Simulation
SUV	Standard Uptake Value
TAC	Time Activity Curve
TBR	Tumor-to-brain Ratio
T1 MPARGE	Longitudinal Relaxation Time Magnetization Prepared – Rapid Gradient Echo
TV	Treated Volume
ULD	Upper Level Discriminator
VOI	Volume of Interest
V_T	Distribution Volume
WHO	World Health Organization
SiPMs	Silicon Photomultipliers

WM	White matter
Z_{eff}	effective atomic number

1. Introduction

1.1 General overview of Positron Emission Tomography (PET)

Positron emission tomography (PET) is considered a significant clinical and preclinical imaging technique in vivo. It has become an established method to measure metabolic tissue functions. PET uses radioactively labeled, metabolic molecules for quantitative in vivo measures of the biochemical and physiological functions. The heart of the PET technique is the radioactive decay and the annihilation process. The positron is emitted when the radioactive atom decays, then the positron annihilates with an electron, thus resulting in the emission of high-energy photons. Tracking the resulting gamma photons from the annihilation is the basis of PET imaging (Cherry & Dahlbom 2006; Khalil 2011; Nuyts 2015). Figure 1.1 shows the general aspects of the beta decay and the annihilation process. PET has many branches of

applications, the main application is the diagnosis in oncology, further, we can find it in the diagnosis of some neurological and psychiatric disorders, receptor binding, metabolism, and quantification of physiologic functions such as cerebral blood flow (Ping et al. 2008; Derlin et al. 2018; Langer 2010; Meyer et al. 2020; Portnow et al. 2013; Sehlin et al. 2019).

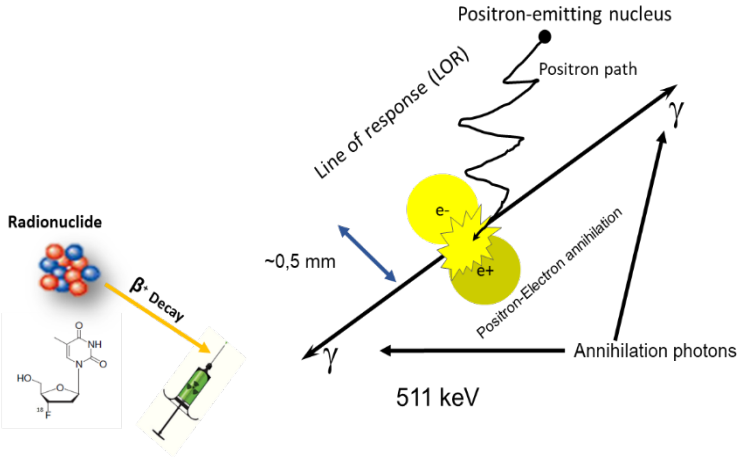

Figure 1. 1 The β+ decay, positron emission and the annihilation process responsible for the production of the two 511 keV gamma photons.

The average positron range in the matter is rather short (see figure 1.1), and it depends on the properties of the matter it is interacting with and the energy of the positron. Different radioactive isotopes are used in PET imaging e.g., ^{18}F, ^{11}C, ^{15}O, etc. Furthermore, the isotopes must be combined with some biological substrates such as water H_2O, CO_2, glucose, and many others according to the target for the PET imaging. Applying the tracer principle, many kinetic studies can be provided using PET scanning (Badawi 2001; Zaidi 2006; Schwaiger & Wester 2011).

1.1.1 Underlying elementary processes

A radioactive isotope is an atom with an unstable nucleus. The unstable nuclei use decay to achieve a more stable state. Different radioactive decay types exist: i.e., gamma decay (γ-decay), alpha decay (α-decay), and beta decay (ß-decay). The positron emission relevant for PET scan is caused by beta plus decay ($ß^+$ decay) (Cherry & Dahlbom 2006;

Khalil 2011; Nuyts 2015; Badawi 2001). During the beta plus decay, the inside the unstable nuclide one proton (p) transforms into a neutron (n) and emits a positron (positively charged electron e^{+}) and a neutrino (ν): "$p \rightarrow n + \beta^{+} + \nu$" (Cherry & Dahlbom 2006; Khalil 2011; Nuyts 2015). The activity is defined as the total number of decays per unit time (normally one second), The radioactive decay process is a random process following an exponential law, where the half-life of the nuclide is defined as the time interval in which the activity reaches half of the initial activity. These aspects are described by equation 1.1 below (Bailey & Humm 2014):

$$A(t) = A(t_0)e^{-\lambda t}$$

$$\text{with} \quad \lambda = \frac{ln2}{t_{1/2}}, \qquad (1.1)$$

where $A(t)$ is the activity which is left at a certain time t , $A(t_0)$ is the initial activity at the time t_0, and λ is the decay constant which is indirect proportional to the half-life, and $t_{1/2}$ is the half-life. (Bailey & Humm 2014; Cherry & Dahlbom 2006).

The positron range in solid and liquid matter is rather short, and there are several different ways the positrons interact with matter. The four main interaction types of the positron are Bremsstrahlung, ionization, inelastic scattering, multiple elastic scattering (Rutherford scattering), and annihilation, where annihilation is the relevant interaction that enables the PET imaging principle (Bailey & Humm 2014; Cherry & Dahlbom 2006). Before the positron annihilates, in general it forms a bound state with the electron, called positronium. Positronium has a short lifetime of approximately 100 ns in gases, 100 ps in metals, and values in around 1.9 ns depending on the chemical environment e.g., oxygen concentration (pO_2) (Shibuya et al. 2020; Zgardzińska et al. 2020; Schwarz et al. 2019). In the annihilation process, all the energy of the combined positron electron pair is converted into radiation (Khalil 2011; Nuyts 2015; Badawi 2001).

In the annihilation process, both positron and electron convert their mass into energy and produce a pair of two gamma photons of 511 keV energy

which are traveling in opposite directions (see figure 1.1), and whose energy is given through Einstein's mass-energy equivalence equation 1.2 bellow (Bailey & Humm 2014; Cherry & Dahlbom 2006):

$$E = mc^2, \qquad (1.2)$$

Here, m is the mass of the charged particle, and c is the speed of light in vacuum.

According to the conversation of momentum, the resulting gamma photons of the annihilation process are emitted in opposite directions in the frame of reference where the positronium is at rest. As the positronium has in general a non-vanishing momentum in the observer's frame of reference, there is a small residual non-collinearity, i.e. the angle between the travel directions of the two gamma photons differ by approximately 0.5° from the 180° (Nuyts 2015; Knoll 2010).

1.1.2 Detector and Components

Scintillation is the most widely used process for gamma photon detection in the PET scanner. The scintillation block detectors are used for photon detection in the PET detector. During the photon detection, the photon is stopped and the energy transferred by the photons to the block detector is measured.

A scintillation block detector for PET consist of an inorganic scintillation crystal attached to a photodetector, that interact with incident high-energy photons (511 keV), and emit visible or near-ultraviolet light. The total number of scintillation photons is proportional to the amount of energy that is deposited by the gamma photon inside the crystal (Bailey & Humm 2014; Cherry & Dahlbom 2006). Four types of sensor technology (photodetector) are used in PET systems: The photomultiplier tube (PMTs) has been used in previous generations of PET detectors, avalanche photodiodes (APDs) which are used some PET systems, and the silicon photomultipliers (SiPMs) which is used in newer

generations of PET systems. In addition to the scintillation detector, there are also semiconducting particle detectors as cadmium zinc telluride (CZT) which are still subjected to research and development (Jiang et al. 2019; Del Guerra et al. 2009; Grazioso et al. 2006; Acerbi & Gundacker 2019). The photodetector turns the incoming light into an electrical pulse. The PET data acquisition depends on the detection of the two γ photons, which requires the addition of coincidence circuits, which are used to identify the temporally coincident pulses from all detected events (Cherry & Dahlbom 2006; Khalil 2011; Nuyts 2015).

The main characteristics of the scintillation crystal are crucial for the relevant performance parameters of PET, e.g., sensitivity, coincidence timing resolution, energy resolution and spatial resolution. One of these characteristics is the decay constant, which determines the length of the scintillation flash in the crystal. Shorter decay constants are preferable for commercial PET scintillation crystals since they allow a higher counting rate and better coincidence

timing resolution. The stopping power in the medium depends on the energy and the charge of the particles and the density and the effective atomic number Z_{eff} of the medium (El-Ghossain, 2017). High effective atomic numbers paired with high density are desirable, as they lead to shorter travel distances which results in a high efficiency of event detection. Alternatively, the scintillation crystals can be made thicker. Furthermore, good energy resolution improves the differentiation between photons resulting from Compton scattered events and unscattered events. The scintillation crystals should also have a high light output for best spatial, timing, and energy resolution (Khalil 2011; Nuyts 2015). The most common scintillator crystal materials used in PET are: NaI(Tl), which was used in the first PET designs in 1972; $Bi_4Ge_3O_{12}$ (BGO), Lu_2SiO_5:Ce (LYSO) and Lu_2SiO_5 (LSO), which are the with a high density currently used in PET. $Gd_3(Ga, Al)_5O_{12}$ (GAGG) is a promising material for future PET designs as it combines lower price with high performance (Yu et al. 2022; Nuyts 2015; Bailey & Humm 2014; Cherry & Dahlbom 2006).

In the case of LSO and LYSO, one of the main components contains a natural radioactive isotope, which is lutetium. Natural lutetium contains around 2.6% of ^{176}Lu which decays via beta and subsequent gamma decay to the ground state ^{176}Hf. The half-life of ^{176}Lu is $\approx (3.56 \pm 0.07) \times 10^{10}$ years (Kossert et al. 2013; Nir-El & Lavi 1998), thus resulting in a constant background signal in the PET system. This intrinsic radioactivity can affect PET images directly and indirectly, especially in the case of using wide energy windows and at low injected activity levels, as the combined beta and gamma decay can lead to spurious coincidences too (Alva-Sánchez et al. 2018; Wang et al. 2020).

In the photodetector, the incoming light photons generate initial electro-hole pairs. They are amplified via the avalanche principle, thus creating an electric current. The produced current is proportional to the energy deposited by the gamma photons in the scintillation crystal. The block detector is the common setup of a scintillation detector for a PET scanner. Block detectors are

detection units consisting of several photodetectors and several scintillation crystal pixels, and each PET scanner has normally several block detectors. The block detector design allows to determine the interaction position of the annihilation photons inside the block detector by analyzing the spatial distribution of the scintillation photons (Nuyts 2015; Bailey & Humm 2014). Further, the PET scanner has normally a cylindrical shape build by rings of block detectors, which are faced with the scintillator side towards the imaged object. The field of view (FOV) in human scanners is typically 70 cm in diameter and around 15-25 cm in axial direction, the FOV is the area inside the detector cylinder which can be imaged by PET system.

1.1.3 Interaction of Photons with Matter

In nuclear medicine, the photon emissions can be used for diagnostic imaging, as gamma radiation can penetrate easily dense matter and because of the rather low energy of photons used for medical imaging ranges roughly from 60-600keV, which allows a for a sufficiently high detection

efficiency. In contrary, alpha and beta radiation cannot be used for in-vivo imaging in humans, as they are absorbed in the matter after a very short path before it can be detected. (Nuyts 2015; Knoll 2010). The 511 keV photons interact with matter in several different ways, but only two are relevant in PET imaging. The first one is photoelectric absorption which is the transfer of complete energy of the photon to the hit electron and the gamma disappears. In contrast, in a Compton interaction, the photon interacts with the electron and transfers only some of its energy to the electron and leaves the collision with the difference of energy (Nuyts 2015; Knoll 2010). In this case, the target electron recoils according to the principle of conservation of momentum in a different direction. As a consequence, Compton scattering in nuclear medicine imaging results in erroneous detected events, because with the current state of the art it is impossible to reconstruct the correct trajectory of the scattered photon. Therefore, a scattering correction has to be applied in PET imaging to minimize the image

noise introduced by the scattered radiation (Bailey & Humm 2014; Cherry & Dahlbom 2006; Nuyts 2015; Knoll 2010). The probability of the photoelectric effect is higher in high-density materials while the probability of Compton scatter is higher in light materials. Therefore, Compton scatter is the dominant annihilation photon interaction in human tissue and it is the dominant process that leads to an attenuation of the annihilation photons creating photons with a lower average energy (Nuyts 2015; Knoll 2010). Unfortunately, the possibilities for discrimination and filtering of Compton scattered photons is very limited with the current state of the art.

1.1.4 Types of Coincidences and their Detection

Coincidence detection is the observation of the pair of gamma photons arriving roughly at the same time at two detectors of the PET detector ring. Coincidence detection of the two 511keV gamma photons, which result from the annihilation process,

is crucial for PET. The photon pair is detected within a short time window, called the coincidence window (Kolinge et al. 2021; Wang et al. 2022), e.g., for the Siemens 3T MR BrainPET insert. this window is set to 12 ns. The long straight-line between the two block detectors is called the line of response (LOR) and, in case of a true coincidence event, the annihilation must have taken place on this line. Figure 1.2 shows a schematic drawing of a PET scanner with cylindrical arrangement of gamma detectors, the object and some LORs. The coincident events which are formed by two singles and occurring within the coincidence window are called prompts. Figure 1.3 illustrates the different types of detected events, i.e. true coincidences (“trues”) random coincidences ("randoms”), scattered coincidences ("scatter”), single events ("singles”), multiple coincidences ("multiples”), and detector scattered coincidence events. Random coincidences are registered when two unrelated gamma photons (they originate from two different annihilations) are detected by the detector pair within the same coincidence time window. If uncorrected, random

events have an important effect on the image contrast since they rise the background in the image and thus lower the image contrast. Scatter coincidences raise due to Compton scattering of the 511 keV photons in the matter and the caused change of its flight direction paired with some loss of energy. Single events carry less information and multiple coincidences occurs when three or more photons are detected simultaneously. Normally, singles are discarded due to the ambiguity of the position of their origin. The non-validated singles are those events that pass the constant fraction discriminator (CFD) without estimating the position (scintillation pixel) in the block and which are not energy filtered, i.e., these events are counted always when the CFD was triggered, see 4.1.1 in the results chapter (Ullisch, and Moses 2007; Weirich et al. 2013). In contrast, the validated singles cases are energy filtered according to the energy window their position (scintillation pixel) in the block was estimated. Triples can present a significant amount of registered events in PET acquisition (Cal-González et al. 2014; Lage et al. 2015). Triple

coincidences take place when three photons are detected within the same coincidence time window and within the energy window. There are four cases which can lead to triples in the PET acquisition, figure 1.4 summarizes the four types of triples. First, in case of nuclides that decay via combined β+ and γ decay, the detection in one coincidence of the two annihilation γ photons and an additional prompt γ photon. Second, triples formed as random events from two different β+ disintegrations, and finally, triples formed by inter-detector scattered events (IDS) (see figure 1.4) (Cal-González et al. 2014). There are PET scanners, which process the three photons as a set of double coincidences thus resulting in increased image noise and quantification bias. The image noise and bias due to uncorrected triples can be introduced directly and indirectly in the data correction steps, e.g., random coincidence correction and dead time correction. True coincidence are coincidences formed by a pair of the 511 keV photons from the same annihilation which are both detected by a pair of block detectors. (Nuyts 2015; Cherry & Dahlbom 2006).

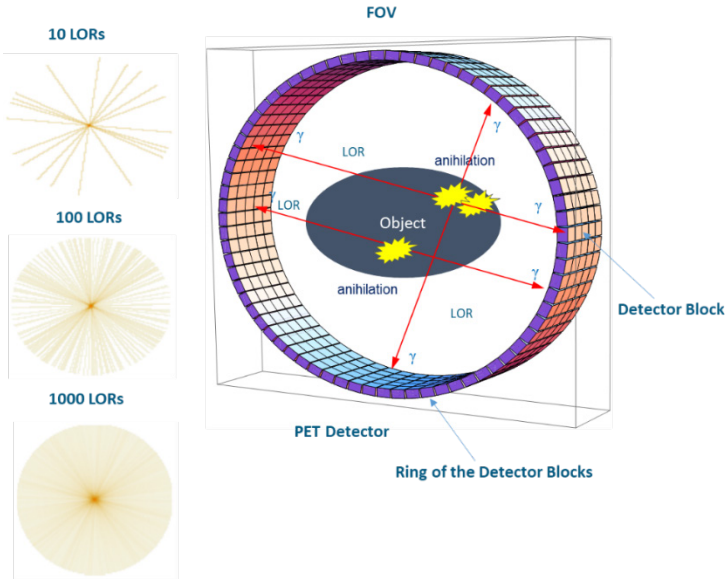

Figure 1.2 Right: Scintillation detectors arranged in a cylinder to build a PET scanner together with the object and the LORs in the FOV. Left: Visualization of the accumulation of LORs in the FOV, which can be binned into sinograms or which are directly used for image reconstruction in PET.

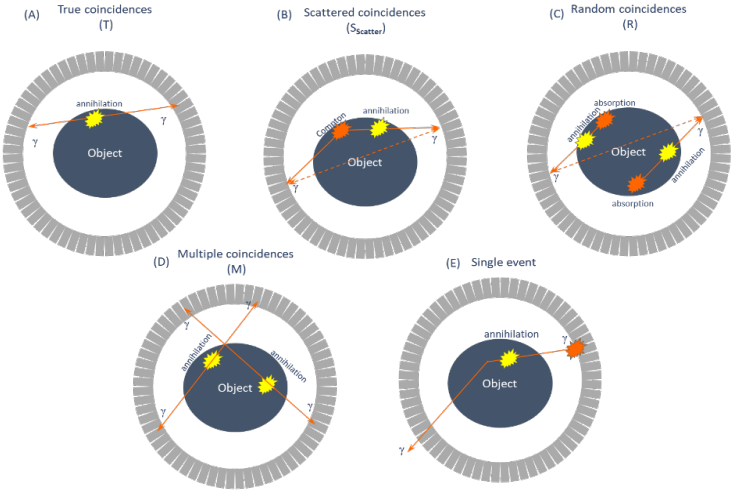

Figure 1.3 The different event types in PET: (A)Trues, (B)Scattered, (C) Randoms, (D) Multiples and (E) Singles.

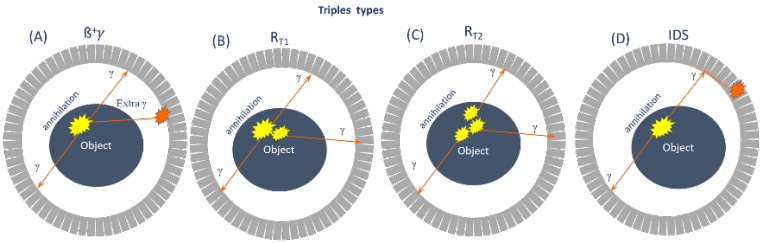

Figure 1.4 The four types of triples:(A) detect both annihilation γ and the prompt γ , (B and C) triples of random events from two different disintegrations, (D) inter-detector scattered events (IDS).

1.2 Quantitative PET images and PET Tracers

PET imaging is an important tool for diagnosis and quantitative analysis of tissue metabolism, as well as for studying the brain's normal vs abnormal physiological activities, cardiac research, and oncology. Quantitative PET imaging refers to acquired images to extract underlying metabolic or physiological parameters as inflow rates, excretion rates, and many others. Most often kinetic modeling and imaging at equilibrium conditions are used for the extraction of these metabolic parameters. For this, PET imaging studies use a bolus injection of the radiotracer followed by a constant infusion (i.e. the bolus-infusion scheme) while simultaneously running the data acquisition. In these studies, the equilibrium is estimated by adjusting the bolus-infusion scheme in order to reach a stable plateau for the distribution volume V_T in the regions of interest (Régio Brambilla et al. 2020; Brambilla et al. 2021; Régio Brambilla et al. 2022; Logan 2001). Figure 1.5 shows different quantitative PET images.

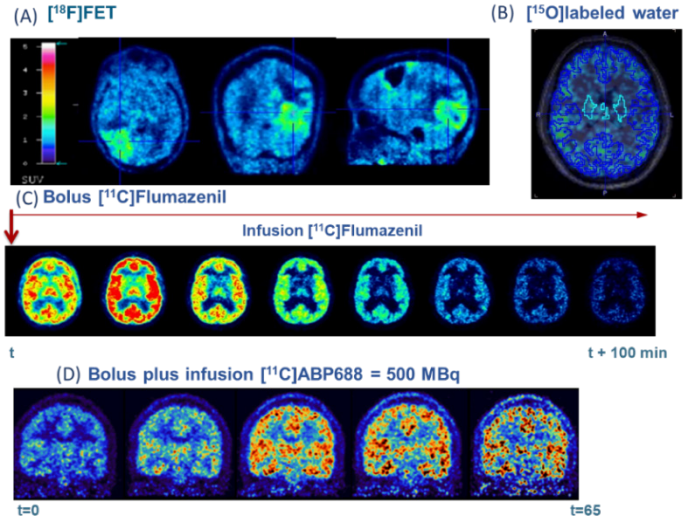

Figure 1.5 Different quantitative and pseudo-quantitative PET images. (A) Summed images from 20-40 minutes of [^{18}F]-FET-PET measurements in SUV units. (B) Image showing the a activity concentration kBq/cm^3 of [^{15}O]H_2O measurement with regions for gray matter (blue lines), and white matter (turquoise lines). (C) Images of dynamic [^{11}C]Flumanzenial measurements using a bolus-infusion protocol. Shown an activity concentration in kBq/cm^3. (D) Images of dynamic [^{11}C]ABP688 measurements using a bolus-infusion protocol. Shown quantity of activity concentration in kBq/cm^3. Adapted from (Régio Brambilla et al. 2022) & (Issa et al. 2023).

However, true quantification as kinetic modelling is very challenging and often require blood sampling, which is not practical in clinical routine. Often, the observation of the differences in radiotracer uptake is enough to obtain diagnostic information. In figure 1.6, an example of the semi-quantitative PET image of [^{18}F]-fluoro-deoxyglucose (FDG) in Alzheimer's disease is shown (Herzog et al. 2018). The lack of FDG uptake in the occipitotemporal cortex is the mainly relevant observation in this case. The correct estimation of the radioactivity concentration in target tissues is normally not sufficient, as injected activity and patient size and weight may differ. In order to correct for these variations in a simple manner, the standard uptake value (SUV) was defined to semi-quantitatively measuring the uptake of the radioactive tracers in the organ or region of interest and to relate it to the injected dose of the radioactive tracer and the volume of the body in which it is distributed (Herzog et al. 2018; Thie 2004; Fletcher & Kinahan 2010).

The SUV is defined as in equation 1.3:

$$SUV = \frac{C}{A/W} \qquad (1.3)$$

Here, C is the radioactivity concentration in the target organ or region in kBq mL^{-1}, A is the total injected activity in (MBq), and W is the body weight in kg (Herzog et al. 2018; Thie 2004; Fletcher & Kinahan 2010).

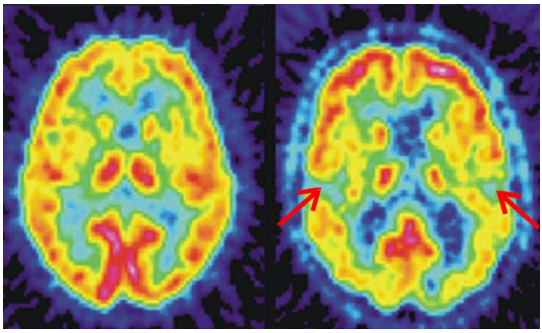

Figure 1.6 Quantitative brain PET image with [^{18}F]-fluoro-deoxyglucose (FDG). Left: for healthy volunteer, right: for Alzheimer's patient. The red arrows indicate the areas of loss of the neurons in the occipitotemporal cortex (Herzog et al. 2018).

For being able to correctly observe the physiological and metabolic functions of the region, organ or tissue of interest, the technical measurement process should not influence these measurements. Further, any required data corrections, e.g., random coincidence correction, dead time correction, etc. should not lead to and disturbance of the measured quantity.

Nuclear imaging as PET is based on the tracer principle, which allows to image the distribution biologically active substance by tagging it radioactively. The amount of the administered radioactive tracer is large enough, so the measured spatial and temporal distribution in the object reflects the functions and/or metabolism of the organs, but it is low enough, to not alter these functions. Various types of PET-radiopharmaceuticals have been developed to image specific biologic functions based on the underlying biochemistry and physiology (Badawi 2001; Zaidi 2006; Schwaiger & Wester 2011). Table 1.1 summarizes some common and uncommon PET-

radiopharmaceuticals together with their corresponding functions (Herzog et al. 2018).

The evaluation of quantitative PET images for obtaining information metabolic function requires further steps in addition to measuring the bio distribution (spatial distribution of the radiopharmaceuticals) and the activity concentration within the target, i.e., the region of interest (ROI). First, the activity concentration in full blood or in the blood plasma must be measured using sampling of arterial blood or sampling of arterialized venous blood. The time course of activity concentration in the blood or blood plasma[1] is called the arterial input function (AIF) or short input function (IF). As blood sampling is challenging and atrial punctuation involves a serious risk for the volunteer, often the image derived AIF is used (ID-AIF).

[1] Blood plasma must be used, when the blood cells themselves show significant uptake of the tracer, for instance in the case of FDG.

Table 1.1 Some PET-radiopharmaceuticals and their corresponding targets adapted from Herzog et al. 2018.

PET-radiopharmaceutical	Function
[^{18}F]-fluoro-deoxyglucose	Glucose consumption
[^{15}O]-water	Perfusion
[^{15}O]-oxygen	Oxygen consumption
[^{15}O]-carbon monoxide	Blood volume
[^{11}C]-raclopride	Binding potential to and density of dopamine receptors
[^{11}C]-flumazenil	Binding potential to and density of benzodiazepine receptors
[^{18}F]-FET	Amino acid uptake
[^{18}F]-altanserin	Binding potential to and density of serotonin receptors
[^{11}C]-ABP688	Binding potential to and density of Metabotropic glutamate receptors subtype 5 ($mGluR_5$) receptors

Second, the radioactive tracer is subjected also to metabolization within the living subject. In some cases, the metabolites resulting from the metabolization of the tracer are radioactive, but do not longer fulfill the function of the tracer and lead to unspecific uptake. In this case, the measured activity concentration with must be corrected for this effect (Herzog et al. 2018).

1.3 Data Corrections in PET

The data acquisition for PET is not perfect and needs to be corrected for different inherent physical effects, i.e., the emitted photons are attenuated in the object, and the gamma photons may be scattered while flying through the matter. Further, the PET detector elements have different detection efficiency, thus leading to different count rates and random and scattered events are recorded together with the true coincidence events. All those effects need to be corrected in order to have accurate quantitative information. In the following, the most

relevant PET data corrections are listed (Scheins et al. 2018):

- Attenuation Correction (AC): The gamma photons are attenuated inside the biological tissues when they traverse the object for subject. As total tissue thickness can be considerable, the fraction of attenuated gammas can be important, especially in human imaging, which has to be corrected for. Otherwise, it will introduce significant image bias. The attenuation is a combination of photoelectric absorption and Compton scattering. (Scheins et al. 2018; Zaidi et al. 2007). If the PET images are reconstructed without AC, deep regions will show a negative bias in the reconstructed activity concentration, e.g. the lung which appears with less uptake in the whole-body PET scan than it really has. (Zaidi et al. 2007). The attenuation coefficient along a path L_j is given by 1.4 (Scheins et al. 2018):

$$a_j = 1 - e^{-\int_{L_j} \mu(l)dl} \qquad (1.4)$$

Here, a_j is the attenuation coefficient, $\mu(l)$ is the spatially dependent linear attenuation coefficient in units of cm^{-1} along the LOR j. L_j is the traveled path of the photon. There are two main factors the attenuation coefficient depends on i.e., the energy of the photons and the local electron density inside the object. Tissue with higher density results in a more elevated attenuation fraction (Scheins et al. 2018; Zaidi et al. 2007). Each of the both annihilation gamma photons have generally a different path for attenuation. However, the combined attenuation coefficient for both annihilation gammas on each LOR is equivalent to the attenuation coefficient for a single photon with the same energy and the sum of the two travel distances of the individual photons. To correct the PET images for the attenuation, the a_j for all LORs must be known. Normally, an attenuation map is provided, that contains the information $\mu(l)$ for

all voxels and which allows to compute the a_j for all LORs.

- Scatter Correction: One of the significant sources for bias in quantitative PET images is Compton scattering. Compton scattering affects the gamma photons by changing their direction, leading in consequence to an erroneous LOR and wrong reconstructed source of the annihilation. Compton scattering results in a decrease of the contrast in the reconstructed PET image. The energy of the scattered photon can be computed with equation 1.5 (Scheins et al. 2018):

$$\bar{E} = \frac{E}{1+\frac{E}{m_0 c^2}(1-\cos\theta)} \qquad (1.5)$$

Here, E is the initial photon energy, θ is the scatter angle and the $m_0 c^2$ is the rest energy of the electron. An energy window (two energy discriminators) is used to reject Compton scattered photons depending on their energy. The scatter fraction (ratio of the number of

scattered events to the total events) was found to be around 40% in brain PET imaging and 50% in whole-body PET. Therefore, scatter correction is considered a significant data correction in PET (Scheins et al. 2018; Bailey & Humm 2014). The Single Scatter Simulation (SSS) algorithm is a fast 3D simulation, that is used to estimate the expected scattered events for each LOR formed by the corresponding true coincidence without scattering (Scheins et al. 2018). The probability of Compton scattering of a photon can be computed for the corresponding energies with the Klein–Nishina formula (Scheins et al. 2018).

- Detector Normalization: Due to the geometry of the PET detector and production tolerances of the components, the detection sensitivity of the scintillation detector block pixels varies over the entire PET ring, depending largely on the angle and the physical position of each scintillator pixel. This results in inhomogeneous LOR detection efficiencies.

The procedure to correct these sensitivity variations is called normalization (Scheins et al. 2018; Theodorakis et al. 2013).

- Random Correction: The coincidences are called true coincidences if the two gamma photons detected in the pair of block detectors are from the same annihilation. Annihilation photons form different decays can be recorded, if their difference in the arrival times is smaller than the coincidence time window. These events are called random coincidences and normally, the fraction of detected randoms is relevant. Randoms lead to reduced image contrast, however, with a good coincidence time resolution, the random coincidence rate can be kept low (Scheins et al. 2018; Brasse et al. 2005). The amount of expected random coincidences can be estimated for each LOR from the singles rates using equation 1.6 (Scheins et al. 2018; Brasse et al. 2005).

$$R_{AB} \approx 2\tau S_A S_B \qquad (1.6)$$

Here, τ is the coincidence time window and S_A, S_B are the single event rates for each block

detector (Scheins et al. 2018; Brasse et al. 2005).

Patient Motion Correction: The voluntary and involuntary motion is another important effect in medical imaging deteriorating the image quality. Increased acquisition time in medical imaging increases the chances for patient motion. The motion artifact can affect the physical correlations between the subject and the detection position within the block detector thus creating an error in the emission image. Therefore, mismatches arise between the subject and the attenuation map in case the map refers to a single and fixed reference position. When correcting for motion, the sensitivity of the LORs is also mismatched, affected, since the normalization was done with a phantom at rest, having therefore a unique relationship between the source and the pair of block detectors. In order to account for this effect, image based motion corrections methods estimate an effective normalization factor, while other methods avoid this effect by

directly correcting the LORs. (Scheins et al. 2018; Catana 2015).

- Decay Correction: Typical PET data acquisitions need more than a half-life of the used radiotracer. As the radiotracer molecules decays, the detected counts are reduced due to this radioactive decay. However, this change in the count rate is not due to the imaged metabolic or physiologic effect and the measured activity concentrations have to be corrected for this loss. The surviving fraction of radioactive tracer molecules is given by equation 1.1. (Scheins et al. 2018; Chen et al. 1995). Equation 1.7 shows the effective decay correction factor D_{eff} derived from equation 1.1 (Scheins et al. 2018):

$$\mathrm{D}_{eff}\,(t_0, \Delta t) = D(t) \cdot \frac{(1-e^{-\alpha})}{\alpha}$$

$$\text{with } \alpha = \ln 2 \cdot \frac{\Delta t}{T_{1/2}} \qquad (1.7)$$

Here, $D(t)$ is the decay correction factor dependent on the time, $T_{1/2}$ is the half- life of

the radioactive tracer. t_0 is the starting time for a frame in the total period of time Δt. The decay correction factor is applied for each image frame.

- Detector Calibration: In addition to all the above mentioned corrections, the PET must be calibrated on regular basis. The calibration has to be done in order to keep all relevant operational parameters and measured values as arrival times and photon energy and photo conversion position within acceptable tolerances (Scheins et al. 2018).
- Dead time Correction (DTC) & Pile up Correction: Dead time (DT) is the time the system needs to process the events. During this period, the system is not able to detect or process another event. DT leads to a loss in the count rate which affects the accuracy of the image by introducing a bias and it increases the noise in the image. The DT losses must be corrected by applying a suitable DT correction, see section (1.4).

As the count rate increases, there is also a higher chance that two scintillation events pile up in the detector and consequently are mispositioned. That is, two events are detected at the same time and the estimated photoconversion position is not correct, i.e. the event is registered in the wrong pixel of the PET detector. Those events are called pileup events. Pileup leads to a loss of spatial resolution and to image artifacts (Vicente et al. 2011; Vicente et al. 2008)

The work in this dissertation focusses on improving the dead time correction (DTC) for an improved quantitation with a dedicated BrainPET Scanner.

1.4 Dead Time Definition

The limitation of the system's capacity of processing is called dead time (τ). If two photons arrive within the same resolving time of the detector, the electronics will detect both as a single event. This

results in not counting one of those events and, due to pile-up, leads to mispositioned events (Cherry & Dahlbom 2006; Nuyts 2015; Bailey & Humm 2014; Khalil 2011). The average losses increase with higher activity and higher count rates. For that, the results of the measured trues are lower than the expected ideal true count rates in the PET system. In this context, it is important to mention that photon counting is a random process whose probability distribution is the Poisson distribution. Due to this random behavior of the radioactive decay, it is not possible to measure the average count rate. Every measurement will only reveal one specific random outcome out of all possible outcomes. Figure 1.7 shows the expected measurement of the true count rate subjected to dead time of 200 ns compared to the ideal true count rates for a typical range of count rages. Figure 1.8 shows the expected measurement of the true count rate subjected to dead time of 1 μs compared to the ideal true count rates.

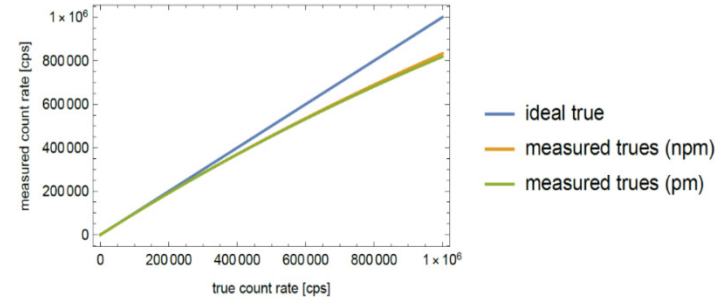

Figure 1.7 Expected measured true count rates for a block dead time of 200 ns compared to the ideal true count rates. The blue line shows the ideal trues and the green and orange line shows the expected measured trues for the non-pralyzable model and the paralyzable model, respectively.

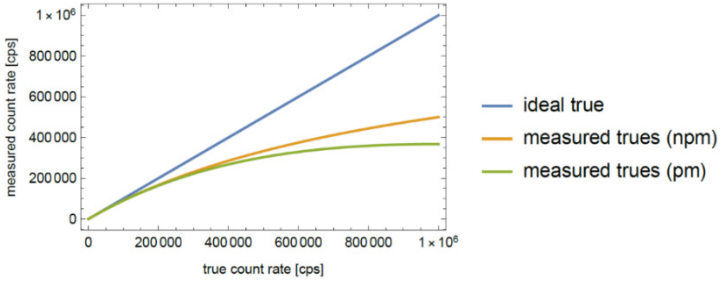

Figure 1.8 As figure 1.7, but with a DT of 1µs.

The DT has different sources which can be grouped into two types: the paralyzable model and the non-paralyzable model. In general, the main source for DT PET systems is the processing of each individual

event in the front-end detector electronics. Here, the DT is generated by the signal integration, which is required to collect the entire scintillation light pulse. Normally, the integration time is set to 3 to 4 times the value of the scintillation decay time constant, i.e., 120-160 ns for the LSO (Cherry & Dahlbom 2006; Nuyts 2015; Bailey & Humm 2014; Khalil 2011; Patil 2010). Consequently, slower scintillators as BGO have a larger dead time. There are different possible DT behaviors depending on the underlying detector or data processing technology. The most common models used to describe the DT behavior are the following:

- Paralyzable DT: Also called extendable dead time model. In this model, the system is unable to generate an output pulse for the second arriving photon, unless the dead time of the detector for processing events (τ) is equal or smaller than to the time interval between the arriving photons. In the paralyzable model, the resolving time extends by τ when the second event occurs before the processing of the

preceding events is finalized. During this period, the system is paralyzed for a time interval, until the detector is recharged. For Poisson processes, distribution of the time intervals between events is given by the exponential distribution $e^{-n\tau}$, where n is the average count rate of arriving events per unit of time. Equation 1.8 gives the expression of the expected measured events (m), which is the product of the true average count rates and the exponential distribution (Cherry & Dahlbom 2006; Nuyts 2015; Bailey & Humm 2014; Patil 2010):

$$m = n\, e^{-n\,\tau} \qquad (1.8)$$

- Non-paralyzable DT: Also called non-extendable dead time model. In this model, the dead time is not affected by events that occur within the DT (τ) of the detector as it is in the paralyzable model. Here, the system is unresponsive for a fixed period of time τ after each arriving event. If the expected measured events rate is m, the total fraction of time during

which the detector is unresponsive, is given by $m\tau$ while the fraction of time in which the system is sensitive is given by $1 - m\,\tau$. Thus, the number of true events n is related to the number of events which can be measured by equation 1.9 (Cherry & Dahlbom 2006; Nuyts 2015; Bailey & Humm 2014; Patil 2010):

$$n = \frac{m}{1-m\,\tau} \qquad (1.9)$$

- Generalized DT: The third model is a hybrid DT model, i.e. a combination of the two previous both models (Müller 1991; Takacs 1958; Albert & Nelson 1953; Usman & Patil 2018). This model is based on the probability θ of the detector system getting paralyzed, where θ can vary from zero to one. θ is the fraction of all events which are able to trigger an extension of the detector paralysation by the interval τ. The generalized model becomes the paralyzable model in the limit, when θ becomes one, while it becomes the non-paralyzable model when θ equals zero. The expected measured counts m for the generalized DT model are given by 1.10

(Müller 1991; Takacs 1958; Albert & Nelson 1953; Usman & Patil 2018):

$$m = \frac{n\theta}{e^{\theta n\tau} + \theta - 1} \qquad (1.10)$$

Here, τ is the generalized DT, n is number of the arriving events. The hybrid model can be further extended by using the two independent dead times for the two behaviors (Lee & Gardner 2000). In this case, m is given by 1.11:

$$m = \frac{n\, exp(-n\tau_p)}{n\tau_n + 1} \qquad (1.11)$$

Here, τ_p is the paralyzable DT, τ_n is the non-paralyzable. Patil & Usman acquired two parameters, i.e., the paralysis factor and the DT using graphical method with this generalized model and by using the data from a fast-decaying source. It is referred to as the original Takacs equation (Patil & Usman 2009; Takacs 1958; Albert & Nelson 1953) with a simple modification shown in equation 1.12:

$$m = \frac{n\, exp(-n\tau\, ∫)}{1 + n\tau\,(1 - ∫)} \qquad (1.12)$$

Here, ∫ is the paralysis factor (probability of paralyzing the system). Hasegawa et. al. defined a technique to measure the higher count rates based on the system clock (Hasegawa et al. 2004). As some parts of typical data acquisition systems process the data using a fixed system clock, in this case, the system is able to measure more counts than in the non- paralyzable model. They proposed equation 1.13 for the expected measurement (Hasegawa et al. 2004):

$$m = \frac{1 - exp(-\tau_{\text{clock}} n)}{\tau_{\text{clock}}} \qquad (1.13)$$

Here, τ_{clock} is the period of the system clock which is chosen to be similar to the detector DT. This model accounts for data buffering in the acquisition chain and was found to better fit to the behavior of positron emission tomography scanners. Figure 1.9 shows behavior of the paralyzable and non-paralyzable DT models with fixed DT for a series of incoming input signals.

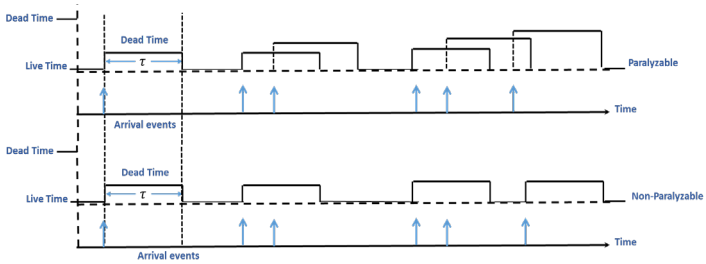

Figure 1.9 Behavior of paralyzable and non-paralyzable DT models with fixed DT for a series of incoming input signals. τ is the dead time and the blue arrows indicate the arrival times of the incoming events.

As seen in this figure, the paralyzable model has an extendable behavior and is able to resolve only three events out of the six arriving events. In contrast, the non-paralyzable has no extendable behavior and is able resolve four events out of six arriving events. Figure 1.10 compares the behavior of the paralyzable model, the non-paralyzable model, and the ideal behavior for a large range of input count rates. At low count rates, both models lead essentially to the same expected measured event rates and show almost identical behavior, while for

higher count rates, the behavior is very different. For the paralyzable model, the count loss is much higher than in the non-paralyzable model, especially for high count rates (Müller 1991; Takacs 1958; Albert & Nelson 1953; Usman & Patil 2018). Importantly, the paralyzable model cannot record any counts in the limit of very high count rates, since the DT keeps continuously extending. In contrast, the non-paralyzable model continues recording incoming events and reaches a saturation count rate which is larger than zero in the asymptotic limit. As shown in figure 1.10, the non-paralyzable model approaches asymptotically the saturation count rate equal to $1/\tau$. Whereas for the paralyzable model, a maximum value for the measured count rate equal to $1/(\tau \cdot e)$ is reached, if the input count rate is equal to $1/\tau$. Furthermore, in the paralyzable model, it is possible to obtain same measured rate for two different values of true event rates (Müller 1991; Takacs 1958; Albert & Nelson 1953; Usman & Patil 2018).

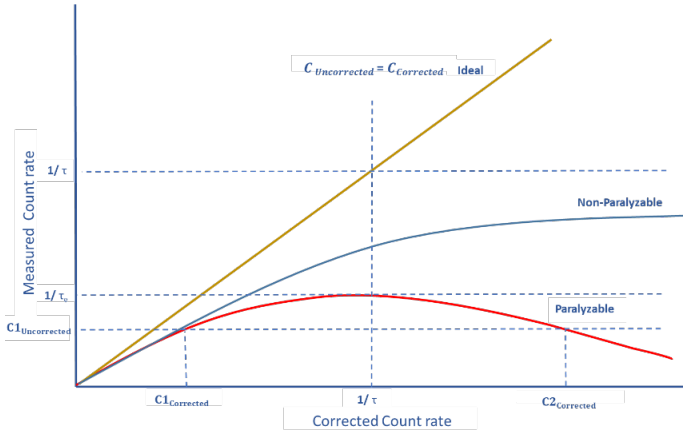

Figure 1.10 Comparison of the behaviors of the ideal case, the paralyzable model, and the non - paralyzable model for a range of count rates. The blue line represents the non - paralyzable model, the red line represents the paralyzable model, and the yellow line represents the ideal behavior. C is the count rate, τ is the DT, and e is the Euler constant.

In real imaging systems for nuclear medicine, the DT behavior is a mixture of the paralyzable and the non - paralyzable models, since some components have a non-paralyzable behavior while others have a paralyzable behavior. That is, the design of the

radiation detector, the design of the analog front-end electronics and analog and digital pulse processing and coincidence procession circuities will affect the DT of the entire system. The amount of DT losses depends on the single event rates which are seen by the individual scintillation detectors of the PET scanner. The radioisotope also affects the amount of DT losses, since the DT is caused by all emitted gamma photons which interact with the detector, not only by those, that pass the energy window (Müller 1991; Takacs 1958; Albert & Nelson 1953; Usman & Patil 2018).

1.4.1 DT Sources

Several components of PET scanners can contribute to DT losses. i.e., the scintillation detector, the electronics which processes the detector signals, and the analog-digital conversion, the data acquisition system which receives the measured data from the other components, and in badly designed systems also data transfer. Figure 1.11

summarizes the most relevant DT sources in a PET scanner system. However, the total DT losses are combinations from individual contributions. In General, there is no method to distinguish the contribution from each individual DT source. Consequently, an optimal DT correction method should make use of a model that involves the DT contribution and behavior from all system elements at different count rates and at different processing levels, since often, the DT losses in the system are a combination of both DT models (paralyzable and non-paralyzable). The determination of the overall DT can be measured by comparing the total measured coincidences rates and the real, ideal emission rate. (Müller 1991; Takacs 1958; Albert & Nelson 1953; Usman & Patil 2018).

1.4.1 DT Measurements

Two main measurement methods are generally used to estimate the overall DT of the entire measurement system. DT of the entire measurement includes all potential contributions of DT, including the DT from

the detector and the DT in the electronic pulse processing.

- The two-source method is one simple method to estimate the total DT of the entire system. This method is based on the measurement of the count rates from two radioactive sources individually and in combination. In a system with dead time, the measured average count rates which result from the combined sources will be less than the sum of the measured average count rates for each radioactive source individually. The differences between the count rates is the loss of counts due to the system DT (Moon 1937; Beers 1942; Usman & Patil 2018; Bécares & Blázquez 2012). This method is especially suited for phantoms measurements but it has the drawback that the type of DT behavior, i.e., paralyzable, non-pralyzable, etc., needs to be known, Further, the measured count rate depends on the measurement geometry. Figure 1.12 illustrates the two-source method. Two radioactive source, S_1 and S_2 with approximately the same activity

should be used (difference between activities should be less than a 10% of the source activity) and they must be placed at the defined distances D_1 and D_2 from the detector. In case of the non-paralyzable one measurement is then described by equation 1.13 (Leo 1988; Patil 2010; Müller 1973; Usman & Patil 2018):

$$O + n = \frac{m}{1-m\tau} \qquad (1.13)$$

Here, n is the input count rate, m is the measured count rate, τ is the constant DT, and O is the offset or background count rate. If the device has a small DT or the source activities are sufficiently small, i.e., we have $m\tau_D \ll 1$, equation 1.13 can be approximated by equation 1.14 (Leo 1988; Patil 2010; Müller 1973; Usman & Patil 2018):

$$O + n \approx m(1 + m\tau) \qquad (1.14)$$

As we have two sources, we can perform tree different measurements, the two sources individually and in combination, in which case, the input count rates from the two sources n_{1+2} is given

by $n_{1+2} = n_1 + n_2 + O$ and we obtain the three equations given in 1.15 (Leo 1988; Patil 2010; Müller 1973; Usman & Patil 2018):

$$\begin{aligned} n_1 + O &\approx m_1 (1 + m_1 \tau) \\ n_2 + O &\approx m_2 (1 + m_2 \tau) \\ n_{1+2} = n_1 + n_2 + O &\approx m_{1+2} (1 + m_{1+2} \tau) \end{aligned} \qquad (1.15)$$

Here, n_1 is the input count rate of source one, n_2 is the input count rate of source two, while m_1 is the measured count rate of source one, m_2 is the measured count rate of source two, m_{1+2} the measured count rate of the combination of the two sources. The set of equations can be solved to give the DT (τ) as written in 1.16 (Bock et al. 2000):

$$\tau = \frac{m_1 + m_2 - m_{1+2} - O}{m_{1+2}^2 - m_1^2 - m_2^2} \qquad (1.16)$$

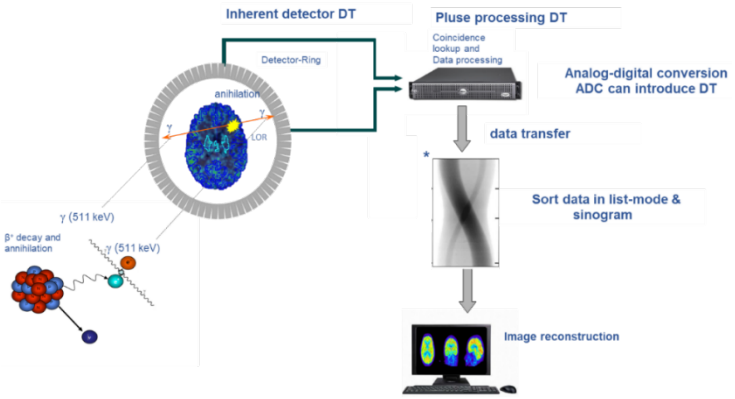

Figure 1.11 Visualization of the most relevant DT sources in a PET scanner system, *adapted from (Fahey 2002).

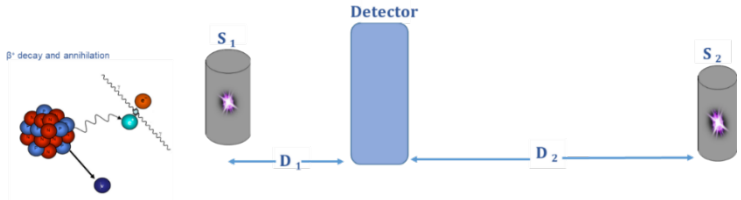

Figure 1.12 The two-source method for determining the system dead time. S1 and S2 are two radioactive sources with approximately the same activity (difference should be less than a 10%). The sources are placed at the distances D1 and D2 to the detector.

- The decaying source method is the second method to measure the overall DT for the detection system. A phantom with decaying activity is used in this method. The half-life radioisotope and the radioactivity concentration of the phantom filling must be known. The method has the advantage, that it can be used also to determine the DT behavior of the system, i.e., if a paralyzable model or a non-paralyzable model or any other model should be used. However, depending on the used radioisotope, this method takes a long time to acquire the required measurement for the determination of the DT and the dead time behavior. The half-life of the radioisotope should have a value that allows the measurement at substantially different count rates in a feasible time. According to exponential decay, the true count rate can be described by equation 1.17, where n_{ba} is the offset (background) count rate (Knoll 2010; Müller 1973; Usman & Patil 2018; Patil & Usman 2009):

$$n = n_0 e^{-\lambda t} + n_{ba} \qquad (1.17)$$

Here, n_0 is the initial true count rate at the start of the measurement, λ is the decay constant of the radioisotope. One obtains for the non-polarizable model with equation 1.9 and by ignoring the background the equation given in 1.18 (Knoll 2010; Müller 1973; Usman & Patil 2018; Patil & Usman 2009):

$$m\, e^{\lambda\, t} = -n_0\, \tau\, m + n_0$$

$$better: \quad \tau = \frac{1}{m} - \frac{e^{\lambda\, t}}{n_0} \qquad (1.18)$$

Here, m is the measured count rate at the measurement time t.

Figure 1.13 illustrates the decaying source method. Many previous studies used the decaying source method with some improvements and adjustments improve the accuracy (Müller 1973; Usman & Patil 2018; Patil & Usman 2009).

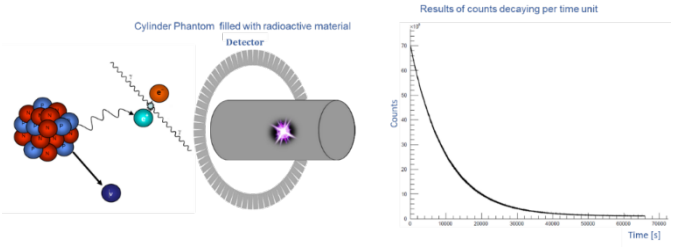

Figure 1.13 The decaying source method. Left: the cylinder is filled with radioactive material for the radioactive decay measurement in the PET detector. Right: the results of the radioactive decay experiment.

- The Two-Pulser method is a technique to measure the DT of parts of the electronic instrumentation. It is based on the use of two oscillators delivering pulses with different frequencies (V, V_1, V_2, and V_{mean} are frequencies). This method is similar to the two-sources method and is a very precise technique to measure the DT of the system components. Essentially, the two decaying sources are replaced by two oscillators, which are running at frequencies $V_1 = 1/T_1$ and $V_2 = 1/T_2$, creating a superposition of the two oscillations which is

fed into the input of the system component whose DT should be determined. The period $\mathrm{T} = 1/\mathrm{V} = \min(T_1, T_2)$ is the reciprocal of the larger one of the both oscillator frequencies (Müller 1973; Usman & Patil 2018). The mean of the frequency of superimposed pulses (V_{mean}) which passed the electronic component with DT (τ) is given by 1.19 for the non-paralyzable model (Müller 1973; Usman & Patil 2018):

$$V_{\mathrm{mean}} = \begin{cases} V_1 + V_2 - 2\tau V_1 V_2 & 0 < \tau < \mathrm{T}/2 \\ V & \mathrm{T}/2 \leq \tau < \mathrm{T} \end{cases} \qquad (1.19)$$

Whereas for the paralyzable DT model, V_{mean} is given by 1.20 below (Müller 1973; Usman & Patil 2018):

$$V_{\mathrm{mean}} = \begin{cases} V_1 + V_2 - 2\tau V_1 V_2 & 0 < \tau < \mathrm{T} \\ 0 & \tau > \mathrm{T} \end{cases} \qquad (1.20)$$

In the case of $V < 1/(2\tau)$ the value of τ is independent of the DT model, and for this case and for n_1, n_2 and n_{mean}, which are the numbers of the pulses counted in the measuring time t, the DT

constant is given by equation 1.21 below (Müller 1973; Usman & Patil 2018):

$$\tau = \frac{t}{2} \frac{n_1 + n_2 - n_{\text{mean}}}{n_1 n_2} \qquad (1.21)$$

In the case, that $V > 1/(2\tau)$, the observed count rate V_{mean} offers us simple means to check the DT type. This method has been improved and used in many related studies (Schönfeld & Janssen 1994; Baerg 1965; Müller 1973; Usman & Patil 2018; Patil & Usman 2009).

1.4.2 Impact of DT on Quantitative Images

Several components in PET system can suffer from DT losses and these losses can affect the accuracy of the quantitative PET images. Each detector system and heir components are affected in different ways by DT. DT losses are systematic errors which introduced a bias in the quantitative measures derived from the images. Essentially, DT losses lead to an underestimation of the pixel value in the reconstructed quantitative images, if not corrected.

(Mazoyer et al. 1985; Freedman et al. 1992). For instance, DT losses result in an overestimation of the thyroid uptake in studies ^{123}I (Maguire 1988). As DT losses increase at high count rates, the DT losses generally vary during the scan time, as the radiotracer distributes and decays. This is especially relevant for dynamic acquisitions and for studies using tracers with a short half-life, but also for studies using the bolus injection scheme (Hoffman et al. 1983; Zaidi 2006). An accurate correction of the DT losses is indispensable for quantitative PET imaging, in addition to all other data corrections such as attenuation correction, scatter correction, and random coincidence correction. A less accurate DTC method increases quantification biases in image reconstructions and results in less accurate mean counts. This will result also in a bias of the measured time activity curves (TAC) and quantities derived from the TACs, such as the maximum tumor-to-brain ratio ($TBR_{max)}$, mean tumor-to-brain ratio (TBR_{mean}), non-displaceable binding potential (BP_{ND}), the volume of distribution (V_T) and molecular rate constants (k). Finally, inappropriate

implementation of the DT correction may invalidate the positivity assumption of Poisson nature of the detected events and may lead to additional reconstruction and quantification biases when using Maximum Likelihood (ML) based reconstructions (Toga & Mazziotta 2002; Morris et al. 2004; Brambilla et al. 2021). For that, achieving higher accuracy in the DTC is important and should be taken into consideration as well as all other corrections for achieving quantitative PET images.

1.5 The Siemens 3T MR BrainPET-Insert

The successful usage of the hybrid imaging modality PET/CT in clinical applications has supported combining PET with other medical imaging techniques i.e., PET/MRI. The Siemens 3T MR-BrainPET insert installed at the Forschungszentrum Jülich (see figure 1.14) is one of several prototypes of dedicated brain hybrid MRI/PET systems worldwide. It is built from a commercial 3T MRI and a MR compatible BrainPET insert (Herzog et al.

2011; Shah et al. 2013). All measurements in this work were done with the Siemens 3T MR-BrainPET Insert. In this scanner, the acquired data is recorded in list-mode format and histogrammed into sinograms. Random coincidences are estimated by the delayed window technique (Markiewicz et al. 2018; Markiewicz et al. 2016). The energy acceptance window is set to 420 to 600 keV. Figure 1.15 shows a typical energy spectrum of the BrainPET insert together with the mentioned energy window. The coincidence time window is fixed at 12 ns. The BrainPET insert uses Avalanche Photo-Diodes, (APDs) as an MR compatible alternative to the photomultipliers, and scintillation event processing is done on the Quicksilver platform (Newport et al. 2006; Hu et al. 2011). As scintillator, LSO is used. The LSO crystals have a pixel pitch of 2.5 mm x 2.5 mm and their length is 20 mm. The crystals are coupled by a light guide to a 3 x 3 array of Hamamatsu S8664–55 APDs, each of them having a sensitive area of 5x5 mm^2. For temperature stabilization, the detector modules are supplied with cooled air. The PET scanner consists of 192 detector

blocks arranged in 32 cassettes (heads), each head bearing 6 detector blocks, (see figure 1.14, & figure 3.3 in chapter 3). Each detector block with its 12x12 scintillation pixels, the 3x3 APDs, and the attached analogue readout electronics acts as one position sensitive scintillation detector with individual count rate and DT loss. The BrainPET insert has an axial FOV of 19.2 cm and a transversal FOV of 31.4 cm (Weirich et al. 2012; Caldeira et al. 2018; Weirich et al. 2013; Weirich et al. 2013).

1.6 Motivations of the DTC for the 3TBrainPET-Insert

For the Siemens 3T MR-BrainPET insert, the current DTC method is global, i.e., this method is based on a count rate-dependent correction factor, which is obtained by averaging over all scintillation detector blocks in the system. For this, the CFD counts for each block are summed over all scintillation detectors to estimate the global,

unqualified (non-validated) single counts and the overall single count losses caused by DT (Weirich et al. 2012; Caldeira et al. 2018; Weirich et al. 2013; Weirich et al. 2013).

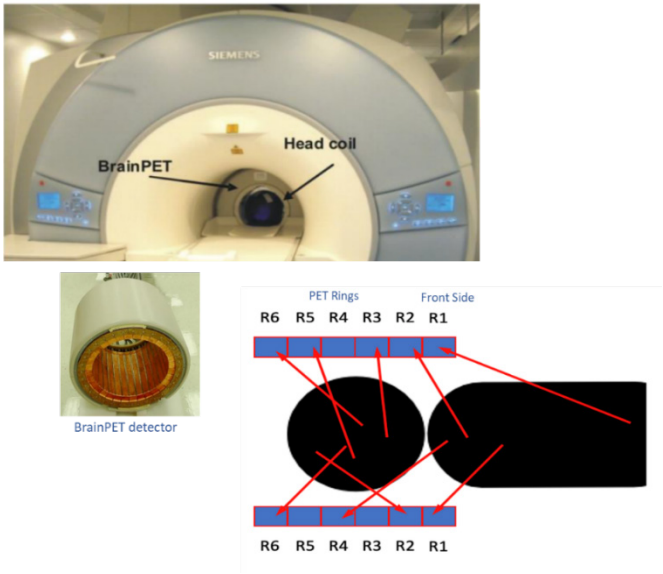

Figure 1.14 The Siemens 3T MR-BrainPET insert at the Forschungszentrum Jülich and a schematic of the detector rings and the position of the patient head.

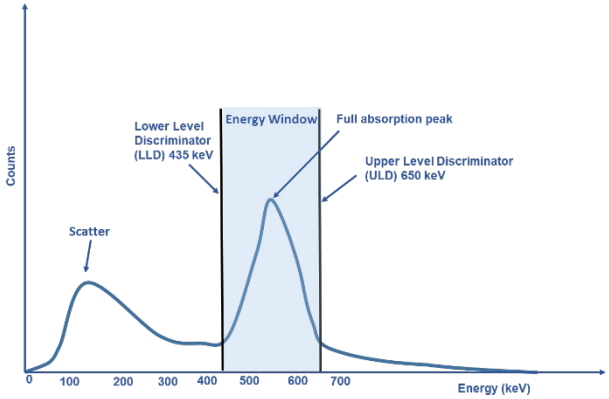

Figure 1.15 The energy spectrum and energy window setting for the BrainPET insert.

As explained, the Siemens 3T MR-BrainPET insert consists of 192 detector scintillation detector blocks arranged in 32 heads (see figure 1.14, & figure 3.3 in chapter 3). Each head bears 6 block detectors, thus forming 6 rings of block detectors. Figure 1.16 shows the unqualified, uncorrected single count rates for 8 different heads of one sector (left) and the 6 different rings (right) from a volunteer measurement with [^{11}C]ABP688 (Issa et al. 2022). As can be observed, the uncorrected count rates are significantly different for the individual heads and

rings. The highest single count rates were found in those blocks close to the radioactivity sources, especially in the first ring of the PET insert. The observed large differences in these count rates affects the accuracy of the DTC factor of the global DTC method, as DT losses depend non-linearly on the count-rates and the differences are not correctly accounted for when using averaged DTC factors. Furthermore, it is ignoring the physical position for each block, thus resulting in inaccurate DTC correction and loss of quantitation accuracy. Apart from the non-uniform activity distribution inside the BrainPET FOV, the DT of individual block detectors is also affected by the radiation of the whole body which is outside of the FOV. This further increases the differences in the single count rates seen by the individual detector blocks and makes the DT losses dependent on the position of the detector block. Therefore, correcting the DT losses for all blocks individually potentially provides more accurate results for quantitative imaging (Issa et al. 2022). Figure 1.17 shows the reconstructed activity concentration in Bq/cm^3 for a

phantom measurement over several half-lives of the nuclide (Issa et al. 2022). The phantom was filled with a ^{18}F solution and placed inside of the PET FOV. An additional phantom with activity was placed outside of the FOV. A region of interest (ROI) was drawn in the reconstructed image of the phantom located at its backside. A significant overcorrection by the global DTC method of up to 10 % of compared to the expected reconstructed activity concentration (dashed red line) can be observed (Issa et al. 2022).

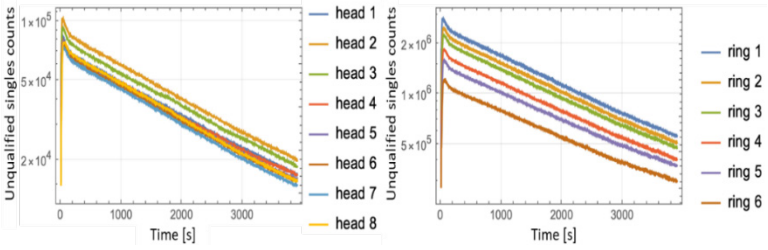

Figure 1.16 The unqualified single counts for the 8 detector heads of one sector on the left side and for individual block rings on the right side. Measurements were taken with the Siemens 3T MR-BrainPET insert from an [^{11}C]ABP688 volunteer measurement adapted from Issa et al. 2022.

For comparison, also the reconstructed activity concentration without DTC is shown. The main motivation of this work was to improve the accuracy of the DTC by implementing a block-pairwise DTC method for the Siemens 3T MR-BrainPET Insert, where the DT is corrected for each pair of scintillation blocks individually. By this, an increased quantitation accuracy for the PET images shall be achieved. The presented method is based on the estimation of the DTC factor as a nonlinear function derived from the delayed random coincidence rate for individual detector rings (Yamamoto et al. 1986; Issa et al. 2022).

For this endeavor, Yamamoto's DTC method was adapted for estimating the DT losses for the 3T MR-BrainPET insert for individual scintillation block pairs. In this work, the precision (noise statistical noise) and the accuracy of this modified method will be compared with the global DTC method currently used on the Siemens 3T MR-BrainPET Insert.

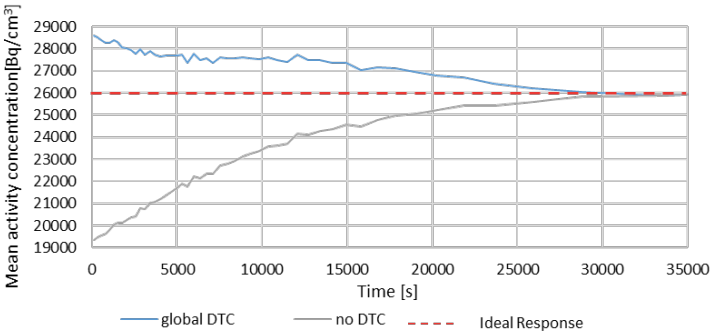

Figure 1.17 Reconstructed activity concentration in Bq/cm^3 vs. time in seconds for phantom measurement (^{18}F) for a ROI at the backside of the FOV and with out-of-FOV activity adapted from Issa et al. 2022.

Further, the impact of the DTC methods on the different clinical and scientific measurements with tracers with different half-lives was studied, in order to quantify the impact, the improved DTC method has on quantitation accuracy.

2. Research Objective

2.1 Main Objective

Development, evaluation and validation of an improved DTC method for the Siemens 3T MR BrainPET insert.

2.2 Specific Objectives

1- Evaluation of the properties of the global DTC method used as current DTC method in the Siemens 3T MR BrainPET insert.
2- Study the inherent DT behavior of individual system components i.e., with respect to paralyzable or non-paralyzable characteristics.
3- Development and implementation of an improved DTC method (block-pair-wise DTC method) for the Siemens 3T MR BrainPET insert.

4- Evaluation of the implemented DTC method with phantom measurements.
5- Validation of the implemented DTC method with patient and volunteer measurements using different tracers, i.e. as [^{11}C]ABP688, [^{18}F]-FET-PET, and [^{15}O]H_2O.

3. Methods

Three DTC methods were investigated throughout the present work in order to achieve an improvement in DTC for the dedicated BrainPET. First, the global DTC method (currently used method for acquisition with the Siemens 3T BrainPET-insert). The second method was the block-wise DTC method, and the third method was the block-pairwise DTC method which resulted in sufficiently accurate and consistent results when compared with the two other DTC methods. This chapter discusses those three methods.

3.1 Mathematical Models

3.1.1 Global DTC Method

In the Siemens 3T MR BrainPET insert, constant fraction discriminator (CFD) are used to generate walk-free timing signals. A timing signal is generated when the electrical pulse (from the PMTs or APDs and SiPMs) passes through a

discriminator, e.g. a CFD. The CFD is an electrical component used to generate the digital pulse when the signal reaches a consistent fractional part of the peak pulse height. Then, these timing signals are used in the coincidence circuitry. In addition, LLD (Lower level discriminator) and ULD (upper level discriminator) are discriminators used to filter the electrical pulses according to their energy or height (see figure 1.15 in the introduction) (Ullisch &Moses 2007; Badawi et al. 1996; Schaart 2021). The DT correction that is currently routinely applied on the Siemens 3T MR BrainPET insert scanner in the research center Jülich is the global DTC (Weirich et al. 2013; Weirich et al. 2012).

For this, the CFD counts from all blocks are summed to estimate the global, non-validated single counts and the overall DT-induced non-validated (unqualified) single count losses. The CFD counts are the non-validated singles that pass by the CFD without estimating the position

(scintillation pixel) in the block and which are not energy filtered, i.e., these events are counted always when the CFD was triggered (Ullisch & Moses 2007; Weirich et al. 2013).

For typical measurements with the Siemens 3T MR BrainPET insert scanner, global non-validated single count rates (sum over all 192 detector blocks) are measured, then the corresponding correction factor is determined to individual single count rates. The dead time correction factor ($DTCf$) is shown in figure 3.1 as a function of the non-validated singles count rates.

The global DTC factor ($DTCf$) was fitted with a polynomial of 6 degrees. The free fit parameters are ($fitp0, \dots fitp5$), as in equation 3.1 below, the global DTC factor value ($DTCf$):

$$DTCf = fitp0 + Cfd_{total} \cdot fitp1 + Cfd_{total}^2 \cdot fitp2 + Cfd_{total}^3 \cdot fitp3 + Cfd_{total}^4 \cdot fitp4 + Cfd_{total}^5 \cdot fitp5 \quad (3.1)$$

Here, the Cfd_{total} is the total of the CFD counts rates from all blocks.

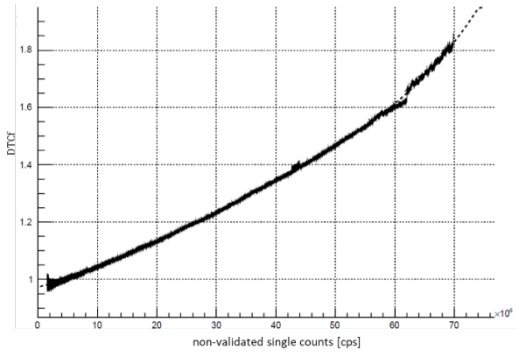

Figure 3.1 The global DTC factor as a function of the non-validated single count rates for the Siemens 3T MR BrainPET insert.

The ideal and measured global trues count rate are presented in figure 3.2, The $DTCf$ in the case of the true count rates is given in 3.2 expression below. The ideal true count rates are not affected by the DT, especially in the low count rates. So the ideal true count rates are an extrapolation of the low count rates with an exponential function. The first period of the measured count rate shows the saturation in case of the system doesn't suffer from the DT (see figure 3.2):

$$DTCf = \frac{C_{Ideal}}{C_{Measured}} \qquad (3.2)$$

Here, the C_{Ideal} is the total ideal count rate, and $C_{Measured}$ is the total measured count rates.

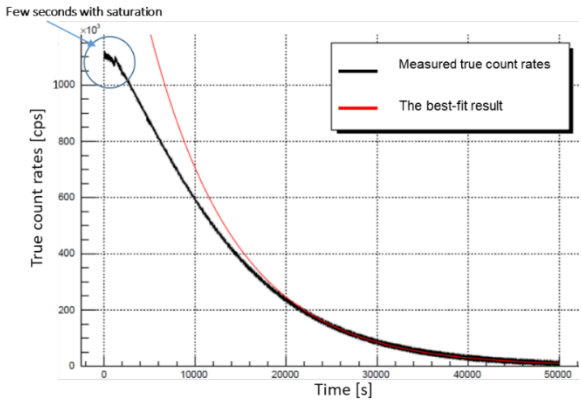

Figure 3.2 The global trues count rate (ideal and measured), black line: the measured global true count rates (the first seconds of the measured true count rates are affected by saturation. This is effect is not corrected for in the present work and the corresponding data cannot be used), red line: the best-fit of the ideal global true count rates.

The global $DTCf$ can be used as a function of the CFD count rates and to approximate the total counts

C_{Ideal} unaffected by DT (Weirich et al. 2013; Weirich et al. 2012).

There are two major problems introduced by the global $DTCf$. First, it is based on the measurement of non-validated (unqualified) singles counts, while for the prompt and true coincidences, only validated, i.e. energy filtered, singles are accepted. Therefore, the global $DTCf$ leads to a systematic deviation (bias) in the DT correction result. Secondly, as described in section 1.4, the count rates can be very different on block level, leading to different block level DT factors. Consequently, an improvement of the DT correction for the dedicated Siemens 3T MR BrainPET insert is needed.

3.1.2 Block-wise DTC Method

The global DTC is insufficient for accurate DT correction.

An independent DTC for each detector block is needed to achieve sufficiently high accuracy for quantitative PET imaging. Figure 3.3 shows the

arrangements and locations of the detector blocks and heads (cassettes) in the Siemens 3T MR BrainPET insert, and the hitmap for all 192 blocks. The hitmap is a map that shows the counts for every single crystal on each block detector. It consists of 6 x 32 blocks; each block represented by a 12x12 LOS-crystal matrix. The hitmap is used to present the coincidences, i.e. prompts and delayed and they are used for the regular quality control (Weirich et al. 2012).

A block-wise DTC model can potentially be used to describe the DT behavior of the Siemens 3T MR BrainPET insert on scintillation block detector level and to accurately correct for DT losses.

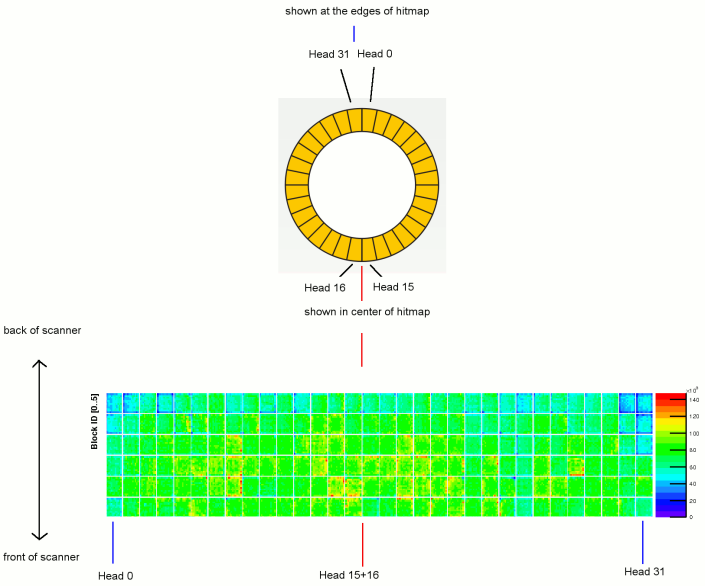

Figure 3.3 Arrangements and locations of the detector blocks and heads (cassettes) in the Siemens 3T MR BrainPET insert together with the hitmap for all 192 blocks.

The activity $\mathrm{A(t)}$ of a decaying source is given by equation 3.3:

$$\mathrm{A(t)} = A_0 \left(\frac{1}{2}\right)^{\frac{t}{t_{\frac{1}{2}}}} + O_A \qquad (3.3)$$

Where A_0 is the starting activity, i.e. $\mathrm{A(0)}$, $t_{1/2}$ is the half-life of the isotope, t is the elapsed time in

seconds and O_A is the offset due to intrinsic ^{176}Lu background in cps/cm^3 (Wei 2015; Alva-Sánchez et al. 2018).

The decay losses for the non-paralyzable DT (NP_{DT}) model are described by equation 3.4:

$$S_m(t) = \frac{S(t)}{1+S(t)\cdot\tau} \qquad (3.4)$$

Here, S_m are the measured singles, S are the ideal singles, and τ is the DT constant .

As all PET scanner have a detection efficiency ϵ with $0 < \epsilon < 1$, we can write for the singles $S(t) = \epsilon \cdot A(t)$. Thus we can write as 3.5:

$$\mathrm{S(t)} = S_0 \left(\frac{1}{2}\right)^{\frac{t}{t_{\frac{1}{2}}}} + O \qquad (3.5)$$

Here, the offset O differs from O_A, because of the detection efficiency. The subscript "S" for singles have been omitted for simplicity. By plugging equation 3.5 into equation 3.4, we obtain equation 3.6 which will be used as fitting model and which describes the expected block-wise, average, and

total, non-validated single count rates in the scanner at arbitrary time t:

$$S_m(\mathrm{t}) = \frac{S_0 + 2^{\frac{t}{t_{1/2}}}\mathrm{O}}{S_0 \cdot \tau + 2^{\frac{t}{t_{1/2}}}(1+\tau \cdot \mathrm{O})} \qquad (3.6)$$

The equation to obtain the DTC factor-is given by 3.7:

$$DTCf_{Block-wise}(\mathrm{t}) = \frac{1}{1 - S_m(t) \cdot \tau} \qquad (3.7)$$

From equation 3.7 it becomes obvious, that the dead time correction factor depends on the time, when the measured counts depend on time. It shall be noted, that the subscript "Block-wise" refers to the method, i.e. Equation can 3.7 is valid in block level and on scanner level. There are 192 scintillation detector blocks in the Siemens 3T MR BrainPET insert, thus their IDs are counted from 0 to 191. Two sub-indexes are used to define the block IDs, the first one is counted according to the physical location of the detector blocks inside the detector cassettes or heads. There are 6 blocks in each of the 32 heads yielding a total of 192 blocks. We use a convention

of separating the head and block numbers in a string of the form head number: block number, where the head ID (ID_{head}) is a number from 0 to 31 and the block ID (ID_{block}) is a number from 0 to 5. We can get a block number from this scheme by multiplying the head number by 6 and adding the block number: Block ID = $ID_{head}*6+ID_{block}$. The identification scheme is a BLUT (block lookup table) function or array (defined by Siemens). Figure 3.3 visualizes the numbering scheme. There is a second Both, individual block CFD counts and total CFD counts fit very well to the NP_{DT} model. Figure 3.4 shows, the total CFD counts (non-validated singles) for the PET detector together with the best fit to a NP_{DT} model i.e., equation 3.7. The fit was applied to the total of the CFD counts from all 192 detector blocks in the PET scanner.

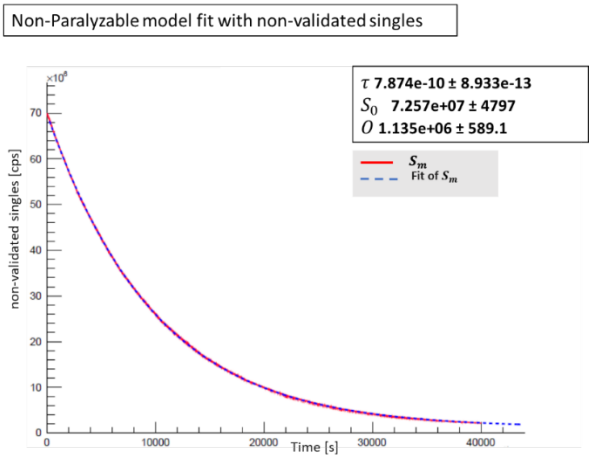

Figure 3.4 The total CFD counts for the entire PET detector together with the best fit to a non-paralyzable dead time model (NP_{DT}). S_0 is the singles count rates at t=0, and O is the offset for CFD counts due to lutetium and natural background.

In the case of the qualified singles i.e., singles forming prompts and trues the effects upon the qualified singles introduced by energy filtering should be correctly considered for the two DT models i.e., NP_{DT} and paralyzable (P_{DT}) models. The investigation of the NP_{DT} and P_{DT} fitting models was applied to the total prompts events (trues plus

randoms) and to the delayed coincidence events for the total of all 192 blocks.

It is known, that the random count rate depends approximately quadratically on the activity equation 3.3. Further, as for true coincidences only validated singles are used, there is no contribution from ^{176}Lu background because the gamma photons generated during the decay have in all applications relevant for the present study less energy than LLD. However, the ^{176}Lu background can contribute to the randoms coincidences because of the energy of the beta particles created during the ^{176}Lu decay. Together with equation 3.4 for the non-paralyzable DT, we obtain the mathematical model the prompt coincidences NP_{DT} given in 3.8:

$$P_{NP}(t) \approx \frac{A_0' - A_0' \cdot B}{2^{t/t_{1/2}} + A_0' \cdot \tau} + \frac{B(2^{-t/t_{1/2}}\, A_0' + O)^2}{1 + \tau(2^{-t/t_{1/2}}\, A_0' + O)^2} \quad (3.8)$$

Here, $A_0^{'} = \epsilon \cdot A_0$, and B is introduced to account for the generally unknown fraction of random coincidences in the prompt counts. When using the

paralyzable DT model instead, the prompt coincidence count rates P_{DT} are described by equation 3.9:

$$P_P(t) = 2^{-2^{t/t_{1/2}}} A_0'(1-B)e^{-2^{t/t_{1/2}}A_0'\tau} + Be^{-\tau(2^{-t/t_{1/2}}A_0' + O)^2}(2^{-t/t_{1/2}}A_0' + O)^2 \quad (3.9)$$

Figure 3.5 shows the total prompts fitted with the NP_{DT} model, i.e. equation 3.8. Figure 3.6 shows the total prompts fitted with the P_{DT} model, i.e. equation 3.9.

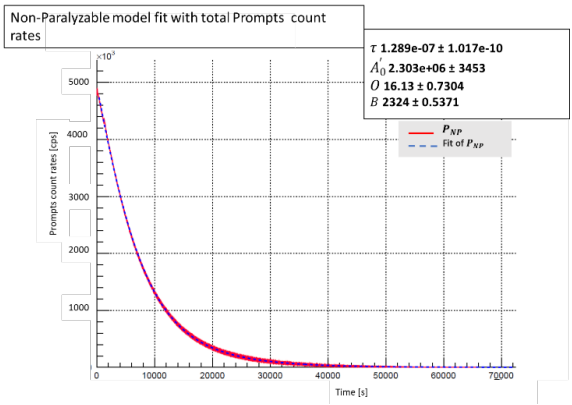

Figure 3.5 Total prompts fitted with non-paralyzable model (NP_{DT}), O is the offset. P_{NP} is the measured prompt count rate.

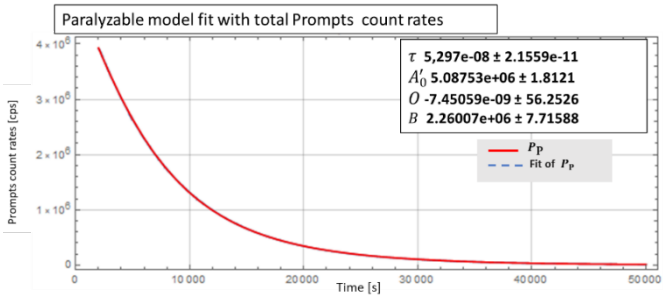

Figure 3.6 The total prompts fitted with paralyzable (P_{DT}) model. O is the offset. P_P is the measured prompt count rate.

3.1.3 Block-Pairwise Method

The high differences in block count rates is the main reason to implement a DTC method on block-wise level. For the implementation, both standard mathematical models for DT, i.e. the P_{DT} and the NP_{DT} models (Müller 1973; Bailey et al. 2005; Ensslin 1991) were tested. As will be shown, the count rates observed during typical PET examinations with the Siemens 3T MR-BrainPET Insert are not high enough to lead to substantial differences in the obtained results. Due to the

absence of differences, the block-wise DTC method based on the NP_{DT} model was implemented and only the derivation of the DTC factor for the NP_{DT} model is described in this work. However, the derivation of DTC factor for the P_{DT} model is analogue. As shown in Yamamoto et al., the expected delayed random coincidence rate without dead time losses can be obtained by extrapolation of the observed delayed coincidences. This allows to compute a DTC factor for the observed prompts coincidence rate (Yamamoto et al. 1986).

The LOR coincidences on the block level define all the working block pixels to find all prompt count rates in each block, for each second. The data have been filled from the prompts hit-map in the LOR file and (32 x 19)/2 = 304 is the number of PET cassettes, whose coincidences will be considered on the LOR data file (ring shape of the detector).

The PET detector has 32 cassettes, and for each cassette, the 19 opposed cassettes will be considered for coincidences, the remaining coincidences are discarded since the LORs are not passing through the head. We have to divide by two, since we find

the same LORs after rotating by 180 degrees instead of 360 degrees, since we have two gammas photons. On every scintillation block, there are 144 scintillation pixels leading to 144x6=864 scintillation pixels on each cassette. The electronics for the 3T MR BrainPET detector work at a block-wise level. Whenever the scintillation occurs and triggers the electronics, the electronics of the whole block is insensitive for a following time interval with the length of the dead time, independent of which of the 144 crystals on the block was hit.

The LOR data file has been created to find the number of pairs of coincidences for each pixel for all heads. Figure 3.7 below shows the total prompts for each of the head (0 & 8) combinations which is head pair nr. 8, and the trues coincidences for each of the head (0 & 19) combinations, which is head pair nr 12.

The measured delayed random coincidences rate (R_m) measured with the delayed window technique (Markiewicz et al. 2018; Markiewicz et al. 2016) is

affected by the DT as in equation 3.10 (Issa et al. 2022; Yamamoto et al. 1986):

$$R_m = \frac{R_{ideal}}{DTCf} \qquad (3.10)$$

Here, R_{ideal} is the delayed random coincidences rate without DT losses for any pair of scintillation blocks and the $DTCf$ is the DTC factor.

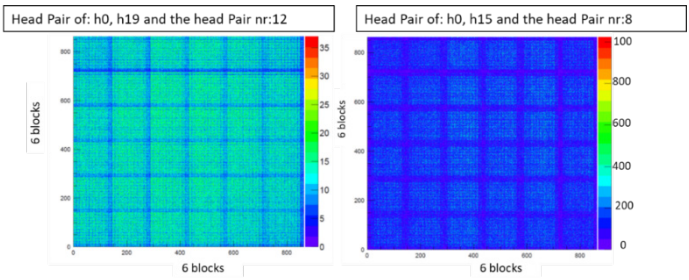

Figure 3.7 Left: The true coincidences for each pixel combination of the heads 0 & 19, which is head pair nr 12. Right: The prompts coincidences for each pixel combination of the heads 0 & 8, which is head pair nr 8.

Figure 3.8 shows relevant aspects of the block-pairwise method. The method is based on the estimation of the dead time correction factor as a nonlinear function derived from the delayed random coincidences rate in individual detector blocks.

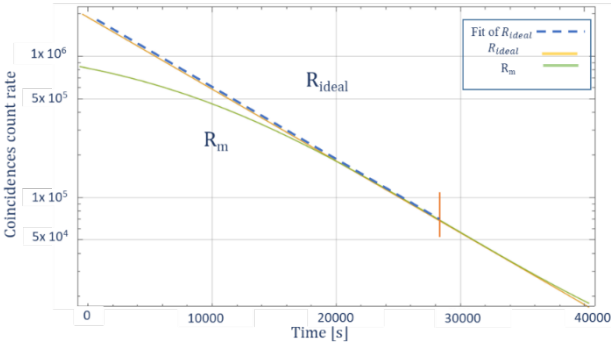

Figure 3.8 The block-pairwise method is based on the estimation of the DTC factor as a nonlinear function derived from the delayed random coincidences rate in individual detector blocks. R_m is the observed delayed random coincidences rate, R_{ideal} the delayed random coincidences rate without DT losses. The dashed blue line is the best linear fit of R_{ideal} in the linear region and its extrapolation.

Figure 3.9 presents the total trues coincidences in all head pairs and the best fit (red line) obtained with the non-paralyzable model. Equation 3.10 allows to compute the correction factor $DTCf$, if R_{ideal} and R_m are known during every instant of the measurement. P_{corr} are the corrected prompt coincidence count rates for each pair of scintillation blocks and they are given by the sum of R_{ideal} and the corrected true coincidence count rates T_{corr}. T_{corr} is given by 3.11(Issa et al. 2022; Yamamoto et al. 1986):

$$T_{corr} = DTCfT_m \tag{3.11}$$

Here, T_m are the measured true coincidence count rates.

Equally, the corrected prompt coincidence count rates P_{corr} can be computed by 3.12:

$$P_{corr} = DTCfP_m \tag{3.12}$$

Here, the P_m are the measured prompt coincidence count rates. Expression 3.13 gives the expected

count rates in case of the non-paralyzable dead time model:

$$C_m = \frac{C_{ideal}}{1+\tau\, C_{ideal}} = \frac{C_{ideal}}{DTCf} \qquad (3.13)$$

Here, the C_m is the measured count rate. C_{ideal} is the count rate without DT losses for any pair of scintillation blocks and τ is the DT. Equation is valid for the true count rate, the prompt count rate and the delayed random count rate. From the mathematical model for the prompt coincidences NP_{DT} (3.8), we obtain the Non-paralyzable (NP_{DT}) fitting model for the total measured trues count rates ($T_m(\mathrm{t})$) in the head pairs given in the expression 3.14. (Measured count rates and best fit shown in figure 3.9):

$$T_m(t) = \frac{A_0}{2^{t/t_{1/2}} + A_0 * \tau} \qquad (3.14)$$

The ideally expected delayed random count rates $D_{ideal}(t)$ as a function of the time t can be

approximated as already explained above to give equation 3.15 (Issa et al. 2022):

$$D_{ideal}(t) \approx (2^{-t/t_{1/2}} A_0' + O)^2 \qquad (3.15)$$

Figure 3.10 shows the best fit for the total delayed random coincidences in the time interval between 10000 and 20000 seconds for the BrianPET detector, obtained with equation 3.15.

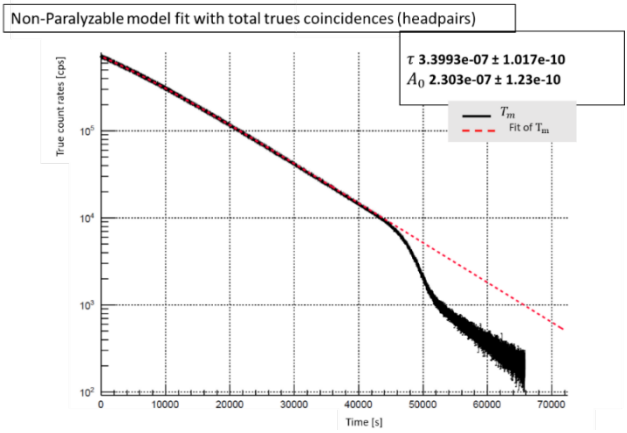

Figure 3. 9 Non-paralyzable (NP_{DT}) fitting model of total trues count rates in the head pairs. A_0 is the measured true count rates at t=0

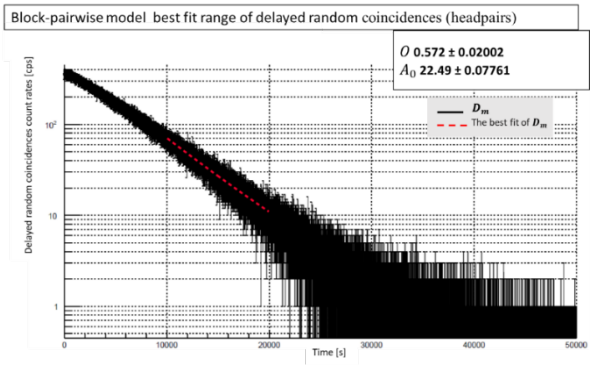

Figure 3. 10 Best fit (blue dashed line) for the delayed random coincidences (red line) in the time interval between 10000 and 20000 seconds in in Siemens 3T MR BrainPET insert. D_m is the observed delayed random coincidence rate.

One important effect which is considered in this work in addition to the method presented in Yamamoto et al. 1986, is a correction of triple coincidences, i.e., when 3 gamma photons are detected simultaneously. Triple coincidences are not uncommon and may be caused by inter-detector scatter and random events (Lage et al. 2015; Cal-González et al. 2013; Pál & Pázsit 2012). In the

Siemens 3T MR-BrainPET insert, triple coincidences are found as two double coincidences in the list-mode data and they are found both in the prompt and delayed coincidences lists. Thus, they would result in count rate overestimation in the presented DTC method and a corresponding triples correction should be applied to correct this effect, especially as the coincidence window of the BrainPET insert is rather large. Figure 3.11 illustrates the double counting of one single event that leads to the overestimation which requires an appropriate correction.

Due to their much lower probability, correction for multiple coincidences was not explicitly considered in this work. The over estimation of delayed random counts caused by triples can be approximated by the empirical model 3.16 (Issa et al. 2022):

$$\widetilde{D}_m = m(D_m)^{\frac{1}{k}} \qquad (3.16)$$

Here, the $\widetilde{D}_m$ are the observed counts with overestimation due to triples and m and k are free fit parameters.

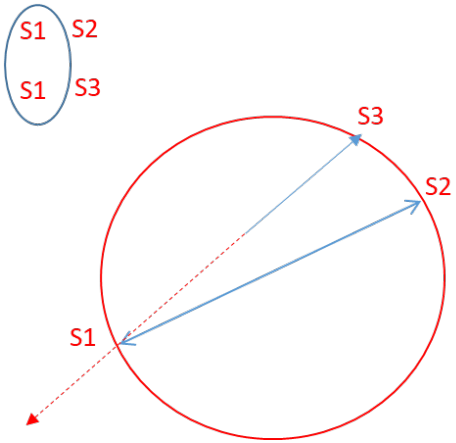

Figure 3. 11 The overestimation due to triples. S_1 is the single event that was listed two times thus resulting in an overestimation of coincidence events.

The expected counts of delayed random coincidences $\widetilde{D}_m$ can now be expressed by combining equations 3.13, 3.15, and 3.16, thus resulting in 3.17 (Issa et al. 2022):

$$\widetilde{D}_m\,(t) = m\left(\frac{(2^{-t/t_{1/2}}\,A_0'+O)^2}{1+\,\tau(2^{-t/t_{1/2}}\,A_0'+O)^2}\right)^{\frac{1}{k}} \qquad (3.17)$$

The DTC factor $DTCf$ can now be obtained in two steps.

First, equation 3.17 is solved for t resulting in equation 3.18 (Issa et al. 2022):

$$t = \frac{\log\left[\frac{A'_0\, O - \tau A'_0\, O\left(\frac{Dm}{m}\right)^k + \sqrt{A'^2_0\left(\frac{Dm}{m}\right)^k - \tau A'^2_0\left(\frac{Dm}{m}\right)^{2k}}}{-O^2 + \left(\frac{Dm}{m}\right)^k + \tau O^2\left(\frac{Dm}{m}\right)^k}\right] t_{1/2}}{\log[2]} \quad (3.18)$$

Then, the time obtained from the model for the measured delayed random count rates, i.e. equation 3.18 is inserted into the model for the ideal delayed random count rates, i.e. equation 3.16 yielding equation 3.19 (Issa et al. 2022) when dividing by D_m:

$$DTCf(D_m) = \frac{\left(O_i - \frac{A'_{0,i}\, O_m}{A'_{0,m}} + \frac{A'_{0,i}\left(\frac{Dm}{m}\right)^k}{\sqrt{A'^2_{0,m}\left(\frac{Dm}{m}\right)^k\left(1-\tau\left(\frac{Dm}{m}\right)^k\right)}}\right)^2}{D_m} \quad (3.19)$$

Where we differentiated between O_i and O_m and $A'_{0,i}$ and $A'_{0,m}$ respectively, to account for different contributions of the ^{176}Lu background to the offset for the ideal and observed counts and for different contributions of the effective start activity $A'_{0,i}$ to the start activity for the ideal and observed counts.

It can be seen from equation 3.19, that with this formulation, $DTCf$ depends on the measured delayed random count rates. Equation 3.19 again gives the correction factor $DTCf$ for one single pair of scintillation blocks or for the entire system. However, as already explained, the block-wise count rates can differ significantly between each other, and a global consideration would introduce significant bias in the DT correction. Furthermore, although the $DTCf(D_m)$ is computed from the measured delayed random count rates, it can be sued to correct dead time losses for trues and prompts as well. As the Siemens 3T MR-BrainPET has 6 rings, 32 heads, and coincidences with only 19 out of 32 heads are used, the $DTCf$ for $6^2 \times 32 \times 19 \times {}^1/_2 = 10944$ used block-pairs must be determined and applied. Thus, the $DTCf$ are correction factors for block pairs, not for single blocks (Issa et al. 2022). All variables in equation 3.19 except the observed delayed random count rate D_m are used as free fit parameters. For the calibration, the time varying delayed count rates for all 10944 block-pairs were

fitted with equation 3.19 and the best fit parameters were stored.

For the correction during measurements, the 10944 individual count rates D_m are used together with the corresponding set of best fit parameters and equation 3.19 to compute the DTC factor for this pair, which is used subsequently to correct the prompt count rate for the corresponding block-pair according to equation 3.12. As figure 3.10 shows, the best-fit with equation 3.15 of the total delayed random coincidence was found in the time interval from 10000 to 20000 seconds. This model is needed for extrapolating the count rates D_m from the range where they are not affected by dead time to a range where they are affected. For the validation of the method, the corrected true coincidence rates of all 10944 block-pairs were summed, and the resulting scanner-wide true coincidence rate was fitted to a simple decaying exponential with the ^{18}F half-life to determine the relative fit residuals. For validation of the appropriateness of the empirical model for over counting due to triples, all prompt coincidences as a

function of the pure double coincidences were fit to equation 3.16.

3.1.4 Identifying the Corrected Coincidences of DT Factors

The DTC factors of the coincident singles for the total prompts and delayed randoms were applied to evaluate and the NP_{DT} model. The measured coincident singles differ and depend on the block DT and the lutetium background activity, which were chosen as free fitting parameters. Those fits were done with ROOT –An-Object-Oriented Data Analysis Framework (Brun & Rademakers 1997) and not all of the fits converged. However, as the block-wise model was discarded for reasons explained below, the fact that some fits did not converge does not affect the relevant results of this work. Figure 3.12 below shows the best fit parameters for the NP_{DT} model applied to the coincident singles of the delayed randoms for the 192 blocks of the Siemens 3T MR BrainPET insert, i.e. the lutetium background activity, the DT constant, and the amplitude (A_0). Figure 3.12 below

shows the best fit parameters for the NP_{DT} model applied to the coincident singles of the prompts for the 192 blocks of the Siemens 3T MR BrainPET insert, i.e. the lutetium background activity, the DT constant, and the amplitude (A_0).

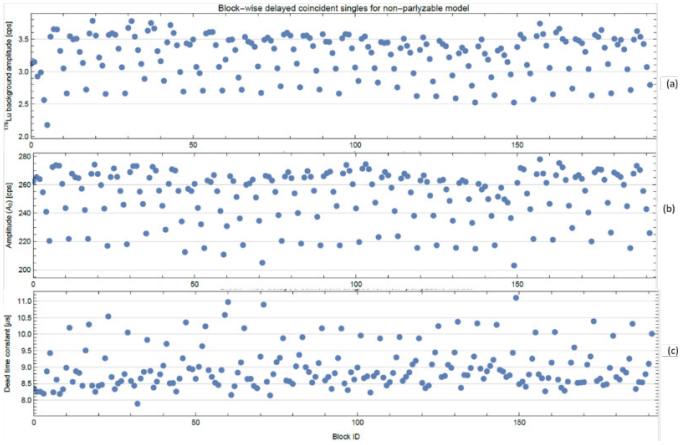

Figure 3.12 Best fit parameters for the NP_{DT} DT model and the delayed random coincident singles. a: Lutetium background activity, b: Amplitude (A_0), c: dead time constant.

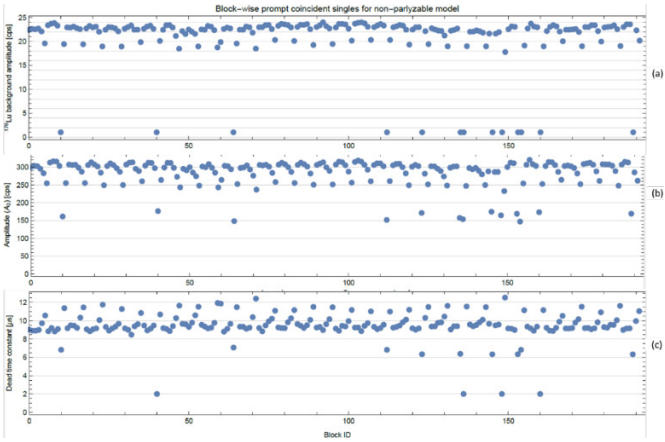

Figure 3.13 Best fit parameters for the NP_{DT} DT model and the prompt coincident singles. a: Lutetium background activity, b: Amplitude (A_0), c: dead time constant.

3.2. Measurements

All measurements were performed with the Siemens 3T MR BrainPET insert. The data was recorded in list-mode and in case of the block-pairwise method, all block pairs, which can lead to accepted coincidences (in total 10944) see 1.1.4 section in the introduction, were analyzed.

3.2.1 Phantom measurements

Evaluation and validation of the block-pairwise DTC were done with a Germanium (^{68}Ge) phantom and with a phantom filled with decaying activity of known half-life. In this work, we also studied the impact of the out-of-FOV activity on the calibration factor and its homogeneity for the DTC methods by evaluating the calibration differences in several ROIs by comparing scans taken with and without out-of-FOV activity. For all the phantom measurements (except the ^{68}Ge Phantom), the

activity concentrations of three reference probes were measured with a calibrated gamma counter (Wallac Wizard 1480) at the beginning of the measurement.

I. Germanium (^{68}Ge) Phantom Measurement

For measurement I, a ^{68}Ge phantom was used to characterize the CFD counts (unqualified singles) for the global DTC caste and the block-wise DTC case. We did short normal acquisitions with standard settings for 600 seconds. The phantom is the model CS 27 from Siemens Medical Solutions. It is a cylinder phantom with an active diameter of 20 cm and a length of 27 cm (volume: ≈ 8365.53 ml). The activity at the time of that measurement (14/2/2019) was 16.9 MBq. The phantom was transversally centered in the FOV and the measurement was done without the MR transmit/receive head coil.

II. Decay Experiment

For the decay experiments, cylindrical, homogeneous phantoms were used. During the phantom measurements, prompt and delayed coincidences count rates are registered for every second during approximately 7 half-lives (≈ 20 hours). For each block-pair, the DTC factor is computed and applied to the prompts. A homogeneous cylinder with inner diameter of 14 cm and length of 23.6 cm (volume: ≈ 3633 ml) was filled with 257.4 MBq activity of ^{18}F diluted in water. The phantom was transversally centered in the PET FOV with the MR transmit/receive head coil. Table 3.1 summarizes the measurements with the calibration probes for all decay experiments described in this chapter. Table 3.2 summarizes the average of the calibration probe measurements given in table 3.1.

III. Decay Experiment with Activity Out of FOV

A homogeneous cylinder with 14 cm inner diameter and 23.6 cm length (volume: ≈ 3633 ml) was filled with 141.8 MBq activity of ^{18}F diluted in water. The phantom was transversally centered in the FOV. The phantom was axially centered to the extent that the MR transmit/receive head coil allowed. In addition, a second homogeneous cylinder phantom with 20 cm inner diameter and 19 cm length (volume ≈ 5969 ml) was filled with 283MBq activity of ^{18}F diluted in water and placed outside of the FOV directly in front of the PET insert. Thus, the total activity was divided into two parts. Approximately 30% of the total activity was placed inside of the FOV and the remaining 70% was placed outside of the FOV to mimic the uptake in the patient's body which contributes significantly to the detector dead times. Figure 3.14 shows the phantom placement for measurement III inside and outside the dedicated Brain PET, see the decay experiment with out of FOV activity in table 3.1 and table 3.2.

IV. Three-Compartment Phantom Measurement

The fourth measurement was done with a three-compartment phantom (NEMA NU 2-994) filled with ^{18}F diluted in water. The inner diameter of the background compartment is 20 cm and the compartment is 23 cm long (volume ≈ 4180 ml). The three inserted compartments are 5 cm in diameter and 20 cm in length (volume ≈260 ml). One of them (hot compartment) was filled with an activity concentration 6 times higher than the activity concentration of background compartment and one of them (warm compartment) was filled with an activity concentration 2 times higher than the background. One insert is made from massive Teflon (cold compartment).

The activity in the background compartment was 113.3 MBq. Data was acquired for 11 hours and the phantom was centered inside of the FOV. In addition, a second homogeneous cylinder phantom (dimensions as described above) was filled with 82.6MBq activity and was placed outside of the

FOV. Figure 3.15 shows the placement of the two phantoms inside and outside the dedicated BrainPET. The compartment to background ratios for the hot and warm compartment were chosen as 6:1 and 2:1, as these values represent typical values for tumor to background ratios and the cortex region to cerebellum ratio, respectively, see three-compartment phantom measurement in table 3.1 and table 3.2.

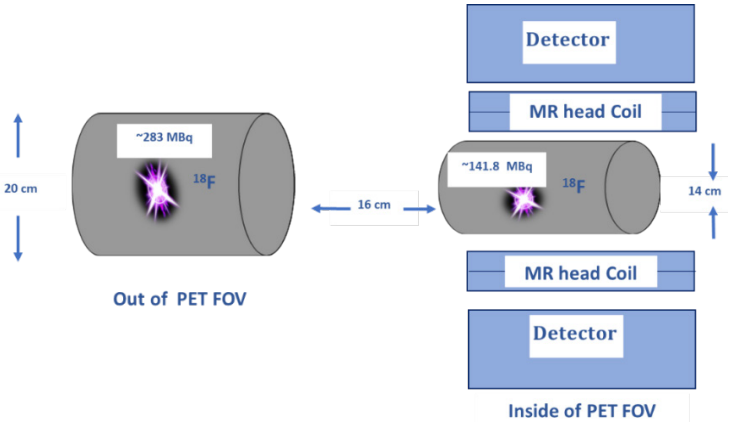

Figure 3.14 Position of the two phantoms for measurement III inside and outside of the BrainPET insert.

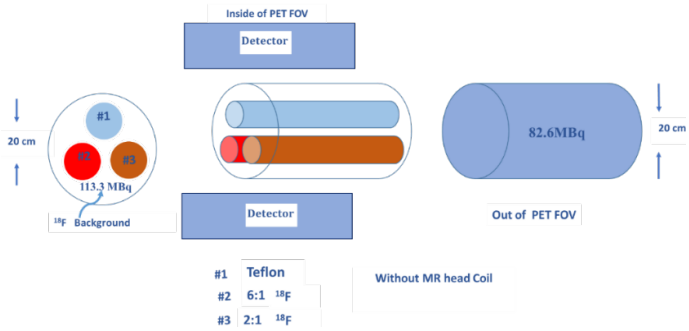

Figure 3.15 Position of the two phantoms for the measurements with the three compartment phantom (measurement IV) inside and outside of the BrainPET insert.

Table 3.1 The calibration probe measurements for all the decay experiments.

Measurement	Probe	Time	CPM	Volume
Decay Experiment without activity outside	1	12:56:10	745178	0.5 ml
	2	12:57:14	705815	0.5 ml
	3	12:59:33	670894	0.5 ml
Decay Experiment with Activity Out of FOV The phantom in FOV	1	11:06:40	520551	0.494 ml
	2	11:07:49	563834	0.495 ml
	3	11:09:01	522965	0.494 ml
Decay Experiment with Activity Out of FOV The phantom out of FOV	1	11:13:11	545858	0.496 ml
	2	11:14:21	583562	0.496 ml
	3	11:15:32	397060	0.498 ml
Three-Compartment Phantom Measurement The phantom in FOV	1	16:23:21	457450	0.499 ml
	2	16:23:21	387356	0.498 ml
	3	16:23:21	396461	0.5 ml

Hot-Compartment				
Three-Compartment Phantom Measurement The phantom in FOV Warm - Compartment	1	16:23:21	164508	0.496 ml
	2	16:23:58	164249	0.502 ml
	3	16:25:10	157421	0.5 ml
Three-Compartment Phantom Measurement The phantom in FOV Background	1	16:26:21	76071	0.496 ml
	2	16:27:33	73068	0.502 ml
	3	16:28:44	74142	0.502 ml
Three-Compartment Phantom Measurement The phantom out of FOV	1	16:30:06	143503	0.498 ml
	2	16:31:18	175947	0.5 ml
	3	16:32:29	167276	0.5 ml
CPM: counts per minute				

Table 3.2 The averages of the calibration probe measurements for all decay experiments.

Measurement	Time	CPM	Volume
Decay Experiment without activity outside	12:57:14	707295.7	0.5 ml
Decay Experiment with Activity Out of FOV The phantom in FOV	11:07:49	535783.3	0.495 ml
Decay Experiment with Activity Out of FOV The phantom out of FOV	11:14:21	508826.7	0.496 ml
Three-Compartment Phantom Measurement The phantom in FOV Hot-Compartment	16:23:21	413755.7	0.499 ml
Three-Compartment Phantom Measurement The phantom in FOV Warm -Compartment	16:23:58	162059.3	0.499 ml
Three-Compartment Phantom Measurement The phantom in FOV Background	16:27:33	74427	0.5 ml
Three-Compartment Phantom Measurement The phantom out of FOV	16:31:18	162242	0.499 ml
CPM: counts per minute			

V. Calibration Bias

The evaluation of the calibration bias was done with two measurements. In the first one, we used a homogeneous cylinder with 14 cm inner diameter and 23.6 cm length (volume: ≈ 3633 ml) which was filled with 64 MBq activity of ^{18}F diluted in water. The phantom was transversally centered in the FOV with the inserted MR transmit/receive head coil. A second homogeneous cylinder phantom with an inner diameter of 20 cm and length of 19 cm (volume ≈ 5969 ml) was filled with 126 MBq activity of ^{18}F diluted in water and was placed outside of the PET FOV. The scan time was 30 minutes. In the second measurement we scanned the phantom in the FOV without any activity outside of FOV. As this measurement was ≈ 30 minutes later we corrected the obtained value for the decay (correction factor ≈ 1.22 ($2^{(31.5/109.8)}$). Figure 3.16 shows placement of the phantoms for the measurement of the calibration bias with the dedicated BrainPET. The motivation for this measurement is to evaluate how the activity outside

of the FOV (caused by the activity in the patient body) affects the calibration in different regions of the FOV and for the different DTC methods. The measurements of the calibration probes are summarized in table 3.3 and the average measurements of the calibration probes are summarized in table 3.4.

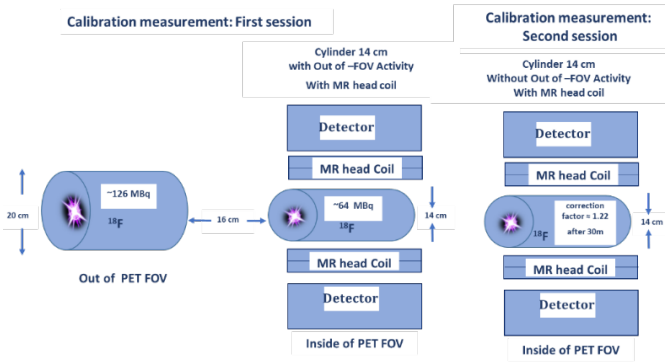

Figure 3.16 The placement of the phantoms for calibration measurements with the dedicated BrainPET. Right: first measurement, left: second measurement.

Table 3.2 The calibration probe measurements for the calibration measurements.

Measurement	Probe	Time	CPM	Volume
Calibration Bias: The phantom in FOV	1	10:42:00	330537	0.494 ml
	2	10:44:00	329162	0.499 ml
	3	10:45:00	321517	0.500 ml
Calibration Bias: The phantom out of FOV	1	10:47:00	413242	0.498 ml
	2	10:48:00	411249	0.500 ml
	3	10:50:00	407989	0.495 ml
CPM: counts per minute				

Table 3.3 The averages of the calibration probe measurements for all the decay experiments.

Measurement	Time	CPM	Volume
Calibration Bias: The phantom in FOV	10:43:67	327072	0.499 ml
Calibration Bias: The phantom out of FOV	10:48:33	410826.7	0.499 ml
CPM: counts per minute			

VI. Cross-Calibration

The block-pairwise DTC method requires a new calibration, as the calibration which is currently applied to the reconstructed images makes use of the global DTC method. Instead of the new calibration block-pairwise DTC method, we used a cross-calibration between the both methods. The cross-calibration factor has been computed by evaluating the differences in the reconstructed activity concentration in specific ROIs obtained with the different DTC methods. The obtained cross-calibration factor was found

to be 1.079 (ratio between ROI activity concentration with global DTC and ROI activity concentration with block-pairwise DTC) and was applied to all reconstructed images obtained with the block-pairwise method. Two measurement were used for this computation and evaluation. The first measurement was done with a homogenous cylinder with a 20 cm inner diameter and 19 cm length (volume: ≈ 5969 ml) and was filled with 99.6 MBq activity of ^{18}F diluted in water. The scan time was 20 minutes. The phantom was transversely centered with half of it inside of FOV and the second half outside of FOV. The measurement was done evaluate the homogeneity of the reconstructed, DT corrected images with MR transmit/receive head coil in order to evaluate the impact of the out-of-FOV activity under normal PET imaging conditions. For the second measurement a homogenous cylinder was used with 14 cm inner diameter and a length of 23.6 cm (volume: ≈ 3633 ml) filled with 99.6 MBq activity (decay corrected for 20 minutes of delay) of ^{18}F diluted

in water. The measurements of the calibration probes are summarized in table 3.5. Table 3.6 summarizes the averages of the calibration probe measurements for the values given in table 3.5. The phantom was transversely centered in the FOV. The phantom was axially centered to the extent that the dimensions of the MR transmit/receive head coil allowed. The duration of the acquisition was 20 minutes. Again, we measured the activity concentration of the phantom filling also with a well counter (3 probes).

Table 3.4 Measurements of the calibration probes for the cross-calibration measurement.

Measurement	Probe	Time	CPM	Volume
Cross-Calibration: The phantom in FOV	1	12:48:36	247214	0.494 ml
	2	12:49:44	248870	0.499 ml
	3	12:50:56	248713	0.502 ml
CPM: counts per minute				

Table 3.5 The average of the measurements of the calibration probes for the cross-calibration measurement.

Measurement	Time	CPM	Volume
Cross-Calibration: The phantom in FOV	12:49:45	248265.7	0.501 ml
CPM: counts per minute			

3.2.2 Volunteer & Patient Measurements

VII. [^{11}C]ABP688 Measurements

For the validation of the block-pairwise DTC method we reanalyzed time activity curves (TACs) and derived quantities such as BP_{ND} and V_T obtained with [^{11}C]-ABP688. The [^{11}C]ABP688 measurements have been previously used to investigate mGluR5 binding with and without cognitive task. (Régio Brambilla et al. 2020). For the this work, 8 image data sets from the [^{11}C]ABP688 cohort were chosen. All subjects were

male and between 24 and 50 years of age. Four of them were smokers and the rest were nonsmokers. Six subjects were healthy volunteers, two of them were diagnosed with schizophrenia. The [^{11}C]ABP688 data was collected from 2017 to 2019; the patients were recruited by Uniklinik RWTH Aachen; and the study was approved by the Ethics Committee of the Medical Faculty at the RWTH Aachen University and the German Federal Office for Radiation Protection (Bundesamt für Strahlenschutz). The [^{11}C]ABP688 PET acquisition had a duration of 65 minutes starting with the injection of the bolus. The bolus-infusion scheme protocol was optimized by injecting around 50% of the total activity with the bolus, followed by a constant infusion of the remaining activity at a rate of 92ml/h. A distribution equilibrium was observed after 30 min. The average total administered activity per subject was 525 ± 55 MBq (Régio Brambilla et al. 2020). Table 3.7 summarizes all the details of the [^{11}C]ABP688 cohort used in this study.

VIII. O-(2-[^{18}F]fluoroethyl)-L-tyrosine (FET) PET Measurements

The TACs and derived mean and maximum tumor-to-normal brain ratios (TBR_{max} and TBR_{mean}) were obtained from the O-(2-[18F]fluoroethyl)-L-tyrosine (FET) PET measurements. These consisted of twenty [^{18}F]-FET -PET measurements from patients with histologically confirmed cerebral gliomas. The [^{18}F]-FET measurements were used to compare the influence of the developed DTC on semi-quantitative parameters like mean tumor to background ratio (TBR_{mean}), maximum tumor to background ratio (TBR_{max}), and the TAC curve shape (Lerche et al. 2021). The PET data acquisition was dynamic from minute 0 to minute 50 post injection (p.i.) of the [^{18}F]-FET bolus. The [^{18}F]-FET measurements were performed with an average injected radioactivity of 220 ± 32 MBq. All measurements were done between 2017 and 2021 on the 3T MR-BrainPET insert. The static and dynamic [^{18}F]-FET-PET parameters were calculated. The age range of this cohort was (26-69 y), with 9 females

and 11 male subjects. Five patients had been diagnosed with Oligodendroglioma, ten patients had been diagnosed with Glioblastoma, one patient had been diagnosed with suspected Glioma, one patient had been diagnosed with brain metastases, one patient had been diagnosed with Astrocytoma, and two patients had been diagnosed with Oligoastrocytoma. Thirteen of the diagnoses corresponded to World Health Organization (WHO) grade III (mutant) and grade IV (wildtype) and five diagnoses corresponded to WHO grade II (Louis et al. 2016; Louis et al. 2021; Vigneswaran et al. 2015). For two subjects, the grade was unknown. All [^{18}F]-FET-PET measurements were approved by the local ethics committees and the relevant federal authorities and the procedures adhered to the standards established in the Declaration of Helsinki. All subjects gave prior written, informed consent for their participation (Lohmann et al. 2018). Detailed [^{18}F]-FET patient cohort characteristics are summarized in Table 3.8.

Table 3. 6 Details of the [^{11}C]ABP688 volunteer cohort.

Adapted from Issa et al. 2023

Subject #	Age (y)	Sex	Smoker/non Smoker	Volunteer/Patient(Initial Diagnosis)
1	24	M	non-smoker	Volunteer
2	49	M	Smoker	Volunteer
3	50	M	Smoker	Volunteer
4	37	M	non-smoker	Volunteer
5	25	M	non-smoker	Volunteer
6	47	M	Smoker	Volunteer
7	26	M	non-smoker	Patient (schizophrenia)
8	45	M	Smoker	Patient (schizophrenia)

IX. [^{15}O]H_2O PET Measurements

We evaluated the TACs of the cerebral blow flow (CBF) tracer [^{15}O]-labeled water in gray matter and white matter (CBF) and calculated the rate constants K1 and K2, and V_T by kinetic modeling. Four measurements of [^{15}O]H_2O PET collected in 2012 for a study on cerebral blood flow (Zhang et al.

2014). Four [^{15}O]H_2O bolus injections from four healthy volunteers were analyzed (4*4=16 reconstructed images). The fourth measurement of the [^{15}O]H_2O was done with the same volunteer as the third measurement but on another day. The acquisition time for each bolus injection was 180 seconds, data was acquired as list mode and 4 injections (half-life frames) of 180 seconds duration were used for reconstruction. The average bolus injection was 536.75 ± 2 MBq. All the subjects were male and the age range was 27-31 years. Table 3.9 resumes [^{15}O]H_2O measurement details for all volunteers. The study was approved by the ethics committee of the university hospital of the RWTH University Aachen and the federal authorities according to the Declaration of Helsinki's Ethical Principles for Medical Research Involving Human Subjects and the German radiation protection law. All participants gave prior written approval.

Table 3.7 Detailed [^{18}F]-FET patient cohort characteristics. Adapted from Issa et al. 2023.

Measurements #	Age (y)	Sex	Initial Diagnosis	WHO grade	IDH Genotype
1	59	F	Glioblastoma	IV	wildtype
2	67	M	Oligodendroglioma	III	mutant
3	59	M	Glioblastoma	IV	wildtype
4	35	F	Glioblastoma	IV	wildtype
5	49	M	Oligodendroglioma	II	mutant
6	26	M	Astrocytoma	III	mutant
7	39	M	Glioblastoma	IV	wildtype
8	48	M	Glioblastoma	IV	wildtype
9	56	M	Glioblastoma	IV	wildtype
10	62	F	Glioblastoma	IV	wildtype
11	50	F	Oligodendroglioma	II	mutant
12	44	M	Oligodendroglioma	III	mutant
13	55	F	Brain Metastases	-	-

14	54	F	Oligoastrocytoma	II	n.a.
15	54	M	Oligoastrocytoma	II	n.a.
16	69	M	Glioblastoma	IV	wildtype
17	44	F	Glioblastoma	IV	wildtype
18	50	M	Oligodendroglioma	II	mutant
19	60	F	Suspected Glioma	unknown	unknown
20	44	F	Glioblastoma	IV	wildtype
n.a. = not available					

Table 3.8 The [^{15}O] water PET measurements data.

Measurements #	Age (y)	Sex
1	27	M
2	31	M
3	29	M
4	29	M

3.3 Data Analysis

3.3.1 Phantom Measurements

The images were reconstructed with the 3D OP-OSEM algorithm for the performance evaluation of the result of the phantom measurements (Mourik et al. 2010; van Velden et al. 2008). The image volume matrix was 256 x 256 x 153 pixels with two subsets, 32 iterations, and an isotropic voxel size of 1.25 mm^3. In addition to the DTC, the data sets were corrected for decay, randoms, attenuation (Kops et al. 2014), and scatter. The corresponding phantom measurements were reconstructed using global DTC, without any DTC, and with the proposed block-pairwise DTC method. The results of the block-wise DTC method showed, that the accuracy of this method was not sufficient. Therefore, the method was abandoned and images were reconstructed for comparison with the global DTC (see 4.2 in the results chapter). Reconstructed images were only generated for the method with sufficient accuracy, i.e. the block-pairwise DTC

method, and also for the global DTC, and without any DTC for comparison. No further data processing was done for the phantom measurements. Constant true coincidence count rate framing schemes were used in all reconstructions in order to minimize reconstruction bias at low count rates (Brambilla et al. 2021; Régio Brambilla et al. 2020).

I. Germanium (^{68}Ge) Phantom Measurement

The ^{68}Ge phantom measurement was only used to characterize the CFD counts contained in the list-mode data.

II. Decay Experiment

The decay experiment without out of FOV activity was used to define the coincidence pairs and to evaluate the block-wise and block-pairwise methods. For this step, it was not necessary to reconstruct the images.

III. Decay Experiment Measurement with Activity Out of FOV

The decay experiment with out of FOV activity was used to define the coincidence pairs and to evaluate the block-wise and block-pairwise methods, and to prepare for the next measurement with three compartment phantom. For this step, it was not necessary to reconstruct the images.

IV. Three Compartment Phantom Measurement

Five cylindrical ROIs were specified in each compartment to enable the evaluation of accuracy and noise level. The same dimensions were used for all ROIs, i.e. $\varnothing_x \approx 44$ mm, $\varnothing_y \approx 44$ mm, and length $l_z \approx 8$ mm. The ROIs were aligned with the compartment's centric axis (again for all 48 time frames). The ROIs were placed in the center, front, and the back of the phantom (see figures 4.40 and 4.41 in the results chapter). The two ROIs that were not centered in the axial direction were 1cm and 2

cm away from the edges, respectively. Those two ROIs were chosen to find the difference between the 1 and 2 cm positions, which may be affected by the other variables.

V. Calibration Bias

Three cylindrical ROIs were drawn in the center, front, and the back of the phantom image (ROI surfaces at 1 cm from the edges). The ROIs at the front and the back of the phantom have the same distance from the iso-center. Those ROIs were applied to the two measurement sessions. For the first calibration bias measurement, three cylindrical ROIs were drawn and the dimensions of the ROIs were $\varnothing_x \approx 170$ mm, $\varnothing_y \approx 170$ mm, and length $l_z \approx 21$ mm. For the second calibration bias measurement, three cylindrical ROIs were drawn and the dimensions of the ROIs were $\varnothing_x \approx 170$ mm, $\varnothing_y \approx 170$ mm, and $l_z \approx 21$ mm. The ROIs were aligned at the scanner axis for all image frames (20

minutes in length). The averaged activity concentration values were computed in the ROI analysis.

VI. Cross-Calibration Measurement

The cross-calibration factor was measured using a single cylindrical ROI placed inside of the FOV. The ROI was centered, and it covered the mayor part of the volume of the phantom in the x, y, and z directions. It´s dimensions were $\varnothing_x \approx 98$ mm, $\varnothing_y \approx 97$ mm, and $l_z \approx 125$ mm. The surfaces of the ROI were 1 cm from the edges. The ROI was aligned at the scanner axis for all image frames (20 minutes in length). Figure 3.17 shows the single ROI together with the image of the phantom.

The averaged activity concentration values were used for the computation of the cross-calibration factor.

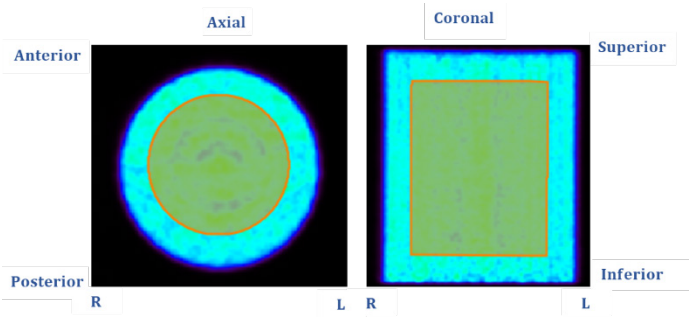

Figure 3.17 The single ROI placement together with the phantom image used in the cross-calibration factor computation.

For all the previous phantom measurements, the ROIs analysis was done with AMIDE (Amide's a Medical Imaging Data Examiner software) (Loening & Gambhir 2003). The values used for the ROI analysis are the averaged activity concentration for each frame and the coefficient of variation (COV) except for the calibration measurements, in which we used the averaged activity concentration only.

The noise levels of the reconstructed images were quantified using the COV. The COV was calculated by dividing the standard deviation (σ) by the mean

of the activity (μ) of the voxel values inside the ROI as in equation 3.20 below (Centore 2016):

$$COV = \frac{\sigma}{\mu} \qquad (3.20)$$

The mean of the activity was calculated for obtaining the cross-calibration factor of the reconstructed images that used the block pairwise DTC method and for the comparison to the mean of the activity concentration in the reconstructed images using the global DTC method.

3.3.2 Influence of scattered coincidences

The scatter sinograms of the phantom measurements were computed to estimate variability introduced by scatter correction into the ROI analysis. As for two measurements with the same phantom, we have necessarily two different scatter corrections, even if the object dimensions and the activity in the phantom are the same.

We need to get an estimate of how much of the reconstructed activity concentration in the reconstructed image can vary from one measurement to the next due to the scatter correction. For this purpose, we split one measurement from a homogeneous phantom into reconstruction frames containing the same number of true coincidence counts and analyzed the scatter sinograms obtained with the SSS algorithm and tail fitting. For the analysis, all scatter sinogram entries of a single slice were summed for all 1399 sinogram slices (see figure 3.18 a and b) and we computed the COV for all slices from the different frame values (see figure 3.18 c). This was done for the global and block-pairwise DTC method and for the measurement III, which is the decay experiment with out of FOV activity.

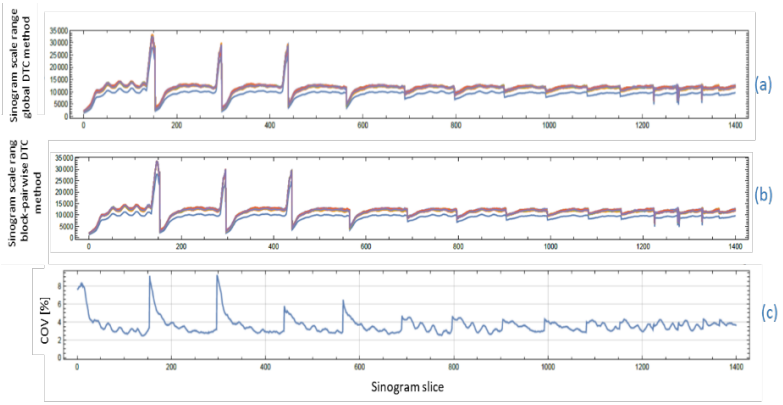

Figure 3. 18 Slice wise variation of the scatter sinograms: a: The slice-wise total of the entries of each sinogram slice for the different frame (different line colors, not separated in this plot) of the global DTC method, b: The slice-wise total of the entries of each sinogram slice for the different frame (different line colors, not separated in this plot) of the block-pairwise DTC method, c: the COV values for the individual scatter sinogram slices.

3.3.3 Volunteers & Patients Measurements

VII. [^{11}C]-ABP688 PET images

For the [^{11}C]ABP688 measurement, constant true coincidence count rate framing scheme was used to minimize reconstruction bias at low counts (Issa et

al. 2022; Brambilla et al. 2021; Régio Brambilla et al. 2022). The analysis of the [^{11}C]-ABP688 PET images was done with PMOD (version 4.103, PMOD Technologies, Zurich, Switzerland), using the PNEURO package. A 3D Gaussian post-reconstruction filter (2.5 mm) was applied. The PET data set was corrected for motion, normalized, and matched to the simultaneously acquired MR T1 MPARGE image. The ROIs were drawn using the T1 MPARGE images as an anatomical reference. Figure 3.19 shows the targets ROIs of the [^{11}C]-ABP688. Three exemplary regions of the human brain were chosen for the analysis based on their relevance: cerebellum gray matter, temporal posterior cortices, and the anterior cingulate cortex (ACC). All the reconstructed images were normalized to the Montreal Neurological Institute (MNI) space and the Hammers atlas (Hammers et al. 2003). The cerebellum gray matter (GM) was used as a reference region for the [^{11}C]ABP688 study (Régio Brambilla et al. 2020; Akkus et al. 2018).

The TACs and the derived quantities, i.e., the non-displaceable binding potential (BP_{ND}), and distribution volume (V_T) were also analyzed. The BP_{ND} was computed by dividing the mean activity in the target region by the mean activity concentration in the reference region i.e., the cerebellum gray matter, and subtracting the value of 1.0, as in model (3.21):

$$BP_{ND} = \left[\frac{C_{max-region}}{C_{reference}}\right] - 1 \qquad (3.21)$$

Here $C_{max-region}$ is the concentration of the bound radioligand, $C_{reference}$ is the nondisplaceable ligand concentration in this case (cerebellar GM, reference tissue). The V_T is computed by building the ratio of the tracer concentration in the target tissue to the concentration in the plasma at equilibrium as in equation (3.22) (Morris et al. 2004; Innis et al. 2007; Slifstein & Laruelle 2001):

$$V_T = \frac{C_{region}}{C_{Plasma}} \qquad (3.22)$$

Here the C_{region} is the concentration of the radioligand in tissue target region. The C_{Plasma} is the concentration of the radioligand in the plasma at equilibrium.

The slope of the V_T and the BP_{ND} during equilibrium (t > 30 min.) was computed with linear regression. A detailed description of the volunteer measurements with [^{11}C]ABP688 can be found in (Brambilla et al. 2021; Rajkumar *et al.* 2021). The cross-calibration factor was applied for the block-pairwise data of all the measurements estimated quantities for [^{11}C]ABP688.

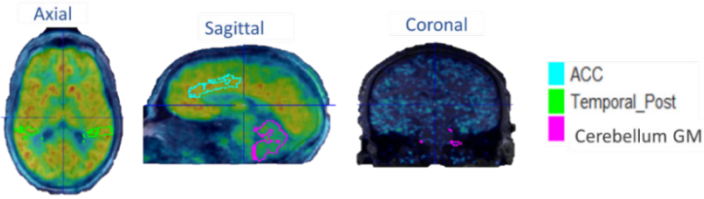

Figure 3.19 The [^{11}C]ABP688 three relevant regions of the human brain: Cerebellum, temporal posterior cortices and the ACC. Adapted from Issa et al. 2023.

VIII. O-(2-[^{18}F]fluoroethyl)-L-tyrosine (FET) PET Measurements

In the case of the dynamic data set analysis of [^{18}F]-FET-PET images, the images were reconstructed using 16 time-frames (5×1 min; 5×3 min; and 6×5 min). Sum image from 20-40 min p.i. were used and the SUV were obtained by dividing the radioactivity concentration (kBq/mL) in the tissue by the ratio of the injected radioactivity and the body weight (See equation 1.3 in the first chapter).

The analysis of the [^{18}F]-FET-PET images was done with PMOD (version 4.103, PMOD Technologies, Zurich, Switzerland). A 3D Gaussian filter (2.5 mm) was applied to all images and the PET data set was corrected for motion and normalized. A spherical volume of interest (VOI) of constant size (dimeter was 15 mm) was drawn at the contralateral side of the tumor area as healthy reference. 3D segmentation with PMOD was used to delineate the tumor volume by assigning all voxels with a TBR of 1.6 or higher to the tumor volume. The shapes of the

TACs derived from the reconstructed images were evaluated by curve fitting with a linearized TAC model for [^{18}F]-FET (Lerche et al. 2021). Figure 3.20 shows one of the [^{18}F]-FET-PET images with the relevant VOIs of the normal tissue, the tumor, and the maximum concentration of the uptake in the tumor area, and the therapy target which is the same as the treated volume (TV). The TV includes the real Gross volume (GTV), Clinical volume (CTV), Planning volume (PTV) and some surrounding of normal tissue (Berthelsen et al. 2007; Grosu et al. 2006).

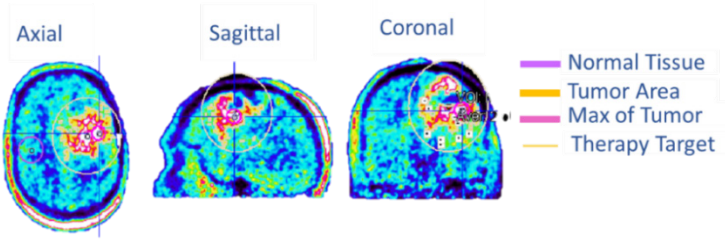

Figure 3.20 [^{18}F]-FET-PET images with the relevant VOIs of the normal tissue, the tumor, the maximum concentration of the uptake in the tumor area, and the therapy target. Adapted from Issa et al. 2023.

The TBR_{max} and TBR_{mean} for the times between 20 min. and 40 min. p.i. were computed for all cases. The TBR_{max} was calculated by dividing the maximum of the SUV of the tumor VOI (which was created by the threshold mask in POMD) by the mean of the SUV of the healthy tissue VOI. The voxels number of the peak area was 1021 voxels, which was fixed by using the Max VOI tool in PMOD, the mean uptake covered a 2 cm sphere centered at maximum voxel in the tumor VOI (Filss et al. 2017).

In contrast, the TBR_{mean} was calculated by dividing the mean SUV of the tumor VOI by the mean SUV of the reference VOI (healthy tissue). Mean relative differences of TBR_{max} and TBR_{mean} for different DTC method were compared. The block-pairwise DTC method lead to sufficiently accurate results (See results and discussions chapters). For that, the TBR_{max} and TBR_{mean} were compared in the block-pairwise DTC and global DTC for the times between 20 min. and 40 min. Further, TBR_{max} and TBR_{mean} were computed and we tested for a potential

correlation between the tumor size and the distance of the tumor concerning the brain center point and the difference in the DTC methods.

The distance was obtained with the data inspector tool in the POMD measuring the distance from the mid-center point of the brain to the tumor area (peak center VOI). The tumor size was obtained with the ISO-contouring VOI tool at a threshold level relative to uptake in PMOD (version 4.103, PMOD Technologies, Zurich, Switzerland). As not all values were distributed normally, the Spearman-Rank correlation test was used instead of the Pearson´s correlation test. The cross-calibration factor was applied for the block-pairwise data of all the measurements and the corresponding estimated quantities for [^{18}F]-FET-PET.

IX. [^{15}O]H_2O Measurements

The images of [^{15}O]H_2O measurements were reconstructed using the constant true coincidence count rate framing schemes for stabilizing and

minimizing reconstruction bias (Issa et al. 2022; Brambilla Issa et al. 2021; Régio Brambilla et al. 2022). The data analysis of the [^{15}O]H_2O measurements was done with PMOD (version 4.103, PMOD Technologies, Zurich, Switzerland). A 3D Gaussian post-reconstruction filter (4 mm) was applied to the reconstructed images. The VOIs covering the GM and the WM were drawn manually for each subject with sufficient distance from tissue borders in order to minimize partial volume effects (PVE) (Yang et al. 2017; Meechai et al. 2015) and in order to allow validation against results obtained in original work (Zhang et al. 2014). Figure 3.21 shows one of the [^{15}O]H_2O measurements with the manually drawn VOIs which were used for the GM and WM. The measured TACs have been used to compute the cerebral blood flow (CBF), the rate

constants K_1 and k2, and the V_T via kinetic modeling (Morris et al. 2004; Bol et al. 1990).

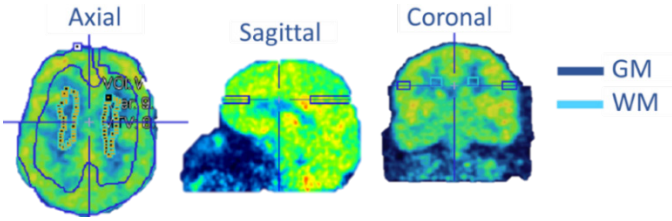

Figure 3.21 The $[^{15}O]H_2O$ measurement with the manually drawn VOIs for the GM and WM.

K_1 is the unidirectional transport of the radioactive tracer from the plasma to the tissue compartment and is given by equation 3.23 (Gunn et al. 2001):

$$K_1 = \mathfrak{f}\left(1 - e^{-\frac{ps}{\mathfrak{f}}}\right) \qquad (3.23)$$

Here, the $\mathfrak{f}$ is the perfusion, ps is the product of the capillary permeability and the capillary surface. k_2 is unidirectional transport of the tracer back from the tissue to the blood and is given by equation 3.24 (Gunn et al. 2001):

$$k_2 = \frac{K_1}{V_T} \qquad (3.24)$$

The Kinetic modeling was performed with PMOD (version 4.103, PMOD Technologies, Zurich, Switzerland). We also computed the ratio between GM and WM. The cross-calibration factor was applied to the block-pairwise data for all measurements and corresponding estimated quantities for [^{15}O]H_2O.

4. Results

The evaluation of the three investigated DTC methods give rise to a variety of results. The global DTC showed significant insufficiencies with respect to accuracy and the block-wise DTC method was found to be inappropriate to improve the accuracy of the DTC for the BrainPET. For the evaluation we put high emphasis on the quantitative accuracy of the BrainPET images. However, the block-pairwise DTC method was found to lead to a significant improvement and was closest to the ideal case without any DT losses when compared with the other two methods. This chapter presents the most important results obtained with the three DTC methods used together with the dedicated Siemens 3T MR BrainPET insert. These results were obtained with phantom measurements and then from reconstructed images of patient and volunteer measurements.

4.1 Global DTC Method

The global DTC method was developed and studied previously (Weirich et al. 2013; Weirich et al. 2012). In our work, we used his findings for comparison with alternative DTC methods and a detailed study of the limitations of the global DTC method. The PET scanner consists of 192 detector blocks in 32 cassettes and six rings. The CFD count rates (non-validated singles) vary for each block depending on its physical position near or far from the radioactivity sources (patients or phantoms). The highest count rates of non-validated singles were found in the blocks nearest to the radioactivity sources, especially in the first ring of the detector. For comparison, figure 4.1 shows how the non-validated single counts in a single cassette (head) are distributed over the six individual blocks for the same time interval and the same phantom.

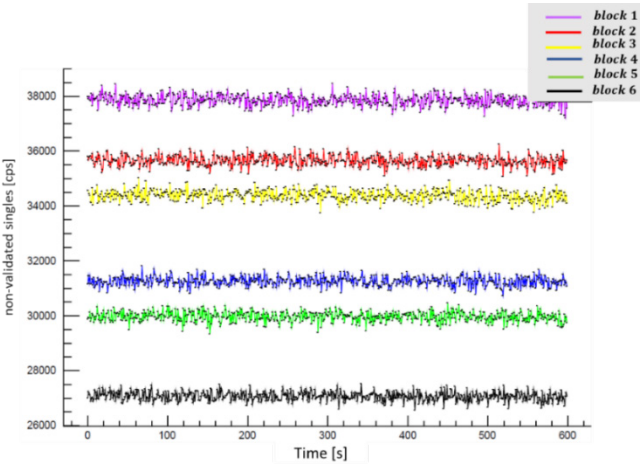

Figure 4.1 Non-validated single counts in a single cassette (head) are distributed over the six individual blocks measured with the ^{68}Ge phantom during 600 seconds.

The highest CFD count rates were found in block number one since it is located in the first ring. The lowest CFD count rates were found in block number six and ring six, which is located on the rear side of the insert and therefore comparatively far away from the radioactive source. Here it is important to mention, that the phantom is not centered along axial direction and therefore the centroid of the activity

was not centered at the middle of the FOV. Instead, it is displaced by around 2 cm from this center. Therefore, the rear rings of the BrainPET are further away from the radioactive source. It can be further seen in figure 4.1 that the count rates of the individual blocks are highly correlated with the position of the ring they belong to (see figure 3.3 in the methods chapter), which can be explained by the solid angle corresponding to the physical position of the individual block with respect to the source. The same effect can be observed in the non-validated single count rates obtained from volunteer measurements. Figure 4.2 shows the non-validated singles for all individual 192 blocks of the BrainPET insert during the first 60 seconds (p.i.) for a [^{18}F]-FET-PET measurement.

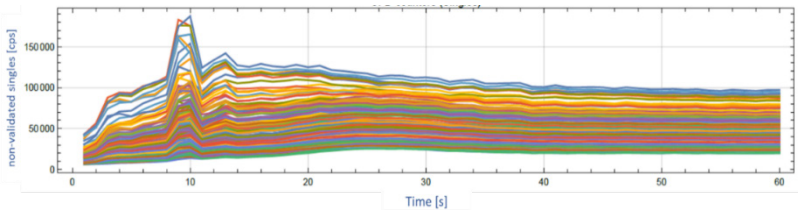

Figure 4. 2 The non-validated singles for all individual 192 blocks of the BrainPET insert during the first 60 seconds (p.i.) for a [^{18}F]-FET-PET measurement.

For the patient and the volunteer measurements, the blocks detectors are exposed to radiation from both the brain volume (inside of the FOV) and the remainder of the body (outside of FOV). In comparison to whole-body PET scanners, the irradiation from outside the FOV is very unsymmetrical and moreover, for reasons of MR compatibility, the BrainPET insert has no shields to reduce the radiation from outside the FOV. Figure 4.3 shows the DT corrected, non-validated singles used by the global DTC method for ring number one, ring number six, and the average of all six rings of the BrainPET Insert, during the first 50 seconds of a [^{18}F]-FET-PET measurement.

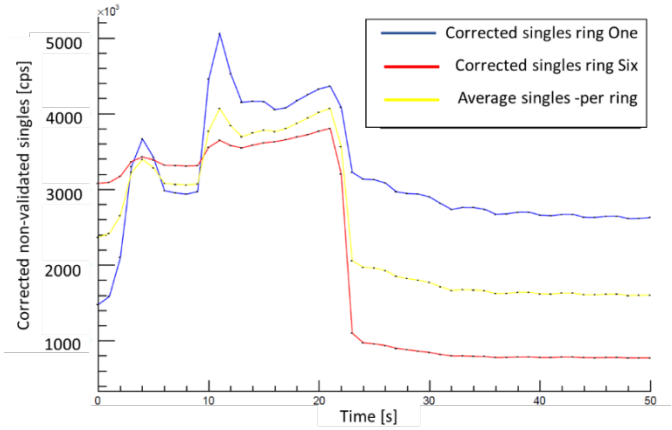

Figure 4. 3 DT corrected, non-validated single count rates used by the global DTC method for ring number one, ring number six, and the average of all six rings during the first 50 seconds of a [^{18}F]-FET-PET measurement.

Three peaks in figure 4.3 are caused by the bolus of the injected tracer passing close by the detectors. There are two main blood circulations in the human brain called the "anterior" and the "posterior" circulation and the blood enters the brain volume through the internal arteries, which are the Vertebral arteries on the posterior side and the internal Carotid arteries on the anterior side (Veenith & Menon 2011; Chandra et al. 2017). The first peak in figure 4.3 at ≈

5 seconds p.i. is caused either by the bolus passing close by the detectors after the injection in the vein of the arm or by the bolus entering the lung after passing the heart. The bolus enters the brain at ≈ 10 seconds p.i. (second peak) and leaves the brain at ≈ 22 seconds p.i. The count rates in ring one are significantly higher than those in the other rings, since it is more exposed to the activity from outside of the FOV (the patient's body). The average count rates of the six rings (yellow line) deviate significantly from the count rates observed in the first and the sixth ring. As the average count rates are used as reference in the global DTC the observed deviations necessarily affect the accuracy of the global DTC method since the differences in the count rates for each block are ignored. As part of this work, I studied the impact of the tracer's half-life and the impact of the velocity at which the biodistribution is changing. As will be shown, understanding this impact of the different DTC methods is highly relevant for the quantitative interpretation of the PET different applications. Figure 4.4 shows the block-wise DTC factor for individual blocks (in different rings) of one cassette

in comparison to the non-validated singles for each individual block measured during an [^{11}C]ABP688 volunteer examination.

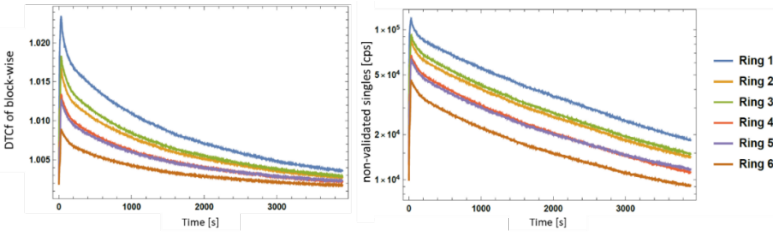

Figure 4.4 Left: Block-wise $DTCf_{Block-wise}$ for each block (in different rings) of one cassette (head), Right: non-validated singles for each block of the former cassette. Both are obtained from an [^{11}C]ABP688 volunteer measurement.

Table 4.1 Gives the derived dead time constants for the blocks which have been considered in Fig. 4.4. Here we present the DT constants only for six blocks. All 192 blocks have very similar DT constants, the complete table is given in the appendix (see table A.1).

Table 4.1 Dead time constants of the six blocks of one cassette.

Block ID	1	2	3	4	5	6
Dead Time [ns]	195	193	195	196	197	191

The global DTC method used the average CFD count rates as reference for computing the global DTC factor. As the results form phantom and volunteer measurements above have shown, the method ignores the significant differences in the count rates of the individual blocks. However, these observed large differences are object dependent and affect the quantitative accuracy of the BrainPET images by introducing variable bias. Therefore, the methods that consider a block-wise DTC correction have been investigated in this work in order to improve the quantitative accuracy of the Siemens 3T MR BrainPET insert detector.

4.2 Block-wise DTC Method

The block-wise DTC method has shown more consistent results in comparison to the global DTC method when considering non-validated singles on the level of individual blocks. An Independent DTC factor for each individual block was computed, thus allowing to consider count rate differences on block level when correcting the dead time losses. However, the block-wise DTC method also failed to accurately correct the total prompt count rates for the dead time losses, which was caused by several effects affecting the prompts count rates which are not adequately accounted for with the block-wise DTC method. These effects have been studied in detail in order to further improve the DTC. Figure 4.5 shows the measured non-validated singles of a single block together with the best fit (non-paralyzable DT model, with exponential decay and constant offset, i.e. equation 3.6) for the radioactive decay phantom measurement with ^{18}F. Figure 4.6 shows the relative fit residuals for the data and best fit in figure 4.5.

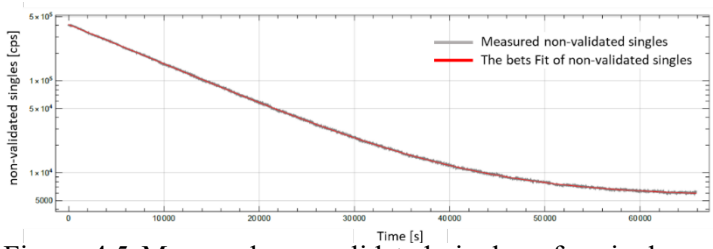

Figure 4.5 Measured non-validated singles of a single block together with the best fit (red line) using equation 3.6. The observed best fit parameters were $S_0 = 437280 \pm 55$, $\tau = 1.839 \cdot 10^{-7} \pm 5 \cdot 10^{-10}$, $O = 5588 \pm 2$.

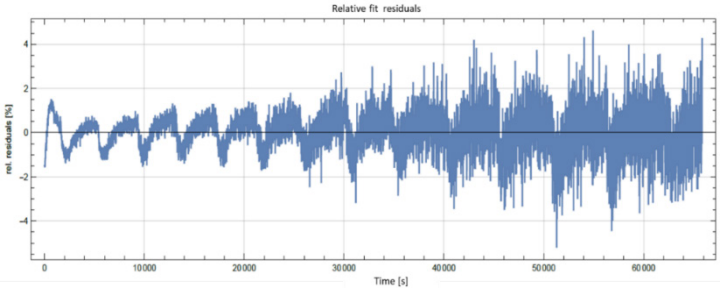

Figure 4. 6 Relative fit residuals for the data and best fit in figure 4.5.

It can be seen from figure 4.6, that there are systematic variations in the relative fit residuals for when fitting the non-validated singles of the

individual block[2] with the block-wise DTC model (equation 3.6). Although the origin of these variations are not known, the accuracy of the best fit would have been acceptable in the explored count rate range. Figure 4.7 shows the corresponding DTC factor for the non-validated singles for a single block ($DTCf_{Block-wise}$, equation 3.7) for this ^{18}F phantom measurement. Figure 4.8 shows the measured and ideal true count rates, the non-validated single count rates, and the values of $DTCf_{Block-wise}$ for a single block obtained with the same phantom measurement.

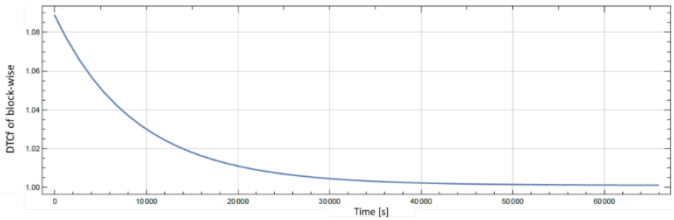

Figure 4.7 Correction factor $DTCf_{Block-wise}$ for the non-validated singles for a single block for this ^{18}F phantom measurement.

[2] Results only for one block shown. Results from all other 192 blocks are very similar.

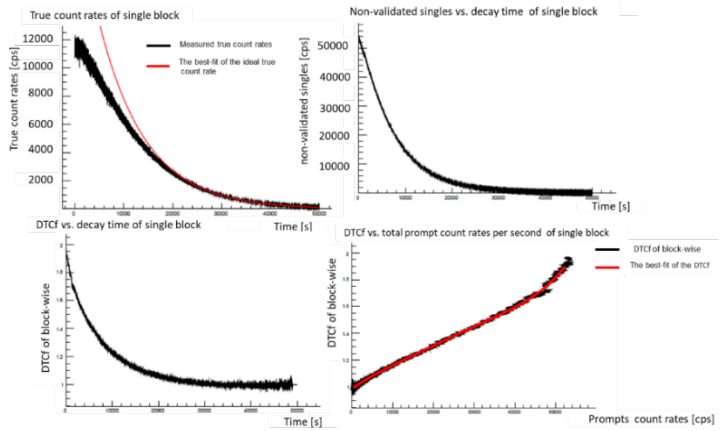

Figure 4.8 Upper left plot: The measured true count rate in a single block (black line) together with the ideal true count rate (red line), i.e. fit of measured counts of the range we used and extrapolation to the other times. Upper right: The measured total non-validated single count rates for the same single block. Lower left plot: the corresponding factors $DTCf_{Block-wise}$. And lower right plot: the corresponding $DTCf_{Block-wise}$ as a function of the total prompt count rate in the same single block. All data was obtained from the ^{18}F phantom measurement (equation 3.1).

The validation of the block-wise DTC method has been done experimentally with phantom measurements, and the results revealed that the block-wise single count rates follow the non-paralyzable DT model (NP_{DT}) with high precision. For the NP_{DT}, the measured average block-wise DT constant was found to be approximately 200 ns for all blocks. This is an important result, since it proves the assumption, that only the different count rates cause the different dead time losses, but not potentially different dead time constants (the time for which the block is dead due to a single detected event and during which it cannot not process any new event). For the patient measurements, the count rates of the 192 blocks depend strongly on the angular and axial block positions. Figure 3.9 shows the prompt count rate together with the best fit using the non-paralyzable DT (NP_{DT}) model (equation 3.8) in a single block. Figure 4.10 shows the all the different count rates for single block for the ^{18}F phantom measurement.

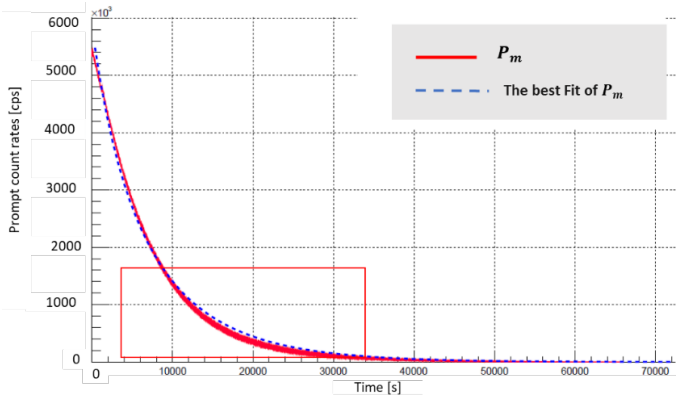

Figure 4. 9 Prompt count rates together with best fit using the non-paralyzable DT (NP_{DT}) model in a single block. P_m are the measured prompt count rates for the single block.

The block-wise DTC method results show that the DT losses vary for each block detector, this is based on the various count rates caused by the block position and the activity distribution (see figure 4.10).

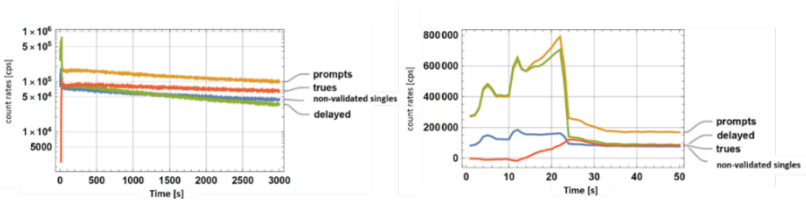

Figure 4.10 The different count rates for prompts (yellow), delayed (green), trues (orange), and non-validated singles (blue) for single block obtained with the ^{18}F phantom measurement. The right plot shows the same data as the left, but for the first 50 seconds only (bolus).

As can be seen from figure 4.9, the non-paralyzable DT fit model (equation 3.8) was not sufficient for describing accurately the total prompt count rates in individual blocks level, as the Prompts are the sum of trues and randoms, the trues are proportional to the activity while the randoms are proportional to the square of the activity. For this reason, and as the fractions of trues and randoms in the prompt coincidences are generally not known, the simple non-paralyzable model (equation 3.8) with decay and ^{176}Lu background (offset) could not model the prompts. Moreover, we accounted for the ^{176}Lu

background in the models with the parameter 0. The amount of scatter is proportional to the amount of prompt coincidences. However, the scatter contribution depends on the position of the ROI in the phantom (see 5.2 in the discussion). Figure 4.11 shows the prompt count rates together with the best fit and the relative fit residuals obtained with the non-paralyzable (NP_{DT}) model in a single block and for the ^{18}F decay measurement. The unqualified singles follow both the paralyzable and the non-paralyzable DT model. This is not a contradiction, since the presented work was done in a prompt count rate range, in which the Siemens 3T MR BrainPET insert is normally operated and in which both models behave very similarly (see figure 1.10 in the introduction). DTC of the coincidences based on block-wise dead time estimated with unqualified singles (CFD counters) has been proven to be insufficient because the energy window applied together with the coincidence search leads to additional count loss, which is not correctly modeled in the block-wise dead time evaluation with unqualified singles. Thus, the block-wise DTC

losses of the coincidences cannot be estimated correctly using with the prompt or true count rates, however, the delayed random coincidences undergo the same processing as prompts and have a well-defined quadratic dependency on the activity in the FOV.

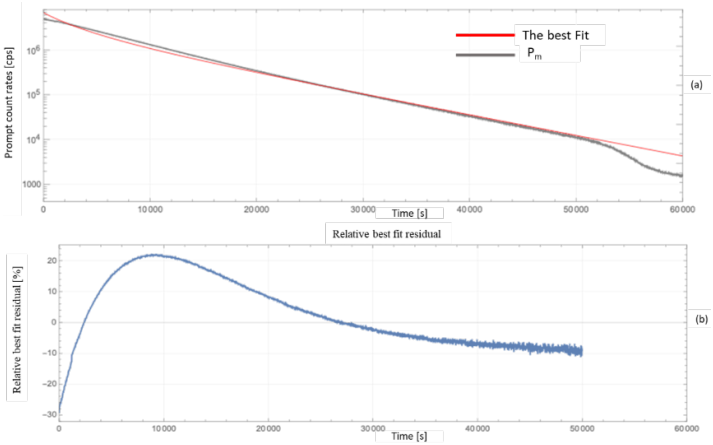

Figure 4.11. a: Measured prompt count rates together with the best fit using the non-paralyzable (NP_{DT}) model in a single block for the ^{18}F decay measurement. P_m are the measured prompt count rates, b: The relative best fit residual of the data shown in figure a. The prompt count rates measured after 50000 seconds have been excluded from the fit because of the known incorrect behavior of the peak-following automatic at low activities (see section 4.3).

Figure 4.12 shows the true count rate together with the best fit using the non-paralyzable (NP_{DT}) model

for a single block for the ^{18}F decay phantom measurement and the corresponding relative residuals. From these results, it became clear, that the block-wise DTC method was not sufficient to accurately correct the DT losses for true coincidences on the individual block level. We further observed during the phantom measurements with the Siemens 3T MR BrainPET insert, that one additional important issue was, that running MR sequences can affect the results of block-wise dead time correction, since the CFD counters are prone to interference with MR sequences, i.e. they lead to spurious triggers and therefore erroneous count rates.

The block-pairwise DTC method was identified as a potential method for realizing block-wise DTC which does not need access to qualified single count rates and which overcomes the mentioned difficulties. The method was successful in correcting DT losses of the true coincidence count rates when applied to the Siemens 3T MR BrainPET

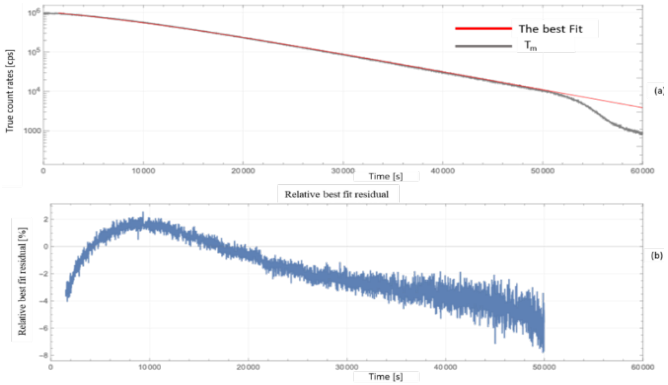

Figure 4.12 a. The true count rates together with the best fit using the non-paralyzable (NP_{DT}) model in a single block, T_m are the measured true count rates, b shows the relative best fit residuals for the data shown in a. The true count rates measured after 50000 seconds have been excluded from the fit because of the known incorrect behavior of the peak-following automatic at low activities (see section 4.3).

insert. However, as the method may amplify the image noise, the noise propagation into the reconstructed images was studied also. Further for the block-wise DTC method, we observed that the random triple coincidences are counted in the Siemens 3T MR BrainPET insert as two double coincidences, which interferes with the DT

measurement and correction, for that, we addressed this issue to get a precise DTC and applied additionally random triple corrections.

4.3 Block-pairwise DTC Method

4.3.1 Estimation of ideal delayed random coincidence count rates

As will be shown, the block-pairwise method was successful in correcting DT losses of the true coincidence counts with high accuracy, when applied to the Siemens 3T MR BrainPET insert. Figure 4.13a shows the measured delayed random count rates together with the best fit using the model for the ideal delayed random count rates (equation 3.15) in the time interval from 14500-24500 seconds. Figure 4.13b shows the same data as figure "a", but extrapolating the best fit of the delayed random count rates to the entire time interval. Figure 4.13c shows the relative fit residuals for best fit and the same data and as in figure a.

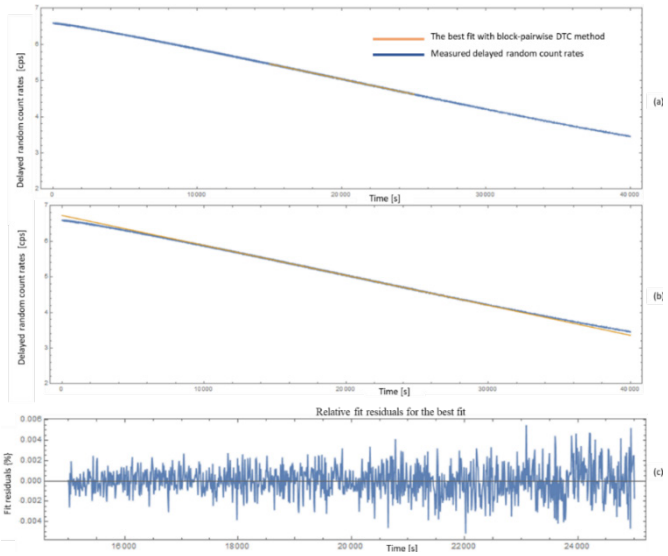

Figure 4.13. a: Measured delayed random count rates together with the best fit using the model for the ideal delayed random count rates in the time interval from 14500- 24500 seconds. The following best fit parameters were observed $R_O \approx -0.000084$ and $\tau \approx 6.7264$. b: Same data as figure a, but extrapolating the best fit of the delayed random count rates to the entire time interval. c: relative fit residuals for the best fit and the same data and as in figure a.

Figure 4.14 shows the ratio of the estimated ideal delayed random count rates and the measured delayed random count rates (D_{ideal} /D_m). For the block-pairwise DTC method, this ratio is used to derive the correction factor $DTCf$. The $DTCf$ becomes smaller than 1 after approximately 30000 seconds , which means that we have the DT gains instead of DT losses. This is an artifact of the peak finding algorithm implemented in the BrainPET insert at low count rates (to compensate for APD gain changes due to varying temperatures, the photo peak position of 511 keV radiation is continuously being analyzed and corrected, which leads to erroneous corrections caused by the Lutetium background at low activities in the FOV). Therefore, at very low count rates, we set the correction factor to 1 at about 4 counts per second.

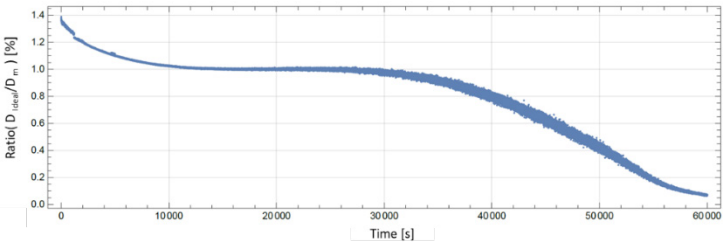

Figure 4.14 Ratio of the estimated ideal delayed random count rates and the measured delayed random count rates.

Figure.4.15 shows the observed true count rates together with the estimated ideal true coincidnece count rates. The latter were estimated by fitting and extrapolation as described above using the true coincidences from all head pairs.

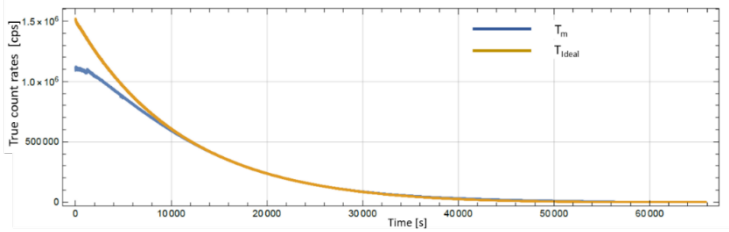

Figure 4.15 Measured true count rates (T_m, blue line) together with the estimated ideal true coincidnece count rates (T_{Ideal}, yellow line).

4.3.2 Triples Correction

As will be shown, the block-pairwise DTC method was successful in accurately correcting DT losses with the dedicated Siemens 3T MR BrainPET insert. Adding a correction for detected triple coincidences leads to higher accuracy. This makes the block-pairwise DTC method outperform the currently used system-wide dead time correction (global DTC method). The validation of the block-pairwise DTC method with phantom measurements showed a very good agreement between expected total true counts and measured and corrected true counts. As shown in the methods chapter, triples correction is potentially needed since the Brian PET does not reject triple coincidences, but counts them as two doubles leading to an overcounting which needs to be corrected. Figure 4.16a displays the total prompt coincidences, i.e. doubles (normal coincidences, triples and multiples) against the total prompt coincidences only containing doubles, which is a good estimate for the real activity in the PET FOV.

Thi figure shows, that the emperical model (equation 3.16), is a sufficiently good approximation for estimating the overcounts due to triple coincidences, although the fit residuals in figure 4.16 “b” still present noticealbe systematic variatons. The data shown in both figures were obtained a decay experiment with ^{18}F. Figure 4.17 (a) shows the measured delayed random coincidences with triple correction (D_{om} with triples) together with the best fit using the paralyzable DT model together with triple correction (equation 3.17) for one out of the 10944 block-pairs. Figure 4.17 “b” shows the relative fit residuals for the same data shown in figure 4.17 “a”. Note that there is no apparent systematic variation in the fit residuals. The data for figures 4.17 “a and b” were obtained from a phantom experiment with decaying ^{18}F in the Siemens 3T MR BrainPET insert scanner.

Figure 4.18 “a” shows the measured delayed random coincidences together with the best fit (equation 3.17) and its extrapolation for estimating D_{ideal}. Figure 4.18 “b” shows the relative fit residuals for

the same data and Figure 4.18 “c” DT correction factor with correction for triple coincidences, but without setting the factor to 1 for low counts. These results were obtained assuming non- paralyzable behavior for one out of 10944 block-pairs and using decaying ^{18}F in a phantom acquired with the Siemens 3T MR BrainPET insert.

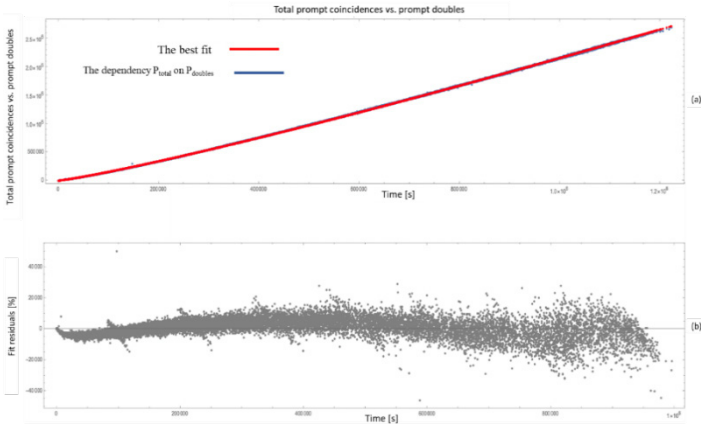

Figure 4. 16 a: The best fit (red line) with an exponential model for the dependency of total prompt coincidences on the total prompt coincidences only containing doubles. The following best fit parameters were observed: $m = 0.2787 \pm 0.0002$, $\kappa = 1.14819 \pm 0.00004$ b: The fit residuals for the best fit and the same data and as in figure a.

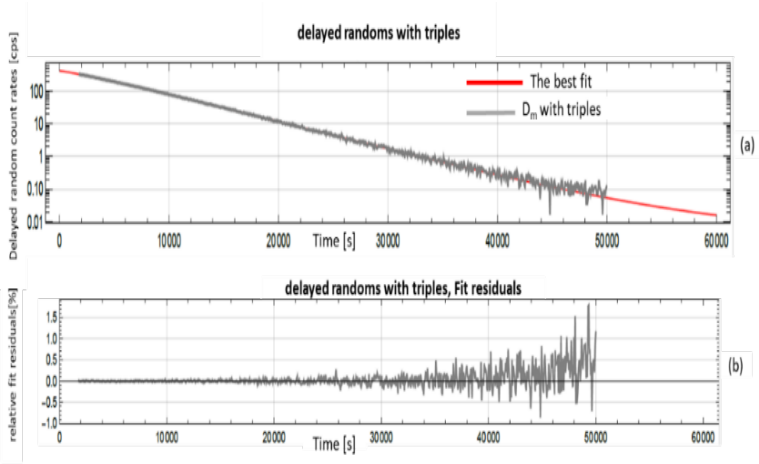

Figure 4.17 a: The fit result (red line) of the measured random with triples (gray line), b: The fit residuals of the averaged corrected delayed coincidences vs time during a phantom experiment with decaying ^{18}F and achieved with the block-pairwise method of DTC in the Siemens 3T MR BrainPET insert scanner.

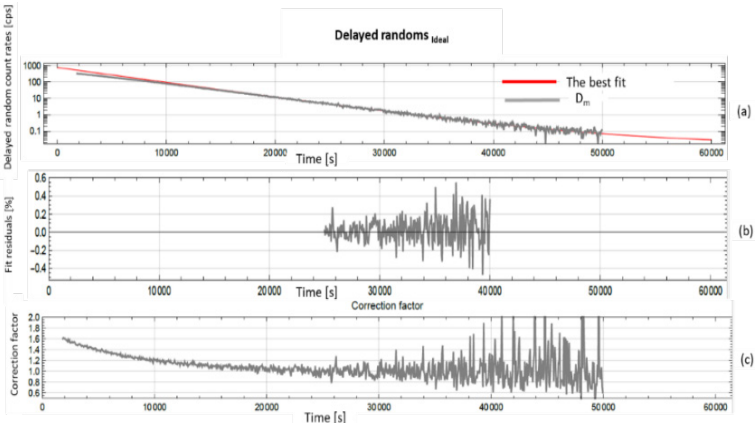

Figure 4.18 a: The extrapolated best fit (red line) together with the measured delayed random coincidences (gray line), b: Relative fit residuals for the data shown in a. c: The obtained DT correction factor with correction for triple coincidences, but without setting the factor to 1 for low counts.

Figure 4.19 “a” shows the DT correction factor with correction for triple coincidences, now after setting the DTC factor to 1 for low counts (happening approximately at second 25000) for a single block pair (same block pair and acquisition as figure 4.17-4.18). Figure 4.19 “b” is presenting both the corrected true coincidence count rates (green line) and the

measured true coincidence count rates for the same single block pair vs the time.

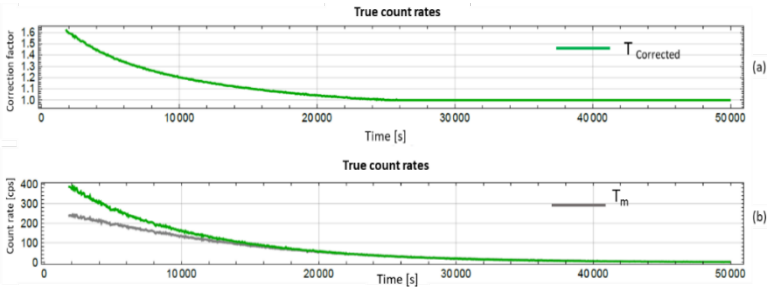

Figure 4.19 a: DT correction factor after setting the DTC factor to 1 for low counts, b: Both, the corrected true coincidence count rates (green line) and the measured true coincidence count rate (gray line) vs the time for the same block-pair.

4.3.3. The Complete Block-Pairwise Fit Model

Figure 4.20 “a” shows again the measured true coincidence count rates and the corrected true coincidence count rates for a single block pair vs acquisition time of the ^{18}F decay experimental. But now, the corrected true coincidence count rates are fitted with a single exponential decaying at the rate

of ^{18}F (red line). Figure 4.20 “b” is showing the corresponding fit residuals and figure 4.20 “c” is showing the relative fit residuals errors for the corresponding fit. The steps presented in figures 4.17 to 4.20 are done for all 10944 block-pairs individually. Figure 4.21 “a” shows the uncorrected and the corrected true count rates vs acquisition time of all the sum of all 10944 block-pairs together with the best fit using a simple exponential with offset term decaying at the rate of ^{18}F, while “b” is showing the fit residuals of the fit, and c shows the relative fit residuals for the same data, “c” is the best fit result obtained after correcting all individual block-pairs using the block-pairwise DTC method with triple overcount correction and assuming non- paralyzable characteristics.

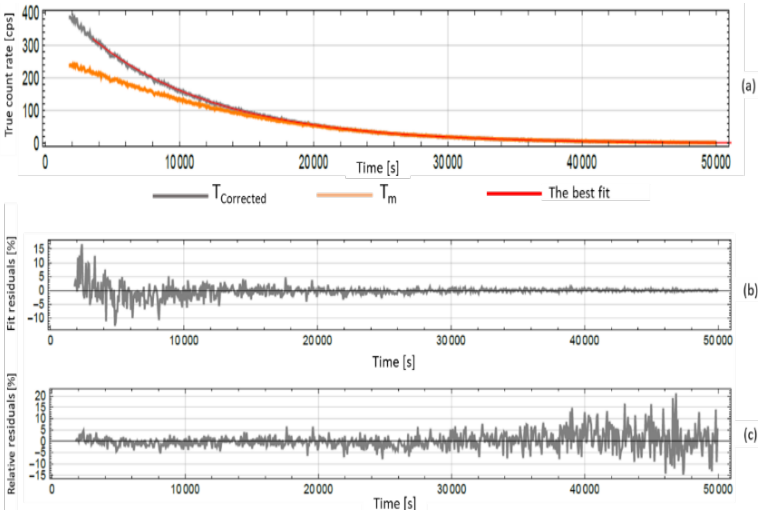

Figure 4.20 a: Measured true coincidence count rates (orange line) and corrected true coincidence count rates (gray line) for a single block pair vs acquisition time obtained with the ^{18}F decay experiment, adapted from Issa et al. 2022. The red line represents the best fit with a single exponential decaying at the rate of ^{18}F. b: Fit residuals for figure a. c: Relative fit residuals for the corresponding fit.

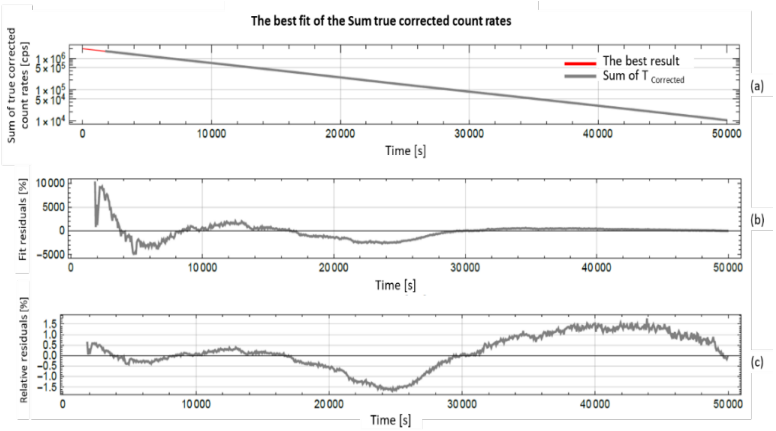

Figure 4.21 a: The best fit result using a single exponential with offset term decaying at the rate of ^{18}F (red line) of the sum of all block-pairwise corrected true count rates vs acquisition time for the ^{18}F decay experiment, b: Fit residuals for the fit shown in figure a, c: The relative residuals for the corresponding fit.

All figures 4.17 to 4.21 were generated using the individually obtained best fit parameters for each of the 10944 block-pairs and computing the DTC factor for each individual block-pair by using these best fit parameters together with equation 3.17.

Figures 4.22, 4.23, 4.24 and 4.25 show these fit parameters and their corresponding uncertainties.

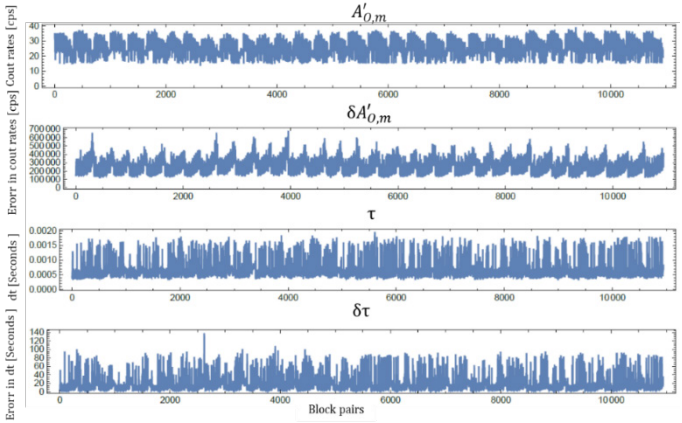

Figure 4.22 The best fit parameters $A'_{0,m}$ and τ together with the corresponding parameter uncertainties $\delta A'_{0,m}$ and $\delta\tau$ for the 10944 indivudual block pairs.

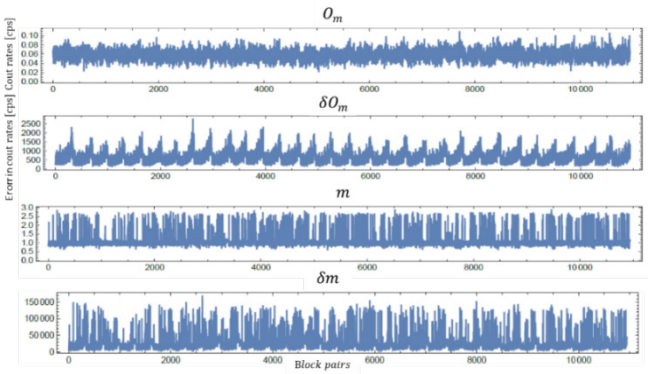

Figure 4.23 Best fit parameters O_m and m together with the corresponding parameter uncertainties δO_m and δm for the 10944 indivudual block pairs.

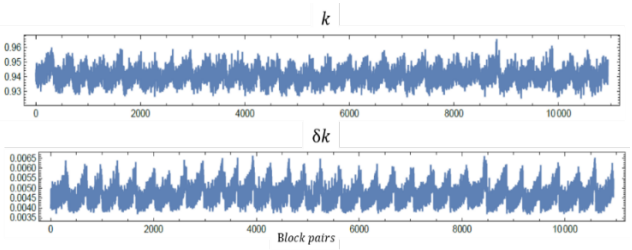

Figure 4.24 Best fit parameters k together with the corresponding parameter uncertainties δk for the 10944 indivudual block pairs.

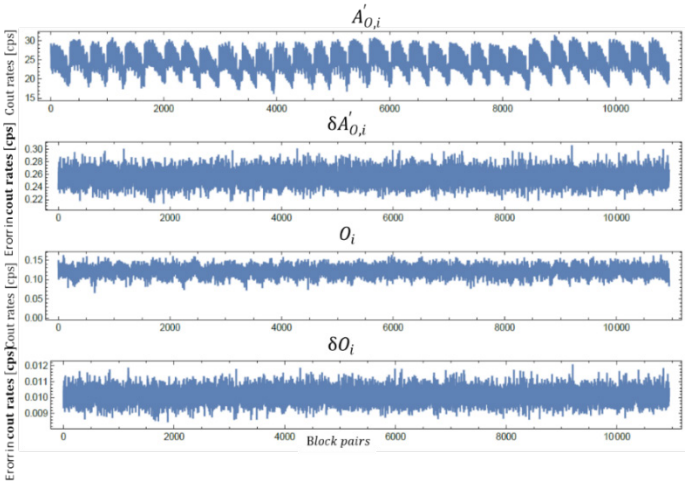

Figure 4.25 The best fit parameters $A'_{O,i}$ and O_i together with the corresponding parameter uncertainties $\delta A'_{O,i}$ and δO_i for the 10944 indivudual block pairs.

The corresponding uncertainties for each of the fit parameters expect $A'_{O,i}$ and O_i and k are larger than the best-fit parameters, which can be explained by the fact the fit model for the measured count rates is far more complex than the model for the ideal count rates. The parameters are not independent of each other which adds a high degree of freedom to the optimiztion problem, leading also to high uncertainty. The parameters $A'_{O,i}$, $A'_{O,m}$, O_m, and k

still present clear systematic variations over the 10944 block pairs, which means that there is still a small residual dependency on the block position for these paramters, which can be explained by the fact that the model most certainly does not exactly predict the measured count rates, although the found approximation is in very good agreement. Both m and τ show strong fluctuations, which again must be explained by the complexity of the model and the challenge for finding iteratively the absolute minimum of the sum of squares. However, as will be shown later, this has no noticeable influence on the final results.

The procedure of finding the DT corrected sum of all block-pairwise true coincidence count rates and fitting an exponential decay model with offset term but without DT losses to it was repeated for several different approaches. Relative fit residuals corresponding to figure 4.21 c for these for cases are shown in figure 4.26. In the first case, a non-paralyzable behavior is assumed and the individual sets of the obtained fit parameters are applied to

compute the block-pairwise DTC factor for each of the 10944 block pairs. In the second case, an average set of the fit parameters was computed from the individual parameter sets and these average values were applied to compute the block-pairwise DTC factor (assuming again non-paralyzing behavior). In the third case, we assume again a non-paralyzing behavior and apply individual parameter sets to compute the block-pairwise DTC factors but we omit triple correction. For the fourth case we were assuming paralyzing behavior, we applied individual parameter sets, and triple correction. All relative residuals were obtained by fitting a single exponential decaying at the rate of ^{18}F to the DT corrected global true count rate (Issa et al. 2022).

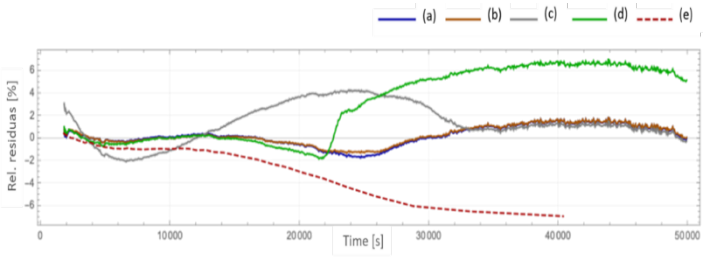

Figure 4.26 Relative fit residuals of the DT corrected and summed true coincidence count rates vs time obtained with a phantom experiment with decaying ^{18}F. Blue line (a): After applying block-pairwise DT correction assuming non-paralyzable behavior, individual fit parameter sets, and triple correction. Orange line (b): Assuming the non-paralyzable behavior, averaged fit parameter set, and triple correction, Gray line (c): Assuming the non-paralyzable behavior, individual fit parameter sets, and no triple correction, Green line (d): Assuming the paralyzable behavior, individual fit parameter sets, and triple correction. Dashed orange line (e): The corresponding residuals for the global DTC methods are shown tor comparison (adapted from Issa et al. 2022).

The best case with lowest relative residuals considering the entire count rate range was the second case (case b), where the relative residuals, i.e. the deviation from the ideal behavior, were

always larger than ≈ -1.2% and smaller than ≈ 1.6%. Without triple correction (case c), the maximum deviation from the expected counts was > -2% and < 4% and therefore substantially larger. However, nearly no differences between the first and second cases (a & b) and the second and fourth cases (b & d) were observed. Throughout the remaining part of this work, only DT correction to case b, i.e., assuming the non- paralyzable behavior, applying an averaged parameter set, and applying triple correction, will be used. Our results showed, that the triples correction leads to higher accuracy of the block-pairwise DTC method, as the average prompt count rate from a homogenous phantom, the maximum deviation between DTC measured trues and ideally expected trues was only 1.5 % in the worst case (with triple correction). While without triple correction, the corresponding maximum deviation between measured trues and expected trues was 4 %.

4.3.4 DTCf values with and without activity out of FOV

Figure 4.27 shows the DTC factors averaged over the first 200s of the acquisition for both measurements with decaying activity (with and without activity out of FOV) and summed over all blocks with the same axial position, thus showing the correction factor depending on the detector ring of the 3T MR BrainPET. These ring-wise average DT correction factors were obtained from phantom measurement with decaying ^{18}F inside the FOV (left figure), and with additional decaying activity outside of the FOV (right figure).

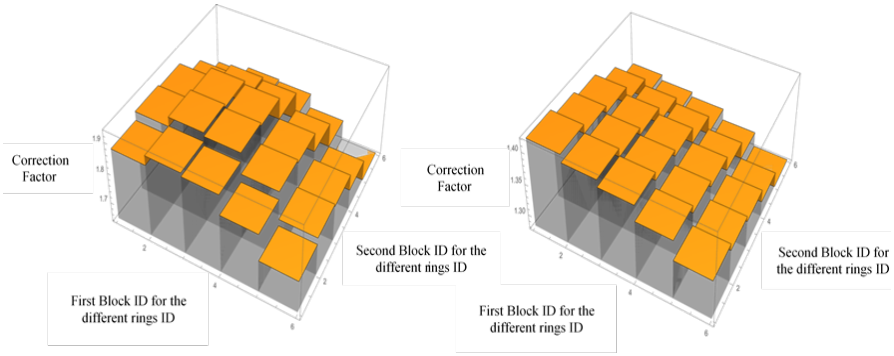

Figure 4.27 Left: The DTC factors for different blocks pairs according to their position in one of the six rings obtained with a phantom measurement inside of FOV and without any outside FOV activity. Right. The DTC factors for different blocks pairs according to their position in one of the six rings obtained with a phantom measurement inside of FOV and with noticeable outside FOV activity.

Figure 4.28 shows the DTC factors averaged over the first 200 seconds summed over all blocks within the same head, thus showing the correction factor depending on the position within the detector ring of the 3T MR BrainPET. Again, these average DT correction factors were obtained from phantom measurement with decaying ^{18}F inside the FOV (left

figure), and with additional decaying activity outside of the FOV (right figure).

According to the original work of the block-pairwise DTC method (Yamamoto et al. 1986), was mentioned that the method could have amplified the noise, in the case of the ring-wise range which they used, therefore we investigated the noise behavior. The derivative of the DTCf has a slope between 0.002 and 0.008 over the relevant range of measured delayed random coincidence count rates (see figure 4.29). Thus, the statistical noise of the measured delayed random count rates is propagating into the DTC factor with a magnitude which is reduced by a factor of more than100.

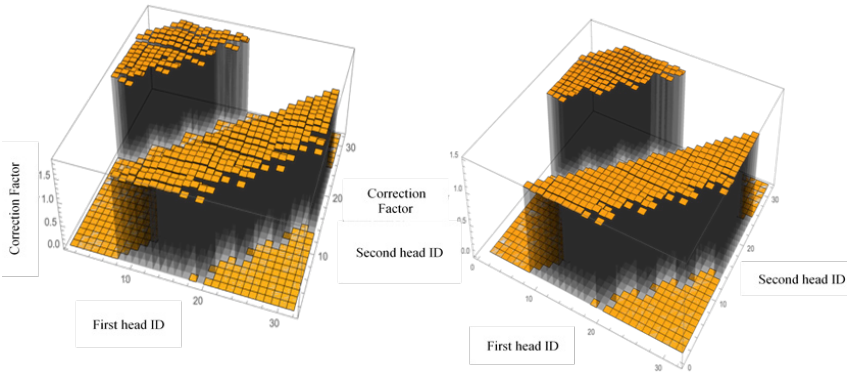

Figure 4.28 Left: The DTC factors for different blocks pairs according to their position in one of the 32 cassettes obtained with a phantom measurement inside of FOV and without any outside FOV activity. Right. The DTC factors for different blocks pairs according to their position in one of the 32 cassettes obtained with a phantom measurement inside of FOV and with noticeable outside FOV activity.

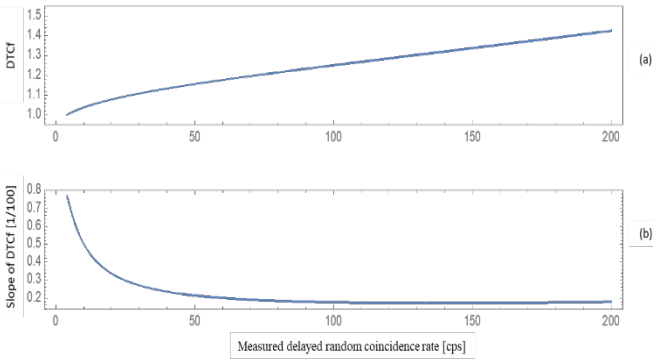

Figure 4.29 a: DTCf for averaged set of best fit parameters and typical delayed random count rates between 0 and 200 cps. b: Derivative of the DTCf with respect to the count rate of the same data (divided by 100 for better readability).

4.3.5 Impact of Single Scatter Simulation variations on image noise

An additional potential source of random variations propagating into the reconstructed images is the single scatter simulation (SSS) algorithm and its global scaling using methods as tail fit. Therefore, we analyzed the scatter sinograms obtained with different global scaling method in order to find the expected variations due to SSS combined with the block-pairwise DTC method and the global DTC

method. Figures 4.30 show the COV of the sum over all sinogram entries of an individual 2D sinogram slices for all 1399 sinogram slices obtained from an DT corrected ^{18}F decay experiment. To obtain figure 4.30 a, global DTC together with SSS scaling by tail fitting was used. To obtain figure 4.30 b, block-pairwise DTC together with SSS scaling by tail fitting was used.

The variations introduced by the SSS are comparable for all 4 cases and are at a level of ≈ 4%. The smallest variations between individual sinogram slices were observed for the block-pairwise DTC method combined with ML SSS scaling. The sinograms for this analysis were obtained from phantom measurements.

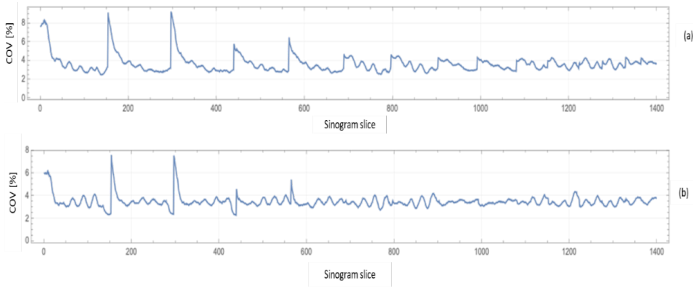

Figure 4.30 COV in the 1399 sinogram slices of the scatter sinogram when using tail fit for SSS scaling together with global DTC (a) and block-pairwise DTC (b).

4.3.6 Reconstructed Images of the Phantom Measurements

Figures 4.31 and 4.32 presents the mean of the activity concentration in Bq/cm^3 vs. time for the measurement with activity outside of FOV with the ^{18}F 3-compartment-phantom for relevant regions. The ROIs at the front and rear sides have been drawn guarding 1 cm (figure 4.31) and 2 cm (figure 4.32)

distance from the phantom walls. The images were reconstructed with using global DTC and block-pairwise DTC. For comparison, also the results from reconstruction without DTC are shown.

Figure 4.33. shows the COV vs. time for the measureemnt with ^{18}F the 3 compartment-phantom and out-of FOV activity for the same ROIs of figures 4.31and 4.32 The images were reconstructed with using global DTC and block-pairwise DTC. For comparison, also the results from reconstruction without DTC are shown.

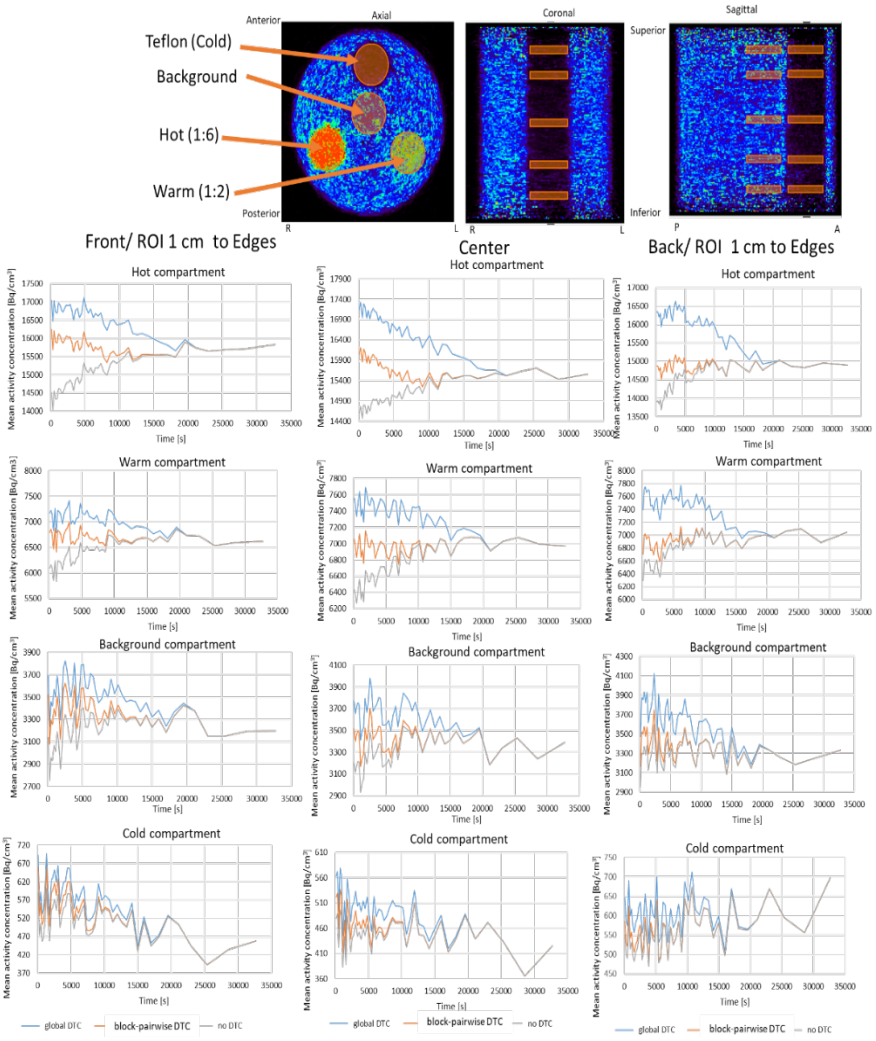

Figure 4. 31 Mean of the activity concentration in Bq/cm^3 vs. time for the three-compartment phantom filled with ^{18}F diluted in water for relevant regions and measured

with activity outside of FOV. The hot compartment on the right side was filled with 6 times higher activity concentration compared to the background, the warm compartment on the left side was filled with 2 times higher activity concentration compared, the background ROI sets in the center and it was filled with 113.3 MBq, and the cold compartment is made from solid Teflon. The ROIs at the front and rear sides have been drawn guarding 1 cm distance from the phantom walls, adapted from Issa et al. 2022.

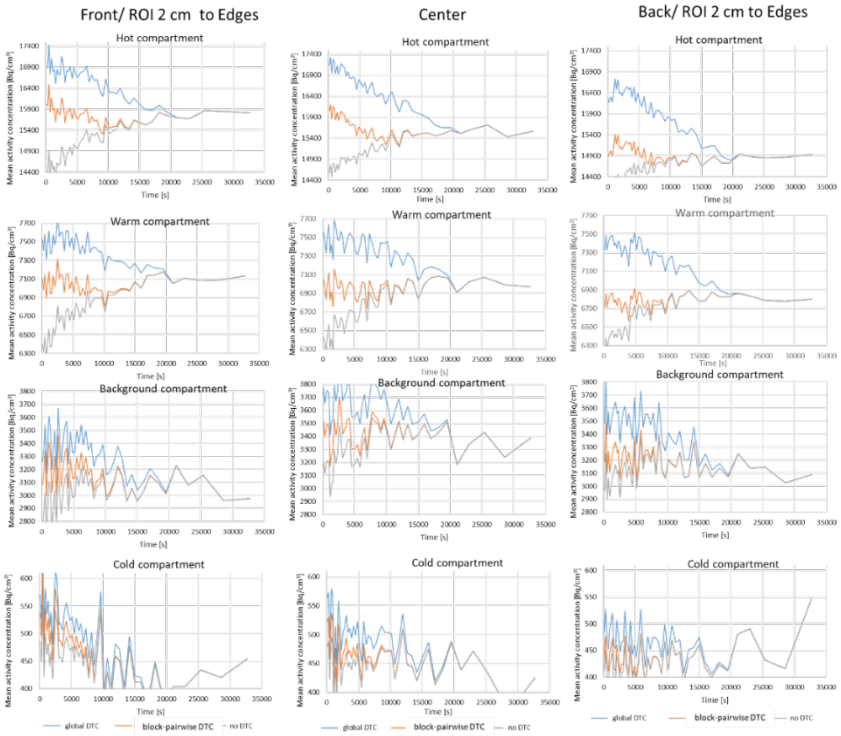

Figure 4.32 The mean of the activity concentration in Bq/cm^3 vs. time for the measurement with activity outside of FOV with ^{18}F the 3 compartment-phantom for relevant regions The ROIs at the front and rear sides have been drawn guarding 2 cm distance from the phantom walls, adapting from Issa et al. 2022.

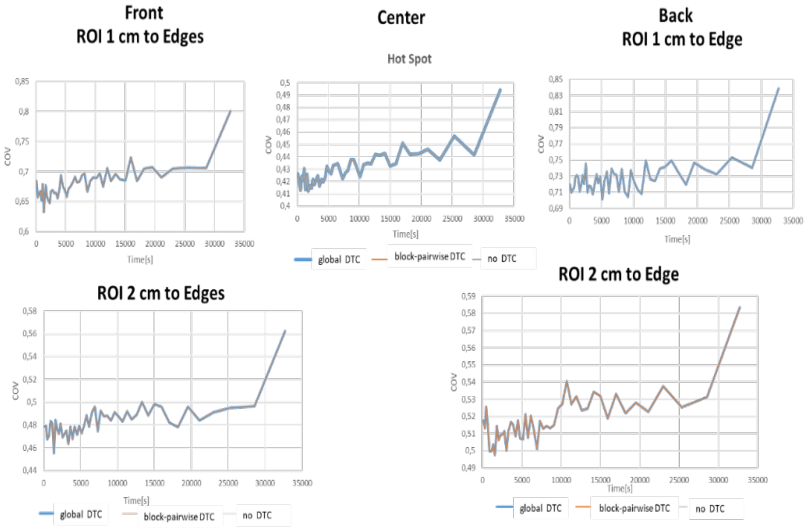

Figure 4.33 COV vs. time for the ^{18}F phantom measureemnt with the 3 compartment-phantom and out-of FOV activity for the same ROIs of figures 4.31 and 4.32, adating from Issa et al. 2022.

The largest differences between the global and the block-pairwise DTC methods were observed in the hot compartment. We can assume that dead time effects can be neglected for t > 20 000 seconds, since the measured activity concentrations with global and the block-pairwise DTC and without DTC converge

at this time. It can be seen, that the global DTC leads to an overestimation of ≈ 6 to 9 % in the three regions of the hot compartment, while the overestimation is reduced significantly when using the block-pairwise DTC (only 3% for the center ROI, and minimal in the front and rear ROI, respectively).

For the warm compartment, overestimations with global DTC reduce to ≈ 6 to 8 % in the three regions, while no overcorrection is observed with the local DTC correction. Overcorrections in the background compartment are of the same order, obtaining lower overcorrections with the block-pairwise method. For the cold compartment, both methods behave very similarly. The COV is the same for all three reconstructions as figure 4.33., i.e. with global DTC, with block-pairwise DTC, and without any DTC.

An evaluation of the noise propagation into the reconstructed image was done previously to the image evaluation and the variation (i.e. statistical noise) in the DTC factor of the block-pairwise DTC

method was found to be of the order of 10 times smaller than the expected count rate variations of the total prompt coincidences when estimating the correction factor for each second. Thus, no relevant noise propagation into the PET image should be observed, and the image noise is dominated by the statistical variations of the prompt count rates, which can be readily seen in figure 4.33 (the COV for all reconstructions is the same).

As the average activity concentration in the case of the global DTC method is consistently higher compared to the average activity concentration obtained with the block-pairwise DTC, especially in the case of high count rates, and also higher than the assumed ideal count rates with DT losses and without DTC correction (obtained by extrapolating the line without DTC correction from its asymptotic limit at low count rates, i.e. large times to its limit at high-count rates, i.e. large times). Thus it can be expected that the overcorrection of the global method also propagated into the calibration factor, requiring a new PET system calibration for the

block-pairwise DTC method, or a cross-calibration of the block-pairwise DTC method against the global DTC method. We preferred a cross-calibration with a dedicated phantom measurement and obtained a cross-calibration factor of 1.079, which was applied for all images obtained with the block-pairwise method.

The calibration bias results are summarized in the table 4.2 below for both of the global and the block-pairwise DTC methods. The relative differences of the calibration factors obtained in the four ROIs (three short cylindrical ROIs and one long cylindrical ROI) were computed for both cases where activity was and was not present outside the FOV.

Table 4.2 The relative differences when comparing calibration factors with and without out of FOV activity for relevant ROIs using global DTC and block-pairwise DTC. Adapted from Issa et al. 2022

DTC method	Cylindrical ROI Front side of phantom	Cylindrical ROI Center of phantom	Cylindrical ROI Back side of phantom	Cylindrical ROI Full calibration region
global DTC	-4.32%	-1.50%	0.56%	-1.5%
block-pairwise DTC	-2.10%	-1.90%	-0.79%	-1.44%

4.3.7 Impact of the two DTC Methods on quantitative measurements

From the phantom measurements it could be seen, that there was a better agreement between the ground truth (ideal behavior without DT losses) and the corrected images when using the block-pairwise DTC. Consequently, the block-pairwise DTC will lead to reconstructed TACs of patient and volunteer measurements, which present less bias. Figure 4.34 compares the time course of the DTC factors for the

block-pair with highest and lowest DTC, the average block-pairwise DTCf, and the global DTC for a typical volunteer measurement with the neuroreceptor ligand [^{11}C]ABP688 (Régio Brambilla et al. 2020).

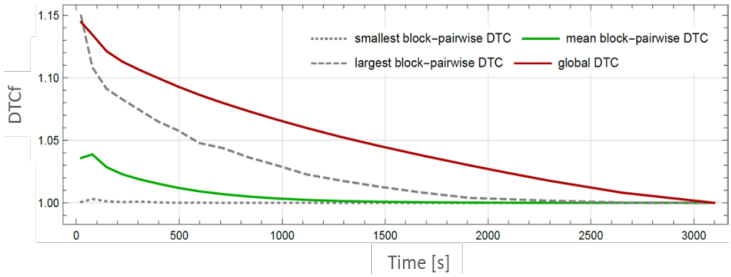

Figure 4.34 DTC factors against acquisition time for the global DTC method compared to selected DTCfs of the block-pairwise DTC method obtained from a typical [^{11}C]ABP688 volunteer measurement of a schizophrenia study, adapted from Issa et al. 2023.

Figure 4.34 shows, that the global DTC method has led to a significantly higher DTC factor when compared to the block-pairwise DTC method. Thus, the global DTC method results in an overestimation of the activity concentration not only in the reconstructed images obtained from phantom measurements but also in the reconstructed images obtained from volunteer or patient measurements.

I. Validation of the block-pairwise method with [^{11}C]ABP688 PET acquisitions

The validation of the block-pairwise DTC with patient and volunteer measurements and its comparison to the global dead time correction using [^{11}C]ABP688 showed important differences in the TACs and derived quantitative estimators such as V_T and BP_{ND}. The evaluation of the [^{11}C]ABP688 measurements showed, that the TACs obtained with the different DTC methods show clear differences in all three regions and that this difference varies over the scanning time. However, as expected, the

differences became smaller towards the end of the scan and after a steady state is reached between 25-35 min. Nevertheless, even a small difference in the TACs can lead to a relevant lack of accuracy of quantitative parameters obtained from the PET images (Issa et al. 2022). Figure 4.35 shows the TACs obtained with [^{11}C]ABP688 in three VOIs using global and block-pairwise DTC methods during image reconstruction, and after applying the cross-calibration factor to the reconstruction with block-pairwise DTC method.

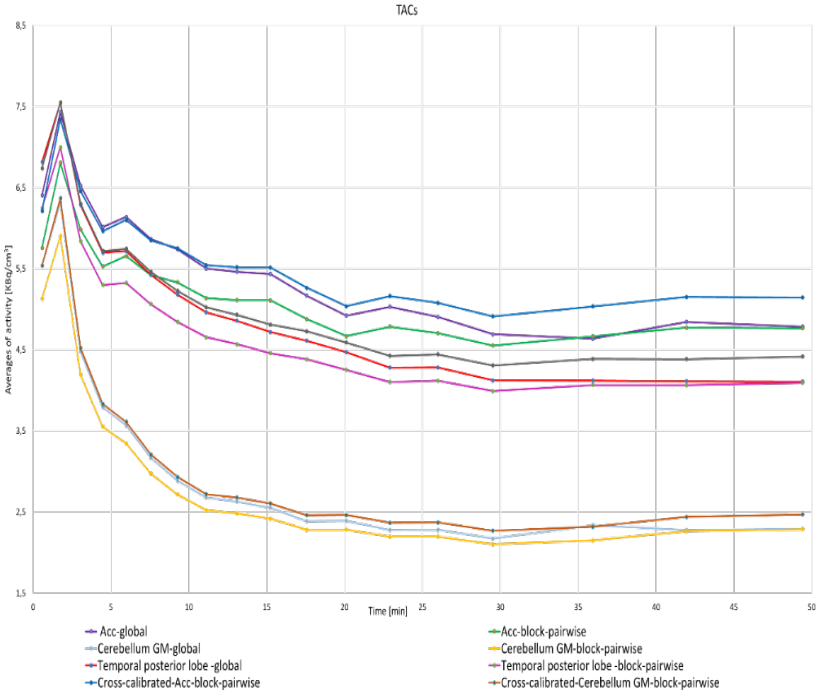

Figure 4.35 The [^{11}C]ABP688 TACs of a smoker in three relevant regions of the human brain and for both DTC methods: Cerebellum, Temporal posterior lobe and the ACC, for global DTC and block-pairwise DTC methods and after applying the cross-calibration factor to the reconstruction with the block-pairwise DTC method.

Figure 4.36 shows for each of the global and the block-pairwise DTC methods the distribution box-plots of the slope values of the BP_{ND} obtained by the simple ratio method in two exemplary brain regions and after reaching the equilibrium. For the BP_{ND} in the ACC, the statistical distribution of the slopes of the BP_{ND} was -0.0025 min^{-1} for the global DTC method, while it was around -0.003 min^{-1} for the block-pairwise DTC method. The median for the global DTC was -0.002 min^{-1} and for the block-pairwise DTC was -0.0032 min^{-1}. For the temporal posterior lobes, the statistical distribution of the slopes of the BP_{ND} was -0.0029 min^{-1} for the global DTC method while it was around the same -0.00292 for the block-pairwise DTC method. The median for the global DTC was -0.0039 min^{-1} and for the block-pairwise DTC was -0.0034 min^{-1}. The BP_{ND} has not shown a real difference between both DTC methods.

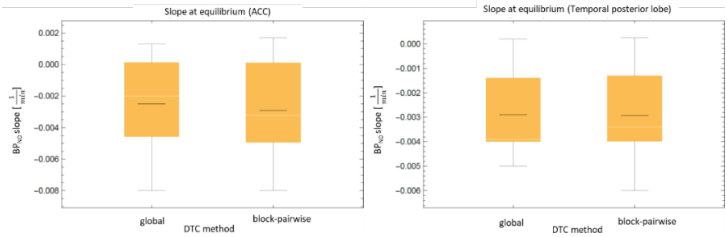

Figure 4.36 The statistical distribution of the slope values for BP_{ND} and global DTC and block-pairwise methods for three exemplary brain regions obtained with the Siemens 3T MR BrainPET insert scanner. Black line: mean, white line: median, yellow box 25/75% quantile, fences: min/max values, adapted from Issa et al. 2023.

Figure 4.37 shows the mean relative differences of the TAC ratios between global and the block-pairwise DTC methods in the ACC and cerebellum gray matter. The ACC-relative-difference and the cerebellum-relative-difference approach at the end of the recording time (3000 seconds). As the true counts framing scheme was used, the reconstructed

image frames were shortened to less than 0.5 lengths to the midpoint. However, in the beginning, when the injection is administered as a bolus with high radioactivity, these relative differences are 9.2 % and 6.5 %, respectively, i.e., they differ by a factor of 1.4. In the end, this factor decreases to 1.1. The average difference for the entire scan time is 1.28.

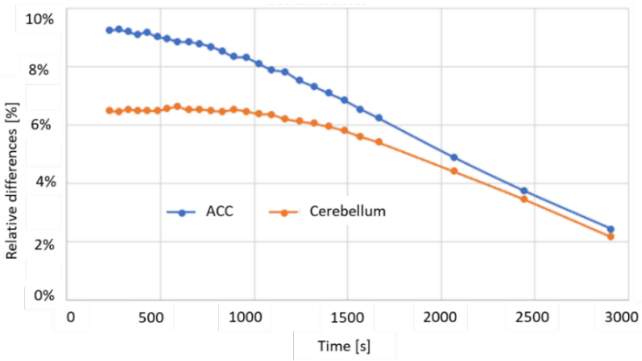

Figure 4.37 The mean relative differences of the TAC ratios between global and the block-pairwise DTC methods in the ACC and cerebellum gray matter.

Figure 4.38 presents the distributions of the slope values of the V_T in three exemplary brain regions

and after reaching the equilibrium for the global and block-pairwise DTC methods. In the ACC region, the statistical distribution of the slopes in the V_T curves was around -0.00038 ml/(cm^3 x min) to the zero value (equilibrium) in the global DTC method, while for the block-pairwise method it was 0.0015 ml/(cm^3 x min) to the zero. The median was for the global DTC -0. 0022 ml/(cm^3 x min), and for the block-pairwise DTC was 0. 0022 ml/(cm^3 x min). For the temporal posterior lobes, the statistical distribution of the slopes in the V_T curves was around -0.0051 ml/(cm^3 x min) using the global DTC, while it was 0.00014 ml/(cm^3 x min) using the block-pairwise DTC method. The median for the global DTC was -0.0028 ml/(cm^3 x min) and for the block-pairwise DTC the ideal slope value at equilibrium, i.e. zero, was reached. This shows that there is an important difference in the computed V_T for both DTC methods, where it was shown with phantom measurements, that the global method introduces a noticeable bias. Therefore, it can be assumed, that the global DTC method introduces a bias in the V_T and that the block-pairwise method is

more accurate. In the cerebellum GM (reference region), the statistical distribution of the slopes in the V_T curves was around -0.00033 ml/(cm^3 x min) to the zero value in the global DTC method, while it was around 0.0031 ml/(cm^3 x min) in the block-pairwise DTC method. The median for the global DTC was -0.0002 ml/(cm^3 x min) and for the block-pairwise DTC it was 0.0028 ml/(cm^3 x min). The mean the statistical distribution of the V_T slopes in the global data is better than in the block-pairwise for the reference area. It was found, that a relevant bias in V_T is introduced by the global DTC method used with the Siemens 3T MR BrainPET insert scanner for the studied brain regions. The bias was considerably smaller for BP_{ND}, which in this work was computed using the simple ratio method, because in this case, the DTC caused bias cancels.

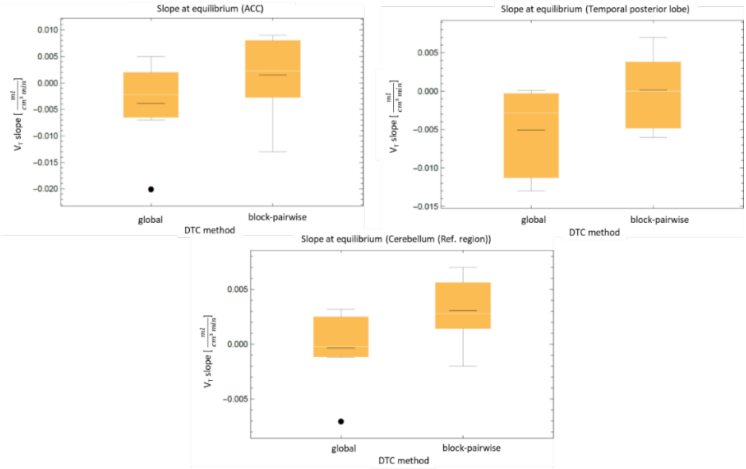

Figure 4.38 The statistical distribution of the slope values for V_T and global and block-pairwise DTC methods for three exemplary brain regions obtained with the Siemens 3T MR BrainPET insert scanner. Black line: mean, white line: median, yellow box 25/75% quantile, fences: min/max values, black dots: outlier. Adapted from Issa et al. 2023.

II. Validation of the block-pairwise method with [^{18}F]-FET- PET acquisitions

The validation of the block-pairwise DTC with patient and volunteer measurements and its comparison to the global dead time correction using [^{18}F]-FET-PET showed important differences in the TACs and derived quantities such as TBR_{max} and TBR_{mean}. Figure 4.39 presents the TACs obtained from one [^{18}F]-FET-PET acquisition for three relevant types of VOIs for the global and the block-pairwise DTC methods. For the block-pairwise DTC method, we showed the TACs before and after application of the cross-calibration factor.

The results we obtained after applying the cross-calibration factor to the block-pairwise DTC data show that in the background and tumor regions, the block-pairwise method leads to equal values as the global DTC (overlaps with TAC obtained with global DTC). In contrast, we observed overcorrection in the tumor-max region for the global DTC method compared to the block-pairwise

even after application of the cross-calibration factor. For the [^{18}F]-FET-PET examinations, the global DTC method tends to overcorrect when compared to the block-pairwise DTC method in approximately 12% of the studied [^{18}F]-FET-PET cases and even after applying the cross-calibration factor. The overcorrection is considerable in the case of the Tumor-max VOI. Figure 4.39 below shows an example of [^{18}F]-FET-PET case that shows the global DTC overcorrection behavior (see Tumor-max VOI).

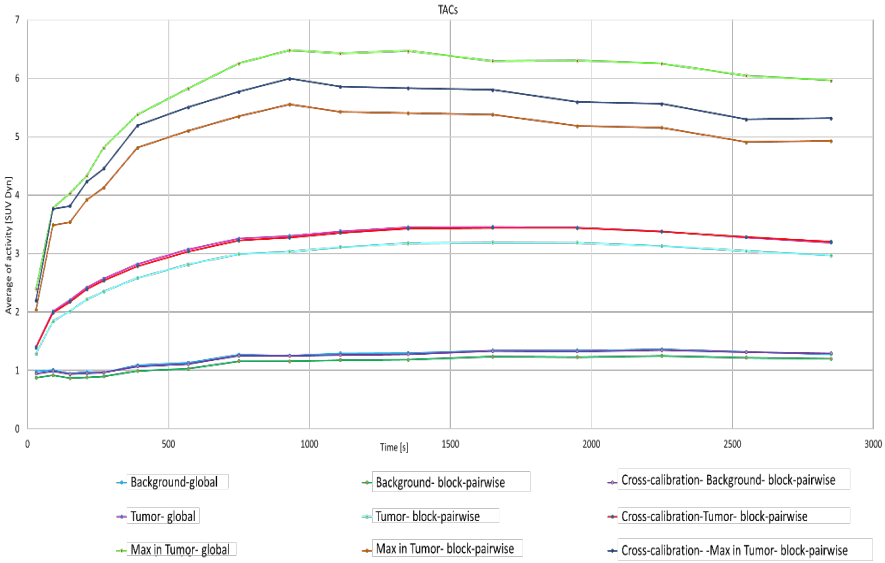

Figure 4.39 The TACs obtained from one [^{18}F]-FET-PET acquisition for three relevant types of VOIs for the global and the block-pairwise DTC methods. For the block-pairwise DTC method, we showed the TACs before and after application of the cross-calibration factor.

Figure 4.40 shows the statistical distribution of the curve shape parameter obtained from various [^{18}F]-FET TACs and for the global and block-pairwise DTC methods. The curve shape parameter casts the different behaviors of the [^{18}F]-FET TACs, i.e.

rising, plateau and falling after reaching a peak, into a single shape parameter κ (Lerche et al. 2021). It has been shown in previous studies, that the [^{18}F]-FET TAC shape is linked to the tumor grade (Kunz et al. 2019; Rausch et al. 2019; Fuenfgeld et al. 2020). The chosen VOIs for the [^{18}F]-FET images are the background (healthy control tissue), the tumor volume, the maximum concentration of the tracer in the tumor area, and the therapy target area.

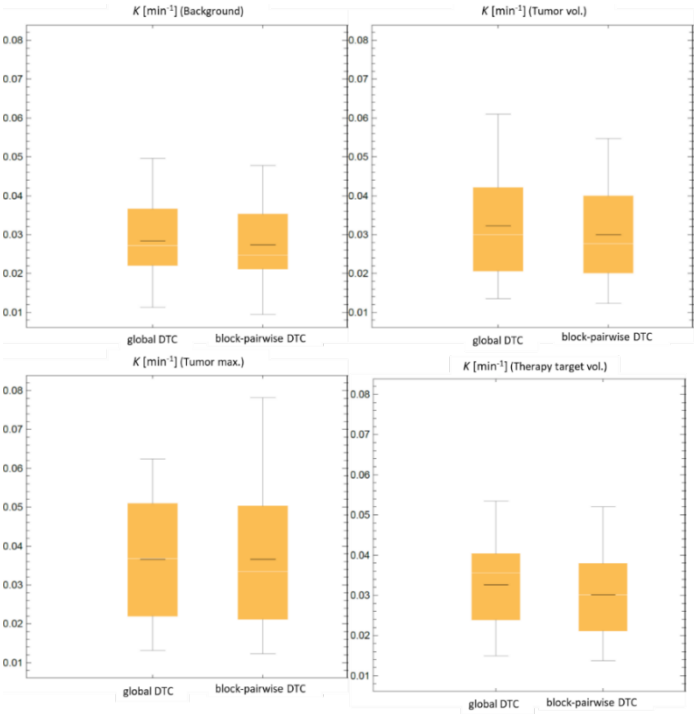

Figure 4.40 The curve-shape parameter statistics for the FET-PET TACs and global and block-pairwise DTC methods for four types of VOIs (i.e., therapy target, entire tumor volume, maximum value volume and healthy background volume). Black line: mean, white line: median, yellow box 25/75% quantile, fences: min/max values.

Figure 4.41 shows the statistics of relevant features of the [^{18}F]-FET-PET TBR_{max} and TBR_{mean} for the global DTC method and the block-pairwise DTC method.

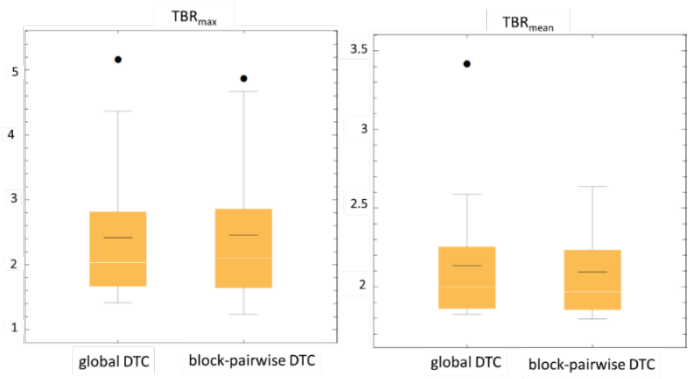

Figure 4.41 Statistics of relevant features of the [^{18}F]-FET-PET TBR_{max} and TBR_{mean} for the global DTC method and the block-pairwise DTC method in the Siemens 3T MR BrainPET insert scanner. Black line: mean, white line: median, yellow box 25/75% quantile, fences: min/max values, adapted from Issa et al. 2023.

Figure 4.42 shows how mean relative difference between the global and the block-pairwise DTC methods in the time interval 20 to 40 min p.i. for the TBR_{max} and TBR_{mean} values depend on the tumor size and the distance of the tumor to the PET FOV isocenter. It can be observed from these plots, that the observed differences between global and block-

pairwise DTC methods are strongly case-dependent for both, TBR_{max} and TBR_{mean} and that they can be rather large for specific cases. These differences are also time-dependent in some cases, see figure A.1 and A.2 in the appendix. The differences ratio of the twenty cases was around 4.4% in the TBR_{max} and TBR_{mean} between the global and the block-pairwise DTC methods. The difference in TBR_{max} shows a significant dependency on the distance of the tumor from the isocenter at 0.05 significance level and there seems to be a tendency that difference in TBR_{max} also depends on the tumor size. The latter difference is, however, not significant. No dependency on tumor size and tumor distance to the isocenter was observed for the that difference in TBR_{mean}. Table 4.3 The spearman rank test results for the dependencies of the TBR_{max} TBR_{mean} differences are resumed.

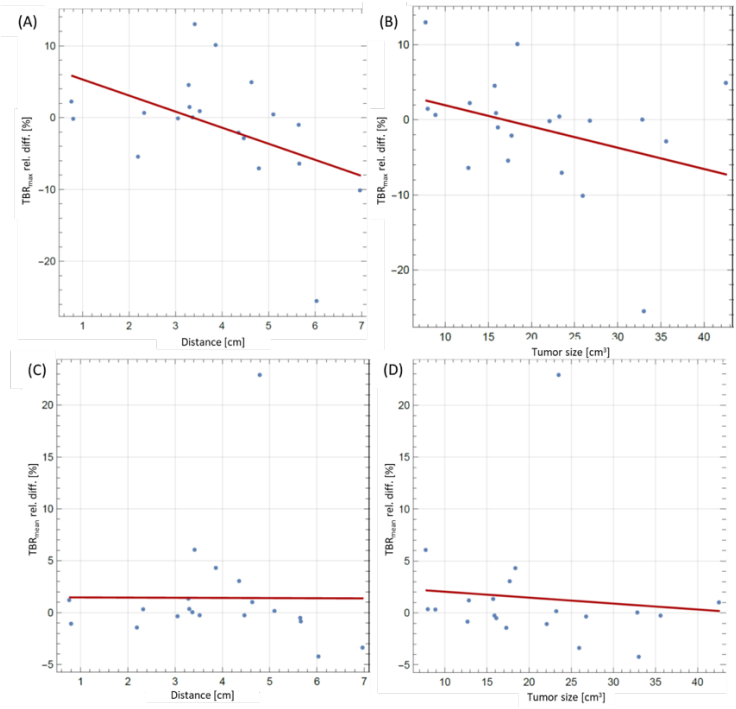

Figure 4.42 (A): Dependency of mean relative difference between the global and block-pairwise DTC methods in the time interval 20 to 40 min p.i. for the TBR_{max} on the distance of the tumor to the PET FOV isocenter. (B): Dependency of mean relative difference between the global and block-pairwise DTC methods in the time interval 20 to 40 min p.i. for the TBR_{max} on the tumor

size. (C): Dependency of mean relative difference between both DTC methods in the time interval 20 to 40 min p.i. for the TBR_{mean} on the distance of the tumor to the PET FOV isocenter. (D): Dependency of mean relative difference between both DTC methods in the time interval 20 to 40 min p.i. for the TBR_{mean} on the tumor size. Regression lines are shown in red, adapted from Issa et al. 2023.

Table 4.3 Spearman rank results for testing the correlation of differences in TBR_{mean} and TBR_{max} and tumor size and distance (data shown in fig. 4.42). Adapted from Issa et al. 2023.

TBR_{mean} vs distance			TBR_{mean} vs size		
	Statistic	P-Value		Statistic	P-Value
Spearman Rank	-0.2	0.4	Spearman Rank	-0.29	0.21
TBR_{max} vs distance			TBR_{max} vs size		
	Statistic	P-Value		Statistic	P-Value
Spearman Rank	-0.47	0.037	Spearman Rank	-0.39	0.09

III. Validation of the block-pairwise method with [^{15}O]H_2O acquisitions

The validation of the block-pairwise DTC with patient and volunteer measurements and its comparison to the global dead time correction using [^{15}O]H_2O acquisitions showed important differences in the TACs and the derived kinetic parameters such as rCBF, K_1, k_2, and V_T. Figure 4.43 presents the TACs obtained from one [^{15}O]H_2O measurement for relevant types of VOIs (GM and WM) for the global and the block-pairwise DTC methods. The overcorrecting behavior of the global DTC method compared to the block-pairwise DTC results of the GM and WM can be well observed.

Table 4.4 summarizes further statistical descriptors of the relative differences of the 4 kinetic parameters when comparing global and block-pairwise DTC methods. We observed a small but noticeable bias in all 4 parameters rCBF, K_1, k_2, and V_T for both regions. As the kinetic parameters obtained with the

global DTC method were considered as reference when computing the relative differences, a negative difference corresponds to the case that the parameter obtained width global DTC was smaller than the corresponding parameter obtained with block-pairwise DTC. Thus, except for V_T in WM, values obtained with global DTC method are always smaller by a few per cent. Plots of the statistical distributions of the relative differences are shown in figure 4.44. The GM/WM ratios are close to 2.5 for both DTC methods.

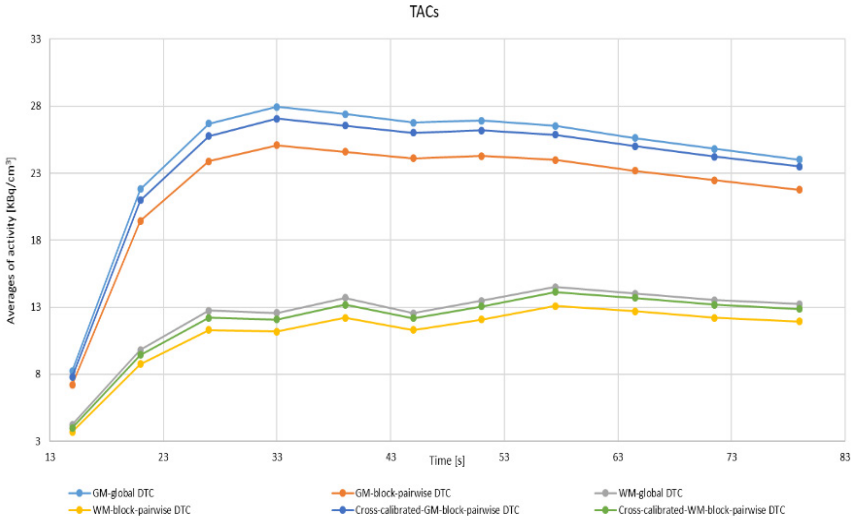

Figure 4.43 TACs of the [^{15}O]H_2O measurements for relevant types of VOIs for the global and the block-pairwise DTC methods.

Table 4.4 Main statistical descriptors of the relative differences between global and block-pairwise DTC for relevant kinetic parameters in GM and WM determined with [^{15}O]H_2O measurements. Adapted from Issa et al. 2023.

Relative differences of global and block-pairwise DTC methods in GM [%]							
Parameter	Mean	Median	StdDev	Min	Max	SE [%]	rel. change of SE
rCBF	-3.9	-3.71	1.82	-9.39	-0.21	2.42	0.97
K_1	-4.58	-3.73	4.6	-17.72	3.93	3.74	0.96
k_2	-3.24	-3.15	7.52	-22.98	13.15	6.32	0.94
V_T	-1.16	-1.27	3.23	-8.13	6.74	3.87	1.1
Relative differences of global and block-pairwise DTC methods in WM [%]							
Parameter	Mean	Median	StdDev	Min	Max	SE [%]	rel. change of SE
rCBF	-5.39	-3.95	4.38	-19.52	-2.84	4.13	1.03
K_1	-4.94	-5.08	1.56	-7.27	-1.35	3.12	0.93
k_2	-7	-7.05	4.84	-17.63	3.91	11.4	1.04
V_T	3.83	1.74	4.73	-5.09	13.25	8.89	1.08
GM: Gray Matter. WM: White matter. SE: Standard Error							

The evaluation of [^{15}O]H_2O (results of table 4.4) showed that a relevant difference was found in the

Gary matter (GM) region and it ranged from +4 % to -7 %. Average biases of -3.9 %, -4.58 %, -3.2%, and -1.2 % for the regional cerebral blood flow (rCBF), the rate constants K_1, k_2 and V_T were observed, respectively. Conversely, in the white matter region (WM), average biases of -5.4%, -4.9%, - 7.0%, and 3.8% were observed for rCBF, K_1, k_2, and V_T, respectively.

Figure 4.45 shows the rCBF comparison for reconstructions with block-pairwise and global DTC methods for the GM and WM. The rCBF results for the block-pairwise DTC method in both of GM and WM are higher than for the global DTC method. For GM, the median blood flow was 60 $\frac{\frac{ml}{min}}{100} ml$ with the block-pairwise DTC method while it was around of 57 $\frac{\frac{ml}{min}}{100} ml$ with the global DTC method the median. For the WM the median blood flow was around 26 $\frac{\frac{ml}{min}}{100} ml$ with the block-pairwise DTC method while it was 24 $\frac{\frac{ml}{min}}{100} m$ wiht global DTC method.

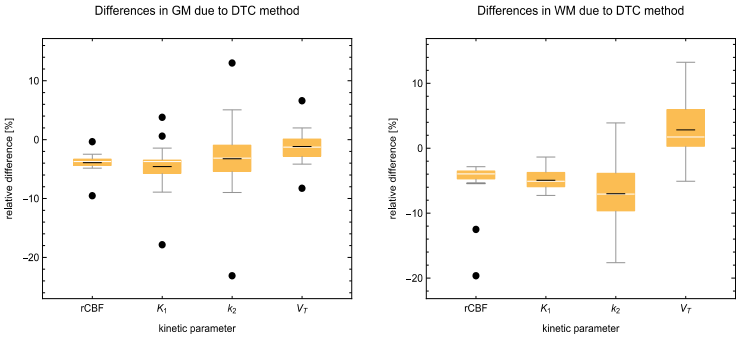

Figure 4.44 The statistical distribution of the relative differences for the kinetic parameters rCBF, K_1, k_2, and the V_T obtained from kinetic modelling of the [^{15}O]H_2O TACs assuming a one tissue compartment model. Black line: mean, white line: median, yellow box 25/75% quantile, fences: min/max values, black dots: outlier. Left: GM, right: WM. Adapted from Issa et al. 2023.

For the GM, the mean blood flow was 57 $\frac{\frac{ml}{min}}{100} ml$ with the block-pairwise DTC method while it was around of 55 $\frac{\frac{ml}{min}}{100} ml$ with global DTC method. No differences in mean values were observed for the WM. Figure 4.46 presents the comparison of the

rCBF GM to WM ratios for the block-pairwise and the global DTC methods. We found that the median of the rCBF GM/WM ratio was around 2.5 for both DTC methods. Table 4.5 shows the rCBF GM/WM ratios of the [^{15}O]H_2O measurements (data shown in figure 4.55).

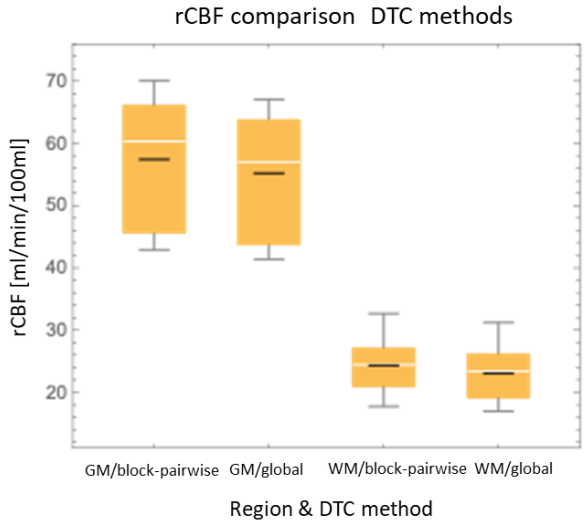

Figure 4.45 rCBF comparison of the block-pairwise and global DTC methods for the GM and WM regions. Black line: mean, white line: median, yellow box 25/75% quantile, fences: min/max values.

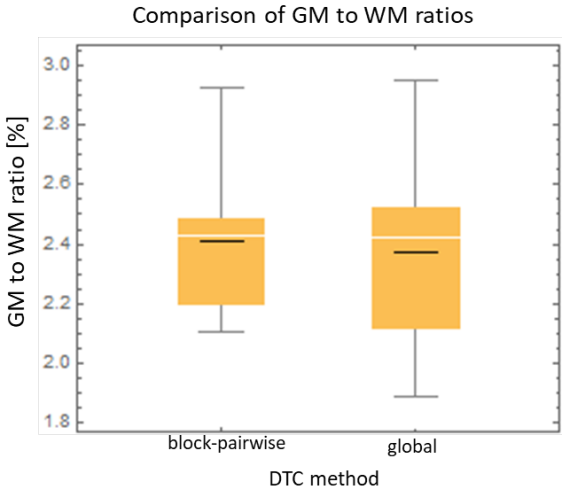

Figure 4.46 Comparison of rCBF GM to WM ratios for the block-pairwise and the global DTC methods. Black line: mean, white line: median, yellow box 25/75% quantile, fences: min/max values.

Table 4.5 The relative differences of the GM/WM ratios for the two DTC methods.

Parameter	Mean	Median	StdDev	Min	Max
rCBF	1.05	1	0.1	0.94	1.33

The global DTC method introduced a bias and overestimation in the studied quantitative parameters for all applications. In contrast, the results of the block-pairwise method show an improvement and a reduction in the bias in the evaluated quantitative parameters. The block-pairwise DTC method can be implemented in all systems that use the delayed window technique and is particularly expected to improve the quantitation accuracy of dedicated brain PET scanners due to their geometry.

5. Discussion

5.1 Comparison of Global DTC Method and Block-wise DTC Method

In this part of the work, we have studied the difference between the current (global) DTC and the block-wise DTC method. This thorough evaluation showed the limitations of the block-wise DTC method and lead to our decision not to use this method as future dead time correction for the dedicated Siemens 3T MR BrainPET insert. However, the block-wise DTC method was studied, since all block count rates are independent form all other blocks and since they are common for all scintillation events on the same block and the subsequent analog signal processing system of the detector on block level (figures. 1.14, 3.3, 4.1, and 4.3). By contrast, the global DTC method, which is currently used for the BrainPET insert and which was developed by Christoph Weirich (Weirich et al. 2013; Weirich et al. 2012), applies the same DTCf to all

detector blocks, even in cases when the individual blocks show highly different count rates, which is caused by the different physical position of each block (figure 4.4). This variation of the single-count rates for individual block leads necessarily to variations in the DT for the same blocks, while the block-wise DTC method has shown more consistent results in comparison to the global DTC method when studying non-validated singles. As expected for these geometrical consideration and actually shown later with the block-pairwise DTC method, the global DTC method leads to results with elevated bias and therefore less accuracy and a bias introduced by the DTC method inevitably propagates into the reconstructed images in the same way statistical noise does. For the above mentioned geometrical and system-architectural reasons, the development and study of improved DTC method was started with evaluating the block-wise DTC method. As we have shown (see figure 4.7, and figure 4.8), the block-wise DTC model can be used to describe the DT losses and

to correct these DT losses on the scintillation block level. The results show, that the block-wise DTC method has a sufficient precision to correct DT losses on the block level, i.e. for non-validated singles. However, it revealed to be insufficient to accurately correct the DT losses of prompt coincidences on block level. This is most probably caused by the fact, that the block-wise DTC is based on estimating the DT using the CFD counters (unqualified singles), which are not a good estimate for the number of accepted coincidences on any level, since energy thresholds are applied to unqualified singles during coincidence processing. The energy discrimination will lead to additional count rate losses not present in the unqualified singles. Therefore, considering coincidence losses on the block level is necessary to improve the DTC to account for all DT losses introduced by the data preprocessing chain. The presented block-pairwise DTC method fulfils this requirement and therefore lead to a relevant improvement of the DTC. Nevertheless, the work on the block-

wise DTC method offered us many important results, which we have taken into account for the further DTC improvement, i.e. the bock-pairwise DTC method. The experimental phantom measurements for evaluating the block-wise DTC method revealed that the block-wise unqualified singles follow the non-paralyzable DT model, and that all 192 individual detector blocks had a very similar dead time constant of ≈ 200 ns. Consequently, differences in the DT losses at block level can be expected to be highly dominated by the differences in the count rates at the block level, but not by differences (e.g. production tolerances) of the system components and their individual performance parameters as the DT constant which is approximately the same for all blocks. Thus, for an effective DTC method, only the differences in the coincidence count rates for each block, which depend on the geometrical physical position has to be taken into consideration. This holds especially in the case of imaging with the BrainPET insert ant its high effect of the activity and scatter radiation from

outside of the FOV. The ^{176}Lu background should be taken into consideration also to achieve sufficient DTC accuracy. Weirich et al. (2013) showed that DT losses are not a globally homogeneous effect and that they are dependent on the physical position of each block. The results observed by Weirich (Weirich et al. 2013) showed that the DTC has to be treated on block level and that it needs to be combined with an effective pileup correction on the crystal level. I could show in this work, that the DTC on block level using the paralyzabel model with unqualified is highly accurate since the DT is common for all scintillation pixel on each individual block in the way that the DT losses are depending on the count rates of the entire individual block. As we described in (3.1.2 session, block-wise DTC method), the DT is the same for all events detected by any crystal on the same block due to the scintillation detector and acquisition system design, i.e. any event detected on the block will makes it insensitive for approximately 200 ns, where this DT constant is

nearly the same for all 192 blocks. The differences in the DT losses of a crystal on a block are thus depending only on the count rate of this individual block which itself depends on the geometrical location of that block and the distribution of the activity inside and outside of the FOV.

The reason that we don't apply the DTC on the crystal level is that the DT is the same for all. If one pixel scintillates, the entire block is busy. So there is no reason to go to the pixel level. Further, we inherently consider a pile-up, as the energy filter is applied to the delayed randoms too. The Pileup means gammas photons are detected at the same time in the same block, thus the detected energy is outside the filter. For global DTC works the inclusion of Pile-up was relevant, as it is not accurately handled with the CFD counts, the CFD counts were used to estimate the DT losses while the block-pairwise DTC method uses the delayed to estimate the CFD counts, where pile-up events are correctly treated. On the

crystal level, we found that the effect of the scatter correction will be more significant than DTC, as the crystals suffer from the scatter radiation inside each block (inter-crystal scatter) and from outside the block level. This is related to the energy window in the dedicated Siemens 3T MR BrainPET insert scanner which is modeled by the non-validated singles. The scatter fraction ranges in the brain scanning is more than 30%-35%, with the other variables such as the energy window settings and the scanner geometry (Zaidi & Montandon 2007; Álvarez-Gómez et al. 2021).

Apart from the present work, only few systematic studies on improvements of DT accuracy and precision have been published in recent years. Aykac et al. (2017) described a DTC method and pile-up correction on crystal pixel level. The method was implemented as a part of the normalization of the prototype of a SiPM based PET scanner and it is based on the crystal count rates estimated from the random sinogram and a

coincidences response in the electronics. This method may be of interest for the new BrainPET 7T prototype, as it offered a simplified method DTC for the crystal level instead of the block detector level, since the scintillation block works differently; in the new BrainPET the entire block will not be paralyzed, only a few SiPMs. They also observed a reduction of ring artifacts at high count rates in the reconstructed image with that DTC method. The method was developed to use in PET/CT scanners, and it tested for step-and-shoot, the authors noted the plan to use it for the Continuous-bed-motion (CBM) acquisition mode which is used in the whole-body imaging (Siman & Kappadath 2017; Meier et al. 2020). Aykac et al. found that the deviation was about 1.5% at 155 kcps for the uniform cylinder phantom and they did not compare with other DTC methods.

Liu et al. (2019) used a DTC method where they combined a non-paralyzable DT model on block level to compensate for the singles losses with the

paralyzable DT model to compensate for the coincidences losses. For the block-pairwise DTC method, our results were consistent with Liu et al. results, as in our evaluation, the non-paralyzable was shown to be the appropriate model on block detector level. However, we have observed that the energy filtering converts the non-paralyzable behavior into a behavior that is more similar to paralyzable behavior. In addition, they take into consideration the influence of scatter on the DT and the differences in the DTCf for different objects i.e., their size and thickness. They evaluated their method with phantom measurements and showed a primary good response linearity. A comparison with respect to the impact on typical parameters derived from patient or volunteer images was not possible, as in this work no validation using clinical data was done. They developed that method for the UEXPLORER, an ultra-long axial FOV PET scanner. Another approach was presented by Vicente et al. (2013). That method was developed for a small animal PET scanner. They showed

that there is a linear relationship between the singles-to-coincidences ratio (SCR) and the effective DT, where the effective DT includes both DT losses and pile-up losses. That allows them to use a simple DTC method to estimate a DT correction factor and a pile-up correction by using the SCR with two calibration acquisitions, on at high activity and one at low activity. Their results showed that their new DTC method based on SCR correction leads to an improved accuracy of 7% even for high count rates. They compare to the single parameter method and state, which obtained the DT corrections by using a reference acquisition of the intermediate size phantom. That the results of the SCR DTC method prove that they can avoid the bias introduced by single parameter method. The block-wise DTC method studied in the present work, introduces a bias in the DT correction of the coincidences, which is higher and which depends on the chosen energy window.

5.2 Comparison of Global DTC Method and Block-Pairwise DTC Method

The block-pairwise DTC method on which we focused in this work is based on previous work (Yamamoto et al. 1986) which we improved and adapted to the PET system available at our institute where we put emphasize on developing a DTC scheme that is independent of the imaged objects (e.g. object size and activity). More precisely, we apply a DT correction for each individual block pair of the Siemens 3T MR BrainPET insert to obtain the block-pairwise DTC method. In our case, a further improvement of the DTC consists of the implementation of a correction of random triple coincidences. As we described in section 5.1, each block with its associated processing circuitry introduces a dead time according to the block DT constant (which is similar for all blocks). The block detector use light sharing and Anger logic for position and energy determination (Newport et al. 2006, Hu et al. 2011), such that a scintillation event causes DT for the entire block of which the

scintillation pixel is a member of, but not for all scintillation pixels that form part of the same ring as it was the case in the original work from Yamamoto (Grazioso et al. 2006; Zhang et al. 2006). In addition, the total number of delayed random coincidences in a single block pair is lower than the total number of delayed random counts in a single pixel ring (plane) because there are 10944 block pairs in the Siemens 3T MR BrainPET insert but only 72 individual scintillation pixel rings and 32*12 = 384 pixels in each ring. Furthermore, took care to avoid excessive noise propagation into the reconstructed image (equation 3.15), we minimized the use of ratios reported in original work, as the use of ratios potentially amplifies noise. Moreover, the excess counting due to incorrectly handled triple random coincidences and the natural activity of ^{176}Lu were considered in our DTC model. The implemented correction for triple coincidences has shown to lead to a considerable improvement in the block-pairwise DTC results, as the relative error between the observed DT corrected counts and the ideally expected counts is reduced from 4% without

triple correction to a maximum of 1.6 % with triples correction (figure 4.29 and figure 4.34). The original work by (Yamamoto et al. 1986) was shown that relative deviations were achieved of ≈ 1% and it is the same in our case. However, in the case of the original work of Yamamoto et al., the higher accuracy can be explained by the different PET scanner (HEADTOME III, Kanno et al. 1985), which was a 2D-PET system with septa that significantly reduce the effect of the scatter radiation from inside and outside of the FOV. As mentioned, in the other previous studies, relative deviations of up to 7% were reported with their improved dead time correction method based on the global singles-to-coincidences ratio (SCR) for small-animal PET scanners (Vicente et al. 2013). Liu et al. (Liu et al. 2019) reported a maximum bias of 5% in the individual reconstructed image slices when using two different phantoms to validate the block-wise SCR DTC method for a long axial FOV PET scanner. Interestingly, for their own method, there is nearly no difference between DTC corrections assuming a paralyzable and non-paralyzable

behavior, since the count rates were moderate. This is very similar to our observations. Liu et al. also included potential background radiation in their model. The success of the block-pairwise DTC method proves also the hypothesis that the count rates are the main factor for the DTC losses and the differences between DT losses on different blocks. As described in section 5.1, a comparison between a block-pairwise DT correction that uses individual fit parameters for all 10944 block pairs and a block-pairwise DT correction that uses averaged fit parameters does not reveal relevant differences. The observed differences in the fit parameters are most probably caused by component tolerances since the 192 blocks and the associated processing electronics use identical design. The reason for the remaining systematic deviation (see figure 4.26) from an ideal correction whose residuals should be purely randomly distributed around 0 is so far unknown and must be subjected to further investigation. However, there is an apparent similarity in the systematic modulation of the residuals compared to the case without triple coincidence correction.

Therefore, it can be assumed, that the residual systematic deviation from the ideal case is mainly due to an insufficient model for the triple miscount estimation, which was purely empirical in our study, and which neglects multiple coincidences.

As shown in figures 4.35 and 4.36, the DTCf for the blocks-pairs from different rings, and DTCf for the blocks-pairs from different cassettes behave as expected. The unsymmetrical behavior of the DTCf for the blocks-pairs from different rings in case of the measurement without out-of-FOV activity can be explained by the fact that the phantom inside the FOV cannot be placed exactly at the axial center when the Tx/Rx RF head-coil is present. For the measurement with out-of-FOV activity, the block-pairs inside the first ring should show the highest DTCfs, with continuously descending values for the pairs in the other rings from number 2 to 6. In contrast, for the measurement without out-of-FOV activity, the largest DTCfs can be found in ring number 2 but not in rings 3 or 4, which is due to fact that around 2.5 cm of the phantom is located outside

the FOV when the Tx/Rx RF head-coil is present. As expected, there are no systematic variations of the DTCfs averaged over all six blocks in one cassette as can be observed in figure 4.27. The block-pairwise DTC presented more slightly less variations of the COV between different scatter sinogram slices when compared to the global DTC method. However, this effect is most probably too small be noticeable in the images. The measurements with the 3 compartments phantom was used to evaluate the accuracy and the noise behavior of the block-pairwise DTC method in an inhomogeneous object and in comparison to the global DTC method (see figures. 4.31 and 4.32). For the count rates which are used our evaluation with these phantom measurement, no relevant noise propagation into the reconstructed PET images was observed. The accuracy measurements revealed, that the global DTC method leads to an overcorrection, especially in the hot compartment. In compartments with lower activity concentration, a smaller overcorrection was found. For some reason, the axial position of the ROI had only a small impact on

the accuracy of the global DTC method. The axial position of the ROI has a clear influence on the activity concentration reconstructed with the global DTC method. For the hot ROI, we found ≈ 6% overcorrection at the front, 9% at the center, and 13% in the rear part of the FOV. The higher overcorrection in the rear can be explained by the fact that the DTCf takes into account the front part, where count rates are higher due to the out of FOV activity, leading to a positive bias in the DTCf. Interestingly, the 6% overcorrection in the front is close to our cross-calibration factor of 7-8 %.

In contrast, in the block-pairwise, only small overcorrection was observed in the hot compartment for the front ROI and the axially centered ROI. However, no apparent overcorrection was observed in the warm compartment, the background compartment, and the cold (Teflon) compartment when using the block-pairwise DTC method, while there is still a significant overcorrection in the warm compartment when using the global DTC method. Thus, the ROI analysis has shown, that the global

DTC method suffers from overcorrection when compared with the block-pairwise DTC method. For most studied ROIs, the block-pairwise DTC method has a more consistent behavior, in the sense, that the DTC corrected reconstructed activity concentration represented by the image voxel values is nearly a constant independent of the time and therefore independent of the activity in the FOV. This behavior is to be expected for a decay corrected measurement with a static phantom. We attribute the improved stability to the fact that in the block-pairwise DTC method, the count rates are no longer averaged, which means that the difference in the count rates between the front and the rear side is adequately treated in the block-pairwise DTC method, but not in the global DTC method, in which the front we have high counts rates form the activity outside of FOV. The reason for the residual overcorrection of the block-pairwise method in the hot compartment and the axially centered ROI is not understood so far and must be subject to further studies. We suspect that the Single Scatter Simulation (SSS) correction and interference of it

with the DTC is responsible for the axial dependency of the block-pairwise method in the case of the hot compartment. This argument is supported by the residual decrease of the reconstructed activity over time in the cold compartment, even for acquisition times, when there were no DT losses. As in all other ROIS, the two methods converge towards the activity reconstruction without DTC (gray lines in the figure 4.40, and figure 4.41), but in difference to the warm and hot ROI, the TAC without DTC seems to show decreasing tendencies in the front and centered ROI. Figure 4.40 presented the results of the ROIs being much closer to the phantom edges than figure 4.41, but with consistent behavior of the accuracy. Figure 4.42 shows the noise behavior in all ROIs. It is to be expected, that those ROIs, which are closer to the edges of the FOV should show higher noise levels mainly due to lower coincidence detection sensitivity. This expected behavior is reproduced, and it can also be observed, that the COV values are nearly the same for the both DTC methods and the reconstruction without DTC. Consequently, the

image noise is dominated by the image reconstruction and the detection process and there is no significant noise contribution from the DTC. The before mentioned previous studies on DTC (Yamamoto et al. 1986; Vicente et al. 2013; Liu et al. 2019) did not evaluate neither the noise nor the potential bias in phantom measurements (with and without the activity outside of FOV) such that, a comparison of these alternative approaches with our approach can be only limited. The observed relative differences in the calibration analysis of the global and the block-pairwise DTC methods (table 4.2) showed that we have a residual inaccuracy in the block-pairwise correction, which most probably also can be attributed to the inaccuracies of the SSS correction. Importantly, the lack of accuracy especially of the global method should be taken into account for the future regular calibration in the Siemens 3T MR BrainPET insert, since the overcorrection of the global DTC method propagates into the calibration factor, as the calibration is currently done using the global DTC method. This is especially important in the case of

calibration at high activity levels. In addition, the bias in the global DTC based calibration factor needs to be addressed when comparing the reconstructed images with different activity levels and different DTC methods. This was done in this work by determining the cross-calibration factor between the global and the block-pairwise DTC methods. When evaluating the calibration values for phantom measurements with and without out-of-FOV activity, there are still differences, also for the block-pairwise DTC method. However, these are smaller than for the global DTC method. Again, they are potentially due to the known deficiencies of the SSS.

5.3 Impact of DTC Methods on Volunteers & Patients Measurements

The quantitative accuracy of PET images is in general sufficient for clinical neurological and neurooncological applications, but not for neuroscientific applications. As shown, the DT losses affect the accuracy of the reconstructed

images by underestimation of the pixel values (in case of no DTC at all), and inadequate DTC methods result in a systematic and relevant bias of the TACs and derived micro- and macro parameters. As seen in figure 4.43, also in volunteer and patient images, large differences in the DTC factors can be observed between the global DTC and the block-pairwise DTC and also between different block-pairs in the case of the block-pairwise DTC. These observations are consistent with the described results and findings of the phantom measurement, and, according to the observation made there, it must be assumed, that the global DTC introduces also a bias into the TAC of volunteer and patient measurements. For the validation of the impact of the block-pairwise DTC method on human PET images and derived micro and macro parameters, we have compared the results of the images reconstructed with the block-pairwise and the global DTC method for three different radioactive tracers and two different administration schemes, where we have chosen nuclides with considerably different physical half-lives for the

selected tracer. We observed relative differences for all tracer and both administration schemes.

I. Validation of block-pairwise DTC method with the[^{11}C]ABP688 PET Images

For the first test application, we have chosen a ^{11}C based tracer for its intermediate half-life. The [^{11}C]ABP688 measurement was done with a bolus-infusion protocol and in which the BP_{ND} was determined in the time of $\approx$ 30 (1800) to 60 (3600) min (sec) p.i.. Even with the rather small difference of the global DTCf compared to the block-pairwise DTCf in that interval (figure 4.43), there still an observable difference of $\approx$ 2% in the BP_{ND} for some of the ROIs. As the difference of the DTC factors is time dependent, also the BP_{ND} will be time dependent (figure 4.44), in a way that they can mask real BP_{ND} changes induced by cognitive challenges (Régio Brambilla et al. 2022). The [^{11}C]ABP688 was therefore used as an exemplary application for the determination of the V_T and BP_{ND} after reaching an equilibrium of the receptor-ligand in the studied

brain regions. Owing to the nuclide and the activity application scheme, the TACs for this application are characterized by fast changing activity in the PET FOV during the bolus phase and a moderate changing activity in the PET FOV after reaching the equilibrium. We observed relevant differences in the slope of the distribution volume after reaching the equilibrium. We observed them for all three studied regions depending on the used DTC method. The TACs of the global method show an overcorrecting behavior compared with the block-pairwise method, consistent with the phantom measurement. As the same phantom studies revealed a residual overcorrection in the image activity concentrations reconstructed with block-pairwise DTC at least for high activity regions, we cannot completely exclude, that the TACs observed in volunteer measurements and reconstructed with block-pairwise DTC may exhibit also residual bias, which is however in all cases lower than the bias introduced by the global DTC. As explained above, the calibration of the used PET system is done with images reconstructed with global DTC, which needs to be compensated by

either calibrating the system also for the block-pairwise DTC or by applying a cross-calibration factor, with was done in our case. The observed rather large inaccuracies of the global method can result in relevant quantitation errors in human studies, especially since it is changing over time depending on the brain region. Although not relevant for the present bolus-infusion protocol investigation, the early part of the TACs allows an important conclusion for dynamic studies using a bolus injection protocol and kinetic modelling, which requires evaluating the entire TAC to derive the BP_{ND} outcome. This can be explained by the fact that for the determination of $V_{T,}$ the reconstructed image activity concentration is related to the activity concentration in the blood-plasma, which itself is not affected by differences of both DTC methods. However, when computing the BP_{ND} from the reconstructed image activity concentrations using the ratio method (figure 4.45), the differences due to the DTC method cancel out to a large extent. Following the same argumentation, the global DTC method introduces a small bias especially for the

determined $V_{T,}$ which moreover, is different for the three regions (figure 4.47). These differences must be expected for two reasons. The first one is the bolus-infusion scheme does not guarantee that an equilibrium is reached in all brain regions (Régio Brambilla et al. 2020; Akkus et al. 2014; Deschwanden et al. 2011). Therefore, it seems that on average, a slope of 0 $ml \cdot cm^{-3} \cdot min^{-1}$ is reached in the cerebellum when using the global DTC method, but not when using the block-pairwise DTC method. This is due to the fact that the bolus-infusion scheme for the underlying study was adjusted before the availability of the block-pairwise DTC method (Brambilla et al. 2021). In the temporal posterior lobe, a slope of 0 $ml \cdot cm^{-3} \cdot min^{-1}$ is reached with the block-pairwise DTC method instead, but not with the global DTC method. In the ACC, a slope of 0 $ml \cdot cm^{-3} \cdot min^{-1}$ is neither reached with the global nor the with block-pairwise DTC method. The second reason for this behavior is the axial asymmetry of the DT losses, which is caused by the out-of-FOV activity caused by mainly the torso of patient. This leads to higher irradiation of the scintillation

detectors at the front end of the PET ring and consequently introduces a dependency of the DTC differences on the VOIs axial location. We have found that the overestimation of the early TACs for the ACC is larger than in the cerebellum TACs by the global DTC (figure 4.46). The overestimation has not had constant behavior and sometimes it decreased towards later times. That means the prerequisite for kinetic modeling of dynamic studies concerning spatial and temporal invariance is violated in those cases. However, the difference between the high counts and the low counts over the scan time of the familiar typical dynamic neuroreceptor studies with a bolus injection can be even greater than what we observed in the presented study.

II. Validation of block-pairwise DTC method with [^{18}F]-FET-PET Images

The [^{18}F]-FET-PET was used as exemplary application for tumour imaging in the human brain. The TACs for this application are characterized by

fast changing activity at the beginning of the PET scan and a continuously deceleration of the change towards the end of the PET scan. Figure 4.48 shows that the TACs for global DTC leads again to an overcorrection compared to the block-pairwise DTC, which is compatible with the results from the phantom measurements. Except for the Tumor-Max V(R)OI, the TACs obtained with global and cross-calibrated block-pairwise DTC lead to nearly identical values. However, in the Tumor-Max V(R)OI, the TAC obtained with the global DTC method shows and relevant overcorrection when compared to TAC for the cross-calibrated block-pairwise method. Consequently, as the global DTC method was shown to introduce substantial bias, we have to assume that the global DTC leads to an overcorrection in this case to, and therefore negatively affects the accuracy of the Tumor-Max value. However, the TAC shapes of dynamic [^{18}F]-FET-PET scans lead to very comparable distributions of the shape parameter κ (Lerche et al., 2021) for both of the global and block-pairwise DTC methods (figure 4.49). Also, the relevant parameters

as the ratios TBR_{max} and TBR_{mean} give rise to very comparable distributions when based on reconstructions with the both different DTC schemes, although rather large differences of up to 20% can be observed for individual cases (figure 4.50). However, when arranging differences in TBR_{max} and TBR_{mean} caused by the DTC methods according to tumor size and distance of the tumor from the BrainPET inserts FOV, a significant dependency of TBR_{max} on the tumor distance can be found. In addition, there seems to be a slight dependency on the tumor size too, which is however not significant. This observation can again be explained by the asymmetry in the DT losses for individual detector blocks, which is larger the larger the distance of the tumor from the iso-center is. In the case of TBR_{mean}, these differences seem to average effectively out. As a consequence of these observations, it must be assumed that the global DTC method mainly increased the variance of TBR_{max} by introducing case dependent biases. (figure 4.51 and table 4.3).

III. Validation of block-pairwise DTC method with [^{15}O]H_2O PET Images

The [^{15}O]H_2O was used to study the impact of the improved DTC on kinetic parameters obtained by modelling using the one tissue compartment model. The TACs for this application are characterized by a very fast changing activity in the PET FOV over the entire scan time. Also in this case, differences between the global and the block-pairwise DTC method were observed, and it must be assumed, that also in this case the global DTC led to an overcorrection of the TAC which led to a potential bias in all derived quantities, while, based on the phantom measurements, higher accuracy can be expected for the block-pairwise DTC. This observation is in agreement with motivation of the original DTC method (Yamamoto et al. 1986), which was developed to accurately correct TAC curves for the fast kinetic modeling of the [^{15}O]H_2O, and which was adapted in the present work.

A comparison between global and block-pairwise DTC methods reveals that a small but consistent bias

around 3-7 % is introduced for all four considered parameters rCBF, K_1, k_2, and V_T for the GM region and the WM region. Interestingly, this bias is an overestimation in all cases except for V_T in the WM region. So far, we have no explanation for this exception (table 4.4 and figure 4.43).

For the rCBF comparison, the results we have are very comparable with the previous studies and the main original work of (Zhang et al. 2014). Zhang et al. (2014), showed that the measured CBF by Pseudo-continuous ASL (pCASL) was an average of 51.9±7.1 mL per 100 g per minute in GM. Our results are compatible with these previous results (Xu et al. 2010), i.e. the mean of the rCBF GM in (Wilke et al. 2007; Karas et al. 2004) was 48.02 mL per 100 g per minute and the mean of the rCBF WM was 20.16 mL per 100 g per minute. Fan et al. (2016) obtained a rCBF GM was 53.9±11 mL per 100 g per minute. Ishii et al. (2020) obtained from phase-contrast (PC-PET) (the blood-free approach, i.e., a noninvasive method to quantify absolute CBF with a PET/MRI hybrid scanner) ≈ 52.0 mL per 100 g per minute as mean value for rCBF GM in the range of

34.5–67.0 mL per 100 g per minute and a mean value of ≈ 22.2 mL per 100 g per minute for rCBF WM in the range of 17.4–33.0 mL per 100 g per minute. They observe a mean GM/WM ratio of ≈ 2.3 in the range between 1.4 and 3.2. Zhang et al. (2014) observed a GM/WM ratio of 3.0 obtained from PET images. Thus, the values for the GM/WM ratio obtained in our study are comparable to the values obtained in previous studies (Ishii et al. 2020; Mutsaerts et al. 2014), our values are lower than others due to the known problem of the ML-EM reconstruction bias, which however does not interfere with the DTC. Interestingly, when using block-pairwise DTC, a higher rCBF values for the GM and WM regions is obtained in comparison to using global DTC method (figure 4.45). However, even with the block-pairwise DTC method, the rCBF ratio is lower than the expected value of 3.0 in (Zhang et al. 2014). The deviations from the expected values are most probably due to the known bias of ML-EM reconstruction at low counts (Herbert 1990; Shepp & Vardi 1982). Different modelling procedures were applied in our case and

in the work from Zhang et al. 2014. We used the General Kinetic Modeling Tool (PKIN) available in PMOD together with the sequence of dynamic [^{15}O]H_2O images, whereas (Zhang et al. 2014) obtained their results by exploiting just a single PET [^{15}O]H_2O image applying the PXMOD tool of PMOD (Herscovitch et al. 1983). Images with short time frames are more sensitive to the bias of the ML-EM reconstruction because of their inherently lower counts compared an PET images over long time frames.

In general, very few studies have investigated the DT effects and mainly in other imaging modalities such as SPECT, thus a comparison of the results is very difficult (Uribe et al. 2018; Inoue et al. 1997; Cohalan et al. 2020, Vicente et al. 2013). Inoue et al. (1997) showed that DT losses have a substantial effect on the measurements of cerebral blood flow when measured by radionuclide angiography using SPECT and ^{99}mTc-HMPAO. The study showed that uncorrected DT count losses result in the overestimation of the calculated values in the TACs, thus obtaining also the conclusion that DTC has a

high impact on quantitation. Uribe et al. (2018) investigated the impact of different DTC on ^{177}Lu images obtained again with SPECT and after radionuclide therapy. However, the DTC methods which were compared in this study did not reveal in detail, if a global or block-wise DTC was used. However, they differ in the used energy acceptance window. Moreover, in that study, only the differences in the DTC factors but no patient-related quantities are reported. Vicente et al. (2013) evaluated an alternative DTC method for small animal PET using simulations and phantoms. Their focus was to lower the accuracy dependency of the DTC on the activity level in the PET FOV reporting a maximum deviation from the ground truth of 7%. We studied this for the evaluated block-pairwise method and found that deviations from the ground truth are smaller than 1.4% in all cases. Cohalan et al. (2020) also studied the impact of different DTC on ^{177}Lu images obtained again with SPECT in a phantom study. They compared a global DTC correction to a DTC for individual projections and report relative quantitation differences in the range

from -1% to 3%, which are comparable with our observations, although measured with a different modality. Freedman et al. (1992) examined the distribution of single rates of the PET scanner during cardiac studies with bolus injections of [^{15}O]H_2O and ^{82}Rb and with slow infusion of static [^{18}F]FDG studies. They came to the same conclusion, which were found in this work, that the DT losses depend on the activity and that there were large differences in local single count rates. The study also showed that DTC methods, which use spatially averaged DT loss determination (as in our case the global DTC method) can lead to inaccurate estimation of the absolute activity concentration, therefore creating regional errors.

All observations and considerations which we presented may also be relevant for DTC in other PET systems. Although from the geometry of the scanner and the positioning of the objects we expect a less significant impact on the insufficiencies of global DTC, the effects should be studied in detail in independent research work on the target PET system. However, the presented results will be

equally relevant for other dedicated brain PET devices which have been developed during recent years or are currently being developed, e.g. (Jung et al. 2015, Nishikido et al. 2017, Del Guerra et al. 2018, Gonzalez et al. 2018, Teimoorisichani and Goertzen 2018, Catana 2019, Moliner et al. 2019, Ahnen et al. 2020, Lerche et al. 2020, Carson et al. 2021).

In conclusion, a more accurate DTC method, the block-pairwise DTC method, was developed for the dedicated Siemens 3T MR BrainPET insert. The DTC method was evaluated and validated against the current DTC method (global) and partly also against the block-wise DTC method. The block-pairwise DTC method was successfully implemented on our BrainPET insert and it is based on the estimation of the DTC factor from the delayed random coincidences between individual block pairs. It further includes a correction for detected random triple coincidences and the ^{176}Lu background introduced by the scintillator. The

evaluation of the accuracy of the block-pairwise DTC method was done by using different phantom measurements, i.e., a Germanium Quality control phantom, several phantoms homogenously filled with high activity of ^{18}F with and without an additional phantom to emulate activity outside of the FOV, a multi-compartment phantom filled with different activity concentrations and with an additional phantom to emulate out-of-FOV activity. The validation of the block-pairwise DTC method was done with PET measurements of volunteers using different tracers an activity application schemes. The quantification bias introduced by the newly developed DTC method was significantly smaller in all evaluated compartments and ROIs. The phantom measurements also revealed that the bias introduced by the global DTC method propagates into the calibration factor. This requires either a recalibration of the PET system using the newly developed block-pairwise DTC, or, as done in the present work, the measurement and application of a cross-calibration factor of the block-pairwise DTC against the global DTC method.

The improvement in the quantitation accuracy which was achieved with the improved DTC method is potentially of high relevance for PET studies that aim at the investigation parameters such as the distribution volume and the binding potential in research settings. Although the validation of the block-pairwise DTC accuracy was done choosing quantitative and semiquantitative measurements of three applications with several tracers, which are representative and relevant for clinical PET and PET in research. The validation included [^{11}C]ABP688 TACs and derived quantities, [^{18}F]-FET-PET TACs and derived quantities, and [^{15}O]H_2O TACs and derived quantities. The evaluation of the new DTC revealed that the method takes count rate differences due to block position, the symmetry of the activity distribution concerning the BrainPET scanner's geometry adequately into account. Further, it accurately handles the introduced bias which depends on the amount of activity from outside of the FOV, i.e., the remainder of the body in the case of the brain imaging with a dedicated BrainPET insert. Thus, the accuracy improvement can be

expected to be especially relevant for the Siemens 3T MR BrainPET insert, as typical whole-body PET scanner normally have scatter shields, and as the activity distribution inside the PET FOV is more homogeneous in these devices. For all studied applications, we found that the global DTC introduces an overcorrection in the TACs which lead to a bias in the studied derived quantitative parameters. This bias is it considerably reduced with the block-pairwise DTC method. In case of [^{11}C]ABP688 measurements, especially the V_T was affected by the bias with differences between both DTC methods of up to 0.005 ml·cm^{-3}·min^{-1}. The observed relative difference ratios between the global DTC method and the block-pairwise DTC methods ranged from 1.4 to 1.1 in a non-linear manner in the course of the study indicating the region-dependent and the time-dependent overestimation by the global DTC method. These differences could lead to a misinterpretation of results, e.g., the masking of the effects that cognitive tasks have on the TACs in the ROI and the reference region. For [^{18}F]-FET-PET, differences in TBR_{max}

of up to 10% were observed. The differences ratio of the twenty cases was around 4.4% in the TBR_{max} and TBR_{mean} between the global and the block-pairwise DTC methods. In addition, these differences depend on the distance of the tumor from the PET iso-center. For the $[^{15}O]H_2O$ measurements, we observed mean relative differences for the studied kinetic parameters rCBF, K_1, k_2, and V_T between +4% and -7%. Except for V_T in WM, all modelled parameters were overestimated when using the global DTC method. The rCBF GM/WM ratio was very comparable with previous typical studies. The GM/WM ratio was ≈ 2.5 for both DTC methods.

Finally, the method can be implemented in all systems that use the delayed window technique and is particularly expected to improve the quantitation accuracy of dedicated brain PET scanners due to their geometry. The observed differences between the two DTC methods are particularly relevant for research applications in neuroscientific studies as they affect the accuracy of the quantification of the PET brain images.

In future work, the presented DTC method for BrainPET should be tested on other PET scanners, as, for instance, the newly developed BrainPET 7T system. For this system, the method potentially needs to be adapted, as the assumption, that an entire scintillation block detector is completely paralyzed after a scintillation event in one of its pixels, is no longer valid. Further, the reasons for the residual bias introduced by the block-pairwise DTC method in the hot compartment needs to be addressed in a detailed way. Although we assume deficiencies of the single scatter correction to be responsible for it, we could not prove this assumption. Also, the empirical model for the overestimation due to triple coincidences which has been used in the mathematical model of the block-pairwise DTC method potentially can be improved, if a the overcounting is better understood. Finally, a validation of the block-pairwise DTC method for additional applications with volunteers and patients could be of high interest. For instance, a study run on our institute with [^{11}C]-Flumazenil was not conclusive so far, which may be due to the

deficiencies of the global DTC method. The application of the new DTC method to the acquired data of this study would also allow to evaluate the impact of the improved DTC on irreversible tracers that require a two tissue compartment model for the kinetic modelling.

6. Summary

Dead time correction (DTC) is of high significance for accurate quantification in PET, just like other corrections for attenuation, decay, and scatter. Many PET systems use the global DTC, i.e., an average DTC factor is computed for all scintillation detector blocks of the system. However, the count rates of the individual scintillation detector blocks are potentially very different due to the individually varying irradiation of each block detector, especially for systems where the allocation of radiation shields is not possible, as in the case of our dedicated Siemens 3T MR BrainPET insert. For that reason, we have developed a block-pairwise DTC. In our approach, we extended a previously published method that uses the delayed random coincidence count rate to estimate the dead time in the individual blocks and planes. This DTC was evaluated with decay experiments using phantom measurements with homogenous and inhomogeneous activity concentrations and with and without out-of-FOV

activity. We compared the accuracy and the noise behavior with measurements using a 3-compartment phantom. Moreover, we showed that the global and the improved block-pairwise DTC require different calibration. Therefore, we cross-calibrated both methods against each other. The differences in the quantification of the BrainPET images were evaluated by using several radioactive tracers. For this, we validated the method by quantifying the impact on [^{11}C]ABP688 time-activity curves (TACs) and derived quantities such as the non-displaceable binding potential (BP_{ND}) and the total distribution volume (V_T). We further studied the new method's impact on O-(2-[^{18}F]fluoroethyl)-L-tyrosine (FET) TACs and tumor to background ratios (TBR_{max} and TBR_{mean}) and we evaluated the impact on [^{15}O]H_2O TACs and the rate constants K_1 and k_2, the regional cerebral blood flow (rCBF), and the V_T obtained by kinetic modeling. The phantom measurements showed that the global DTC led to significant quantification biases in mainly those regions with high activity concentrations, while the block-pairwise DTC led to substantially less bias.

The noise level was comparable for both methods. The evaluation of typical applications in volunteer and patient measurements revealed relevant differences between the two DTC, particularly relevant for research applications in neuroscientific studies. In case of PET imaging with [^{11}C]ABP688 we found a relevant bias of V_T in all studied brain regions when using the global DTC. For [^{18}F]-FET-PET, differences in TBR_{max} of up to 10% were observed when comparing both DTC methods. These differences depend on the distance of the tumor from the PET iso-center. For [^{15}O]H_2O, we found relevant biases for rCBF, K_1, k_2, and V_T in the both regions (GM and WM).

7. References

Acerbi, F. and Gundacker, S., 2019. Understanding and simulating SiPMs. Nuclear Instruments and Methods in Physics Research Section A: Accelerators, Spectrometers, Detectors and Associated Equipment, 926, pp.16-35. https://doi.org/10.1016/j.nima.2018.11.118

Ahnen, M. L., Fischer, J., Kuegler, N., Mikhaylova, E., Becker, R., Lustermann, W., & Dissertori, G. Performance of the Ultra-Compact Fully Integrated Brain PET System BPET. In 2020 IEEE Nuclear Science Symposium and Medical Imaging Conference (NSS/MIC) (pp.1-4). IEEE. https://doi.org/10.1109/NSS/MIC42677.2020.9508026

Akkus, F., Mihov, Y., Treyer, V., Ametamey, S.M., Johayem, A., Senn, S., Rösner, S., Buck, A. and Hasler, G., 2018. Metabotropic glutamate receptor 5 binding in male patients with alcohol use disorder. Translational psychiatry,8(1),pp.1-8. https://doi.org/10.1038/s41398-017-0066-6

Akkus, F., Terbeck, S., Ametamey, S.M., Rufer, M., Treyer, V., Burger, C., Johayem, A., Mancilla, B.G., Sovago, J., Buck, A. and Hasler, G., 2014. Metabotropic glutamate receptor 5 binding in patients with obsessive-compulsive disorder. International journal of neuropsychopharmacology, 17(12), pp.1915-1922. https://doi.org/10.1017/S1461145714000716

Albert, G.E. and Nelson, L., 1953. Contributions to the statistical theory of counter data. The Annals of Mathematical Statistics, pp.9-22. https://doi.org/10.1214/aoms/1177729079

Álvarez-Gómez, J.M., Santos-Blasco, J., Moliner Martínez, L. and Rodríguez-Álvarez, M.J., 2021. Fast energy dependent scatter correction for list-mode PET data. *Journal of imaging*, *7*(10), p.199. https://doi.org/10.3390/jimaging7100199

Alva-Sánchez, H., Zepeda-Barrios, A., Díaz-Martínez, V.D., Murrieta-Rodríguez, T., Martínez-Dávalos, A. and Rodríguez-Villafuerte, M., 2018. Understanding the intrinsic radioactivity energy spectrum from 176Lu in LYSO/LSO scintillation crystals. Scientific reports, 8(1), pp.1-7. https://doi.org/10.1038/s41598-018-35684-x

Aykac, M., Panin, V.Y. and Bal, H., 2017, October. Crystal-based deadtime correction for Siemens next generation SiPM based PET/CT scanner. In 2017 IEEE Nuclear Science Symposium and Medical Imaging Conference (NSS/MIC) (pp. 1-5). IEEE. https://doi.org/10.1109/NSSMIC.2017.8532923.

Badawi, R.D., 2001. Nuclear medicine. Physics education, 36(6), p.452. https://doi.org/10.1088/0031-9120/36/6/302

Badawi, R.D., Marsden, P.K., Cronin, B.F., Sutcliffe, J.L. and Maisey, M.N., 1996. Optimization of noise-equivalent count rates in 3D PET. Physics in Medicine & Biology,41(9), p.1755. https://doi.org/10.1088/0031-9155/41/9/014

Baerg, A.P., 1965. Variation on the paired source method of measuring dead time. Metrologia, 1(3), p.131. https://doi.org/10.1088/0026-1394/1/3/005

Bailey, D. L., Maisey, M. N., Townsend, D. W., & Valk, P. E. (2005). Positron emission tomography (Vol. 2, p. 22). London: Springer.

Bailey, D.L. and Humm, J.L., 2014. Nuclear medicine physics: a handbook for teachers and students. Iaea.

Bécares, V. and Blázquez, J., 2012. Detector dead time determination and optimal counting rate for a detector near a spallation source or a subcritical multiplying system. Science and Technology of Nuclear Installations, 2012. https://doi.org/10.1155/2012/240693

Beers, Y., 1942. A precision method of measuring Geiger counter resolving times. Review of Scientific Instruments, 13(2), pp.72-76. https://doi.org/10.1063/1.1769976

Berthelsen, A.K., Dobbs, J., Kjellén, E., Landberg, T., Möller, T.R., Nilsson, P., Specht, L. and Wambersie, A., 2007. What's new in target volume definition for radiologists in ICRU Report 71? How can the ICRU volume definitions be integrated in clinical practice?. Cancer Imaging, 7(1), p.104. https://doi.org 10.1102/1470-7330.2007.0013

Bock, R.K., Grote, H. and Notz, D., 2000. Data analysis techniques for high-energy physics (Vol. 11). Cambridge University Press.

Bol, A., Vanmelckenbeke, P., Michel, C., Cogneau, M. and Goffinet, A.M., 1990. Measurement of cerebral blood flow with a bolus of oxygen-15-labelled water: comparison of dynamic and integral methods. European journal of nuclear medicine, 17(5), pp.234-241. https://doi.org/10.1007/BF00812363

Brambilla, C. R., Scheins, J., Issa, A., Tellmann, L., Herzog, H., Rota Kops, E., ... & Lerche, C. W. (2021). Bias evaluation and reduction in 3D OP-OSEM reconstruction in dynamic equilibrium PET studies with 11C-labeled for binding potential analysis. Plos one, 16(1), e0245580.https://doi.org/10.1371/journal.pone.0245580

Brasse, D., Kinahan, P.E., Lartizien, C., Comtat, C., Casey, M. and Michel, C., 2005. Correction methods for random coincidences in fully 3D whole-body PET: impact on data and image quality. Journal of nuclear medicine, 46(5), pp.859-867. PMID: 15872361

Brun, R. and Rademakers, F., 1997. ROOT—An object oriented data analysis framework. Nuclear instruments and methods in physics research section A: accelerators, spectrometers, detectors

and associated equipment, 389(1-2), pp.81-86. https://doi.org/10.5281/zenodo.3895860

Caldeira, L., Kops, E. R., Yun, S. D., da Silva, N., Mauler, J., Weirich, C., ... & Shah, N. J. (2018). The jülich experience with simultaneous 3t mr-brainpet: Methods and technology. IEEE transactions on radiation and plasma medical sciences, 3(3), 352-362. https://doi.org/10.1109/TRPMS.2018.2863953

Cal-González, J., Herranz, E., Vicente, E., Udías, J.M., Dave, S.R., Parot, V., Lage, E. and Herraiz, J.L., 2013. Simulation of triple coincidences in PET. In 2013 IEEE Nuclear Science Symposium and Medical Imaging Conference (2013 NSS/MIC) (pp. 1-4). IEEE. https://doi.org/10.1109/NSSMIC.2013.6829155

Cal-González, J., Lage, E., Herranz, E., Vicente, E., Udías, J. M., Moore, S. C., ... & Herraiz, J. L. (2014). Simulation of triple coincidences in PET. Physics in Medicine & Biology, 60(1), 117. https://doi.org/10.1109/NSSMIC.2013.6829155

Carson, R., Berg, E., Badawi, R., Cherry, S., Du, J., Feng, T., & Li, H. (2021). Design of the NeuroEXPLORER, a next-generation ultra-high

performance human brain PET imager. https://doi.org/10.1088/1361-6560/ac195d

Catana, C. (2019). Development of dedicated brain PET imaging devices: recent advances and future perspectives. Journal of Nuclear Medicine, 60(8), 1044-1052. https://doi.org/10.2967/jnumed.118.217901

Catana, C., 2015, May. Motion correction options in PET/MRI. In Seminars in nuclear medicine (Vol. 45, No. 3, pp. 212-223). WB Saunders. https://doi.org/10.1053/j.semnuclmed.2015.01.001

Cavalcanti, Y.C., Oberlin, T., Dobigeon, N., Févotte, C., Stute, S., Ribeiro, M.J. and Tauber, C., 2019. Factor analysis of dynamic PET images: beyond Gaussian noise. IEEE transactions on medical imaging, 38(9), pp.2231-2241. https://doi.org/10.1109/TMI.2019.2906828

Centore, P., 2016. The coefficient of variation as a measure of spectrophotometric repeatability. Color Research & Application, 41(6), pp.571-579. https://doi.org/10.1002/col.22002

Chandra, A., Li, W.A., Stone, C.R., Geng, X. and Ding, Y., 2017. The cerebral circulation and cerebrovascular

disease I: Anatomy. Brain circulation, 3(2), p.45. https://doi.org/10.4103/bc.bc_10_17

Chen, K., Reiman, E., Lawson, M., Feng, D. and Huang, S.C., 1995. Decay correction methods in dynamic PET studies. IEEE Transactions on nuclear science,42(6),pp.2173-2179. https://doi.org/10.1109/23.489413

Cherry, S.R. and Dahlbom, M., 2006. PET: physics, instrumentation, and scanners. In PET (pp. 1-117). Springer, New York, NY.

Cohalan, C., Morin, M.A. and Leblond, A., 2020. Practical considerations for establishing dead-time corrections in quantitative SPECT imaging. Biomedical Physics & Engineering Express, 6(2), p.027001. https://doi.org/10.1088/2057-1976/ab7500

Constantinescu, C.C. and Mukherjee, J., 2009. Performance evaluation of an Inveon PET preclinical scanner. Physics in Medicine & Biology, 54(9), p.2885.https://doi.org/10.1088/0031-9155/54/9/020

Del Guerra, A., Ahmad, S., Avram, M., Belcari, N., Berneking, A., Biagi, L., & TRIMAGE Consortium. (2018). TRIMAGE: A dedicated trimodality (PET/MR/EEG) imaging tool for

schizophrenia. European psychiatry, 50, 7-20. https://doi.org/10.1016/j.eurpsy.2017.11.007

Del Guerra, A., Belcari, N., Bisogni, M.G., Llosá, G., Marcatili, S. and Moehrs, S., 2009. Advances in position-sensitive photodetectors for PET applications. Nuclear Instruments and Methods in Physics Research Section A: Accelerators, Spectrometers, Detectors and Associated Equipment, 604(1-2), pp.319-322. https://doi.org/10.1016/j.nima.2009.01.034

Derlin, T., Grünwald, V., Steinbach, J., Wester, H.J. and Ross, T.L., 2018. Molecular imaging in oncology using positron emission tomography. Deutsches Ärzteblatt International, 115(11), p.175. https://doi.org/10.3238/arztebl.2018.0175

Deschwanden, A., Karolewicz, B., Feyissa, A.M., Treyer, V., Ametamey, S.M., Johayem, A., Burger, C., Auberson, Y.P., Sovago, J., Stockmeier, C.A. and Buck, A., 2011. Reduced metabotropic glutamate receptor 5 density in major depression determined by [11C] ABP688 PET and postmortem study. American Journal of Psychiatry, 168(7), pp.727-734. https://doi.org/10.1176/appi.ajp.2011.09111607

El-Ghossain, M.O., 2017. Calculations of stopping power, and range of ions radiation (alpha particles) interaction with different materials and human body parts. International Journal of Physics, 5(3), pp.92-98. https://doi.org/10.12691/ijp-5-3-5.

Ensslin, N. (1991). Principles of neutron coincidence counting. Passive Nondestructive Assay of Nuclear Materials, 550. https://www.lanl.gov/org/ddste/aldgs/ssttraining/_assets/docs/PANDA/Principles%20of%20Neutron%20Coincidence%20Counting%20Ch.%2016%20p.%20457-492.pdf

Fan, A.P., Jahanian, H., Holdsworth, S.J. and Zaharchuk, G., 2016. Comparison of cerebral blood flow measurement with [15O]-water positron emission tomography and arterial spin labeling magnetic resonance imaging: a systematic review. *Journal of Cerebral Blood Flow & Metabolism*, *36*(5), pp.842-861. https://doi.org/10.1177/0271678X16636393

Filss, C. P., Albert, N. L., Böning, G., Kops, E. R., Suchorska, B., Stoffels, G., Galldiks, N., Shah, N. J., Mottaghy, F. M., Bartenstein, P., Tonn, J. C., & Langen, K. J. (2017). O-(2-[18F]fluoroethyl)-L-tyrosine PET in gliomas: influence of data processing

in different centres. EJNMMI research, 7(1), 64. https://doi.org/10.1186/s13550-017-0316-x

Fletcher, J.W. and Kinahan, P.E., 2010. PET/CT standardized uptake values (SUVs) in clinical practice and assessing response to therapy. NIH Public Access, 31(6), pp.496-505. https://doi.org/10.1053/j.sult.2010.10.001

Freedman, N. M., Bacharach, S. L., McCord, M. E., & Bonow, R. O. (1992). Spatially dependent deadtime losses in high count rate cardiac PET. Journal of nuclear medicine: official publication, Society of Nuclear Medicine, 33(12), 2226-2231. PMID: 1460521. https://europepmc.org/article/med/1460521

Fuenfgeld, B., Mächler, P., Fischer, D.R., Esposito, G., Rushing, E.J., Kaufmann, P.A., Stolzmann, P. and Huellner, M.W., 2020. Reference values of physiological 18F-FET uptake: Implications for brain tumor discrimination. PLoS One, 15(4), p.e0230618. https://doi.org/10.1371/journal.pone.0230618

Gonzalez, A. J., Gonzalez-Montoro, A., Vidal, L. F., Barbera, J., Aussenhofer, S., Hernandez, L., & Benlloch, J. M. (2018). Initial results of the MINDView PET insert inside the 3T mMR. IEEE Transactions on

Radiation and Plasma Medical Sciences, 3(3), 343-351. https://doi.org/10.1109/TRPMS.2018.2866899.

Grazioso, R., Zhang, N., Corbeil, J., Schmand, M., Ladebeck, R., Vester, M., Schnur, G., Renz, W. and Fischer, H., 2006. APD-based PET detector for simultaneous PET/MR imaging. Nuclear Instruments and Methods in Physics Research Section A: Accelerators, Spectrometers, Detectors and Associated Equipment,569(2),pp.301-305. https://doi.org/10.1016/j.nima.2006.08.121

Grosu, A.L., Sprague, L.D. and Molls, M., 2006. Definition of target volume and organs at risk. Biological target volume. In New Technologies in Radiation Oncology (pp. 167-177). Springer, Berlin, Heidelberg. http://eknygos.lsmuni.lt/springer/315/167-177.pdf

Gunn, R.N., Gunn, S.R. and Cunningham, V.J., 2001. Positron emission tomography compartmental models. Journal of Cerebral Blood Flow & Metabolism, 21(6), pp.635-652.https://doi.org/10.1097/00004647-200106000-00002

Hammers, A., Allom, R., Koepp, M.J., Free, S.L., Myers, R., Lemieux, L., Mitchell, T.N., Brooks, D.J.

and Duncan, J.S., 2003. Three-dimensional maximum probability atlas of the human brain, with particular reference to the temporal lobe. Human brain mapping, 19(4), pp.224-247. https://doi.org/10.1002/hbm.10123

Hasegawa, T., Yoshida, E., Yamaya, T., Maruyama, K. and Murayama, H., 2004. On-clock non-paralyzable count-loss model. Physics in Medicine & Biology, 49(4), p.547. https://doi.org/10.1088/0031-9155/49/4/006

Herbert, T.J., 1990. Statistical stopping criteria for iterative maximum likelihood reconstruction of emission images. Physics in Medicine & Biology,35(9),p.1221. https://doi.org/10.1088/0031-9155/35/9/003

Herscovitch, P., Markham, J. and Raichle, M.E., 1983. Brain Blood Flow Measured with Intravenous H215O.: I. Theory and Error Analysis. *Journal of Nuclear Medicine*, *24*(9),pp.782-789. https://jnm.snmjournals.org/content/jnumed/24/9/782.full.pdf

Herzog, H., Iida, H. and Caldeira, L., 2018. Kinetic Modelling and Extraction of Metabolic Parameters. In

Hybrid MR-PET Imaging (pp. 183-202). https://doi.org/10.1039/9781788013062-00183

Herzog, H., Langen, K. J., Weirich, C., Kops, E. R., Kaffanke, J., Tellmann, L., ... & Shah, N. J. (2011). High resolution BrainPET combined with simultaneous MRI. Nuklearmedizin, 50(02), 74-82. https://doi.org/10.3413/Nukmed-0347-10-09

Hoffman, E., Phelps, M., & Huang, S. C. (1983). Performance Evaluation of a Positron Tomograph Designed for Brain Imaging. https://doi.org/10.2967/jnumed.110.085738

Hu, D., Siegel, S. B., Wu, H., Wen, J., Ravindranath, B., & Tai, Y. C. (2011, October). Extending QuickSilver™ electronics for PET insert integration. In 2011 IEEE Nuclear Science Symposium Conference Record (pp. 3247-3249). IEEE. https://doi.org/10.1109/NSSMIC.2011.6152582

Hu, D., Siegel, S. B., Wu, H., Wen, J., Ravindranath, B., & Tai, Y. C. (2011, October). Extending QuickSilver™ electronics for PET insert integration. In 2011 IEEE Nuclear Science Symposium Conference Record (pp. 3247-3249).

IEEE.
https://doi.org/10.1109/NSSMIC.2011.6152582

Innis, R.B., Cunningham, V.J., Delforge, J., Fujita, M., Gjedde, A., Gunn, R.N., Holden, J., Houle, S., Huang, S.C., Ichise, M. and Iida, H., 2007. Consensus nomenclature for in vivo imaging of reversibly binding radioligands. Journal of Cerebral Blood Flow & Metabolism, 27(9), pp.1533-1539.
https://doi.org/10.1038/sj.jcbfm.9600493

Inoue, Y., Momose, T., Ohtake, T., Asai, S., Yoshikawa, K., Nishikawa, J. and Sasaki, Y., 1997. Effect of deadtime loss on quantitative measurement of cerebral blood flow with technetium-99m hexamethylpropylene amine oxime. European journal of nuclear medicine, 24(11), pp.1418-1421. https://doi.org/10.1007/s002590050169

Ishii, Y., Thamm, T., Guo, J., Khalighi, M.M., Wardak, M., Holley, D., Gandhi, H., Park, J.H., Shen, B., Steinberg, G.K. and Chin, F.T., 2020. Simultaneous phase-contrast MRI and PET for noninvasive quantification of cerebral blood flow and reactivity in healthy subjects and patients with cerebrovascular

disease. Journal of Magnetic Resonance Imaging, 51(1), pp.183-194. https://doi.org/10.1002/jmri.26773

Issa, A.S.M., Scheins, J.J., Tellmann, L., Brambilla, C.R., Lohmann, P, Rota-Kops, E, Herzog, H., Neuner, I., Shah, N.J. and Lerche, C.W., 2023. Impact of Improved Dead Time Correction on the Quantification Accuracy of a Dedicated BrainPET Scanner. PLOS ONE,PONE-D-23-17852R1. https://doi.org/10.1371/journal.pone.0296357

Issa, A.S.M., Scheins, J.J., Tellmann, L., Montes, A.L., Herraiz, J.L., Brambilla, C.R., Herzog, H., Neuner, I., Shah, N.J. and Lerche, C.W., 2022. A detector block-pairwise dead time correction method for improved quantitation with a dedicated BrainPET scanner. Physics in Medicine & Biology.https://doi.org/10.1088/136165603

Jiang, W., Chalich, Y. and Deen, M.J., 2019. Sensors for positron emission tomography applications. Sensors, 19(22), p.5019. https://doi.org/10.3390/s19225019

Jung, J. H., Choi, Y., Jung, J., Kim, S., Lim, H. K., Im, K. C., & Kim, J. G. (2015). Development of PET/MRI

with insertable PET for simultaneous PET and MR imaging of human brain. Medical physics, 42(5), 2354-2363. https://doi.org/10.1118/1.4918321

Kanno, I., Miura, S., Yamamoto, S., Iida, H., Murakami, M., Takahashi, K. and Uemura, K., 1985. Design and evaluation of a positron emission tomograph: HEADTOME III. Journal of computer assisted tomography, 9(5), pp.931-939. https://doi.org/10.1097/00004728-198509000-00017

Karas, G.B., Scheltens, P., Rombouts, S.A., Visser, P.J., van Schijndel, R.A., Fox, N.C. and Barkhof, F., 2004. Global and local gray matter loss in mild cognitive impairment and Alzheimer's disease. Neuroimage, 23(2), pp.708-716. https://doi.org/10.1016/j.neuroimage.2004.6

Kemp, B.J., Hruska, C.B., McFarland, A.R., Lenox, M.W. and Lowe, V.J., 2009. NEMA NU 2-2007 performance measurements of the Siemens Inveon™ preclinical small animal PET system. Physics in Medicine & Biology, 54(8), p.2359.https://doi.org/10.1088/00319155/54/8/07

Khalil, M.M. ed., 2011. Basic sciences of nuclear medicine (pp. 155-157). Berlin: Springer.

Knoll, G.F., 2010. Radiation detection and measurement. John Wiley & Sons.

Kolinger, G.D., Vállez García, D., Lohith, T.G., Hostetler, E.D., Sur, C., Struyk, A., Boellaard, R. and Koole, M., 2021. A dual-time-window protocol to reduce acquisition time of dynamic tau PET imaging using [18F] MK-6240. EJNMMI research, 11(1), pp.1-13. https://doi.org/10.1186/s13550-021-00790-x

Kops, E.R., Herzog, H. and Shah, N.J., 2014, December. Comparison template-based with CT-based attenuation correction for hybrid MR/PET scanners. In EJNMMI physics (Vol. 1, No. 1, pp. 1-1). SpringerOpen. https://doi.org/10.1186/2197-7364-1-S1-A47

Kossert, K., Jörg, G. and Gostomski, C.L.V., 2013. Experimental half-life determination of 176Lu. Applied Radiation and Isotopes, 81, pp.140-145. https://doi.org/10.1016/j.apradiso.2013.03.033

Kunz, M., Albert, N.L., Unterrainer, M., la Fougere, C., Egensperger, R., Schüller, U., Lutz, J., Kreth, S., Tonn, J.C., Kreth, F.W. and Thon, N., 2019. Dynamic 18F-FET PET is a powerful imaging biomarker in

gadolinium-negative gliomas. Neuro-oncology, 21(2), pp.274-284. https://doi.org/10.1093/neuonc/noy098

Lage, E., Parot, V., Moore, S. C., Sitek, A., Udías, J. M., Dave, S. R., ... & Herraiz, J. L. (2015). Recovery and normalization of triple coincidences in PET. Medical physics, 42(3), 1398-1410. https://doi.org/10.1118/1.4908226

Lage, E., Parot, V., Moore, S.C., Sitek, A., Udías, J.M., Dave, S.R., Park, M.A., Vaquero, J.J. and Herraiz, J.L., 2015. Recovery and normalization of triple coincidences in PET. Medical physics, 42(3), pp.1398-1410. https://doi.org/10.1118/1.4908226.

Langer, A., 2010. A systematic review of PET and PET/CT in oncology: a way to personalize cancer treatment in a cost-effective manner?. BMC health services research, 10(1), pp.1-16. https://doi.org/10.1186/1472-6963-10-283

Lee, S.H. and Gardner, R.P., 2000. A new G–M counter dead time model. Applied Radiation and Isotopes, 53(4-5), pp.731-737. https://doi.org/10.1016/S0969-8043(00)00261-X

Leo, W.R., 1988. Techniques for nuclear and particle physics experiments. Nucl Instrum Methods Phys Res, 834, p.290.

Lerche, C., Lenz, M., Bi, W., Scheins, J., Tellmann, L., Choi, C. H., & Shah, N. J. (2020). Design and Simulation of a high-resolution and high-sensitivity BrainPET insert for 7T MRI. *Nuklearmedizin-NuclearMedicine*, *59*(02),V96. https://doi.org/10.1055/s-0040-1708248

Lerche, C.W., Radomski, T., Lohmann, P., Caldeira, L., Brambilla, C.R., Tellmann, L., Scheins, J., Kops, E.R., Galldiks, N., Langen, K.J. and Herzog, H., 2021. A Linearized Fit Model for Robust Shape Parameterization of FET-PET TACs. IEEE transactions on medical imaging, 40(7), pp.1852-1862. https://doi.org/10.1109/TMI.2021.3067169

Liu, Y., Tang, S., Wang, J. and Dong, Y., 2019. Dead-time correction method for block detector based ultra-long axial FOV PET scanner. In 2019 IEEE Nuclear Science Symposium and Medical ImagingConference (NSS/MIC) (pp. 1-4). IEEE. https://ieeexplore.ieee.org/stamp/stamp.jsp?arnumber=9059855&casa_token=Sy7aff5kPVwAAAAA:om_asFYypwMSxMyrxvOwOpJAtNfGu3V

us2FPpsq1etkRm35EEt4RDxarGsZK9ljGebZyGrrbtDcb&tag=1

Loening, A.M. and Gambhir, S.S., 2003. AMIDE: a free software tool for multimodality medical image analysis.Molecularimaging,2(3),p.153535002003031333. https://doi.org/10.1162/153535003322556877

Logan, J., 2001. STRATEGIES FOR QUANTIFYING PET IMAGING DATA FROM TRACER STUDIES OF BRAIN RECEPTORS AND ENZYMES (No. BNL-68188; KP140102). Brookhaven National Lab.(BNL), Upton, NY (United States). https://doi.org/10.1002/0470846380.ch17

Lohmann, P., Stavrinou, P., Lipke, K., Bauer, E.K., Ceccon, G., Werner, J.M., Neumaier, B., Fink, G.R., Shah, N.J., Langen, K.J. and Galldiks, N., 2019. FET PET reveals considerable spatial differences in tumour burden compared to conventional MRI in newly diagnosed glioblastoma. European journal of nuclear medicine and molecular imaging, 46(3), pp.591-602. https://doi.org/10.1007/s00259-018-4188-8

Louis, D.N., Perry, A., Reifenberger, G., Von Deimling, A., Figarella-Branger, D., Cavenee, W.K., Ohgaki, H., Wiestler, O.D., Kleihues, P. and Ellison,

D.W., 2016. The 2016 World Health Organization classification of tumors of the central nervous system: a summary. Acta neuropathologica, 131(6), pp.803-820. https://doi.org/10.1007/s00401-016-1545-1

Louis, D.N., Perry, A., Wesseling, P., Brat, D.J., Cree, I.A., Figarella-Branger, D., Hawkins, C., Ng, H.K., Pfister, S.M., Reifenberger, G. and Soffietti, R., 2021. The 2021 WHO classification of tumors of the central nervous system: a summary. Neuro-oncology, 23(8), pp.1231-1251.https://doi.org/10.1093/neuonc/noab106

Maguire, W.J., 1988. Deadtime error with iodine-123 thyroid uptake measurements. Journal of Nuclear Medicine Technology, 16(3), pp.105-108.https://inis.iaea.org/search/search.aspx?orig_q=RN:20026290

Markiewicz, P. J., Ehrhardt, M. J., Erlandsson, K., Noonan, P. J., Barnes, A., Schott, J. M., ... & Ourselin, S. (2018). NiftyPET: a high-throughput software platform for high quantitative accuracy and precision PET imaging and analysis. Neuroinformatics, 16(1), 95-115. https://doi.org/10.1007/s12021-017-9352-y

Markiewicz, P. J., Thielemans, K., Schott, J. M., Atkinson, D., Arridge, S. R., Hutton, B. F., & Ourselin,

S. (2016). Rapid processing of PET list-mode data for efficient uncertainty estimation and data analysis. Physics in Medicine & Biology, 61(13), N322. https://doi.org/10.1088/0031-9155/61/13/N322

Mazoyer, B. M., Roos, M. S., & Huesman, R. H. (1985). Dead time correction and counting statistics for positron tomography. Physics in Medicine & Biology, 30(5), 385. https://doi.org/10.1088/0031-9155/30/5/002

Meechai, T., Tepmongkol, S. and Pluempitiwiriyawej, C., 2015. Partial-volume effect correction in positron emission tomography brain scan image using super-resolution image reconstruction. The British Journal of Radiology, 88(1046), p.20140119. https://doi.org/10.1259/bjr.20140119

Meier, J.G., Erasmus, J.J., Gladish, G.W., Peterson, C.B., Diab, R.H. and Mawlawi, O.R., 2020. Characterization of continuous bed motion effects on patient breathing and respiratory motion correction in PET/CT imaging. Journal of applied clinical medical physics, 21(1), pp.158-165. https://doi.org/10.1002/acm2.12785

Meyer, J.H., Cervenka, S., Kim, M.J., Kreisl, W.C., Henter, I.D. and Innis, R.B., 2020. Neuroinflammation in psychiatric disorders: PET imaging and promising new targets. The Lancet Psychiatry, 7(12), pp.1064-1074. https://doi.org/10.1016/S2215-0366(20)30255-8

Moliner, L., Rodríguez-Alvarez, M. J., Catret, J. V., González, A., Ilisie, V., & Benlloch, J. M. (2019). NEMA performance evaluation of CareMiBrain dedicated brain PET and comparison with the whole-body and dedicated brain PET systems. Scientific reports, 9(1), 1-10. https://doi.org/10.1038/s41598-019-51898-z

Moon, P.B., 1937. Recent developments in Geiger-Müller counters. Journal of Scientific Instruments, 14(6), p.189. https://doi.org/10.1088/0950-7671/14/6/301

Morris, E.D., Endres, C.J., Schmidt, K.C., Christian, B.T., Muzic, R.F. and Fisher, R.E., 2004. Kinetic modeling in positron emission tomography. Emission tomography, 46, pp.499-540.https://doi.org/10.1016/B978-012744482 6.50026-0

Mourik, J.E., Lubberink, M., Van Velden, F.H., Kloet, R.W., Van Berckel, B.N., Lammertsma, A.A. and Boellaard, R., 2010. In vivo validation of reconstruction-based resolution recovery for human brain studies. Journal of Cerebral Blood Flow & Metabolism, 30(2), pp.381-389. https://doi.org/10.1038/jcbfm.2009.225

Müller, J.W., 1973. Dead-time problems. Nuclear Instruments and Methods, 112(1-2), pp.47-57. https://doi.org/10.1016/0029-554X(73)90773-8

Müller, J.W., 1991. Generalized dead times. Nuclear Instruments and Methods in Physics Research Section A: Accelerators, Spectrometers, Detectors and Associated Equipment, 301(3), pp.543-551. https://doi.org/10.1016/0168-9002(91)90021-H

Mutsaerts, H.J., Richard, E., Heijtel, D.F., Van Osch, M.J., Majoie, C.B. and Nederveen, A.J., 2014. Gray matter contamination in arterial spin labeling white matter perfusion measurements in patients with dementia. NeuroImage: Clinical, 4, pp.139-144. https://doi.org/10.1016/j.nicl.2013.11.003

Newport, D. F., Siegel, S. B., Swann, B. K., Atkins, B. E., McFarland, A. R., Pressley, D. R., ... & Nutt, R. E.

(2006, October). QuickSilver: a flexible, extensible, and high-speed architecture for multi-modality imaging. In 2006 IEEE Nuclear Science Symposium Conference Record (Vol. 4, pp. 2333-2334). IEEE. https://doi.org/10.1109/NSSMIC.2006.354381

Nir-El, Y. and Lavi, N., 1998. Measurement of the half-life of 176Lu. Applied Radiation and Isotopes, 49(12), pp.1653-1655.https://doi.org/10.1016/S0969-8043(97)10007-0

Nishikido, F., Fujiwara, M., Tashima, H., Akram, M. S. H., Suga, M., Obata, T., & Yamaya, T. (2017). Development of a full-ring "add-on PET" prototype: a head coil with DOI-PET detectors for integrated PET/MRI. *Nuclear Instruments and Methods in Physics Research Section A: Accelerators, Spectrometers, Detectors and Associated Equipment*, *863*,55-61. https://doi.org/10.1016/j.nima.2017.05.006

Nuyts, J., 2015. Nuclear medicine technology and techniques. KU Leuven: Nuclear Medicine.

Oyama, S., Hosoi, A., Ibaraki, M., McGinnity, C.J., Matsubara, K., Watanuki, S., Watabe, H., Tashiro, M. and Shidahara, M., 2020. Error propagation analysis of

seven partial volume correction algorithms for [18F] THK-5351 brain PET imaging. EJNMMI physics, 7(1), pp.1-15. https://doi.org/10.1186/s40658-020-00324-9

Pál, L., & Pázsit, I. (2012). On some problems in the counting statistics of nuclear particles: Investigation of the dead time problems. Nuclear Instruments and Methods in Physics Research Section A: Accelerators, Spectrometers, Detectors and Associated Equipment, 693, 26-50. https://doi.org/10.1016/j.nima.2012.07.036

Patil, A. and Usman, S., 2009. Measurement and application of paralysis factor for improved detector dead-time characterization. Nuclear technology, 165(2), pp.249-256. https://doi.org/10.13182/NT09-A4090

Patil, A., 2010. Dead time and count loss determination for radiation detection systems in high count rate applications. Missouri University of Science and Technology.

Pélabon, C., Hilde, C.H., Einum, S. and Gamelon, M., 2020. On the use of the coefficient of variation to quantify and compare trait variation. Evolution Letters, 4(3), pp.180-188. https://doi.org/ 10.1002/evl3.171

Ping Li, W., Meyer, L.A., Capretto, D.A., Sherman, C.D. and Anderson, C.J., 2008. Receptor-binding, biodistribution, and metabolism studies of 64Cu-DOTA-cetuximab, a PET-imaging agent for epidermal growth-factor receptor-positive tumors. Cancer biotherapy & radiopharmaceuticals, 23(2), pp.158-171. https://doi.org/10.1089/cbr.2007.0444

Portnow, L. H., Vaillancourt, D. E., & Okun, M. S. (2013). The history of cerebral PET scanning: from physiology to cutting-edge technology. Neurology, 80(10),952–956. https://doi.org/10.1212/WNL.0b013e318285c135

Rajkumar, R., Régio Brambilla, C., Veselinović, T., Bierbrier, J., Wyss, C., Ramkiran, S., Orth, L., Lang, M., Rota Kops, E., Mauler, J. and Scheins, J., 2021. Excitatory–inhibitory balance within EEG microstates and resting-state fMRI networks: assessed via simultaneous trimodal PET–MR–EEG imaging. Translational psychiatry, 11(1), pp.1-15. https://doi.org/10.1038/s41398-020-01160-2

Rausch, I., Zitterl, A., Berroterán-Infante, N., Rischka, L., Prayer, D., Fenchel, M., Sareshgi, R.A., Haug, A.R., Hacker, M., Beyer, T. and Traub-Weidinger, T., 2019. Dynamic [18F] FET-

PET/MRI using standard MRI-based attenuation correction methods. European Radiology, 29(8), pp.4276-4285.

https://doi.org/10.1007/s00330-018-5942-9

Régio Brambilla, C., Veselinović, T., Rajkumar, R., Mauler, J., Matusch, A., Ruch, A., Orth, L., Ramkiran, S., Sbaihat, H., Kaulen, N. and Khudeish, N.Y., 2022. mGluR5 binding changes during a mismatch negativity task in a multimodal protocol with [11C] ABP688 PET/MR-EEG. Translational Psychiatry, 12(1), pp.1-10. https://doi.org/10.1038/s41398-021-01763-3

Régio Brambilla, C., Veselinović, T., Rajkumar, R., Mauler, J., Orth, L., Ruch, A., Ramkiran, S., Heekeren, K., Kawohl, W., Wyss, C. and Kops, E.R., 2020. mGluR5 receptor availability is associated with lower levels of negative symptoms and better cognition in male patients with chronic schizophrenia. Human brain mapping,41(10),pp.2762-2781. https://doi.org/10.1002/hbm.24976

Schaart, D.R., 2021. Physics and technology of time-of-flight PET detectors. Physics in Medicine & Biology,66(9),p.09TR01.https://doi.org/10.1088/1361-6560/abee56

Scheins, J.J., Kops, E.R., Caldeira, L. and Ma, B., 2018. PET Quantification. In Hybrid MR-PET Imaging (pp. 162-182). https://doi.org/10.1039/9781788013062

Schönfeld, E. and Janssen, H., 1994. Precise measurement of dead time. Nuclear Instruments and Methods in Physics Research Section A: Accelerators, Spectrometers, Detectors and Associated Equipment, 339(1-2),pp.137-143.https://doi.org/10.1016/0168-9002(94)91793-0

Schwaiger, M. and Wester, H.J., 2011. How many PET tracers do we need?. Journal of Nuclear Medicine, 52(Supplement2),pp.36S-41S. https://doi.org/10.2967/jnumed.110.085738

Schwarz, M., Franke, S.M., Oberauer, L., Plein, M.D., Steiger, H.T.J. and Tippmann, M., 2019. Measurements of the Lifetime of Orthopositronium in the LAB-Based Liquid Scintillator of JUNO. Nuclear Instruments and Methods in Physics Research Section A: Accelerators, Spectrometers, Detectors and Associated Equipment, 922,pp.64-70. https://doi.org/10.1016/j.nima.2018.12.068

Sehlin, D., Syvänen, S. & on behalf of the MINC faculty. Engineered antibodies: new possibilities for

brain PET?. Eur J Nucl Med Mol Imaging 46, 2848–2858 (2019). https://doi.org/10.1007/s00259-019-04426-0

Shah, N. J., Oros-Peusquens, A. M., Arrubla, J., Zhang, K., Warbrick, T., Mauler, J., ... & Neuner, I. (2013). Advances in multimodal neuroimaging: hybrid MR–PET and MR–PET–EEG at 3 T and 9.4 T. Journal of Magnetic Resonance,229,101-115. https://doi.org/10.1016/j.jmr.2012.11.027

Shepp, L.A. and Vardi, Y., 1982. Maximum likelihood reconstruction for emission tomography. *IEEE transactions on medical imaging*, *1*(2), pp.113-122. https://doi.org/10.1109/TMI.1982.4307558.

Shibuya, K., Saito, H., Nishikido, F., Takahashi, M. and Yamaya, T., 2020. Oxygen sensing ability of positronium atom for tumor hypoxia imaging. Communications Physics,3(1),p.173. https://doi.org/10.1038/s42005-020-00440-z

Siman, W. and Kappadath, S.C., 2017. Comparison of step-and-shoot and continuous-bed-motion PET modes of acquisition for limited-view organ scans. Journal of

nuclear medicine technology, 45(4), pp.290-296. https://doi.org/10.2967/jnmt.117.195438

Slifstein, M. and Laruelle, M., 2001. Models and methods for derivation of in vivo neuroreceptor parameters with PET and SPECT reversible radiotracers. Nuclear medicine and biology, 28(5), pp.595-608.https://doi.org/10.1016/S0969-8051(01)00214-1

Takacs, L., 1958. On a probability problem in the theory of counters. The Annals of Mathematical Statistics,29(4),pp.1257-1263. https://doi.org/10.1214/aoms/1177706457

Teimoorisichani, M., & Goertzen, A. L. (2018). Geometry optimization of a dual-layer offset detector for use in simultaneous PET/MR neuroimaging. IEEE Transactions on Radiation and Plasma Medical Sciences,3(3),275-284. https://doi.org/10.1109/TRPMS.2018.2864923

Theodorakis, L., Loudos, G., Prassopoulos, V., Kappas, C., Tsougos, I. and Georgoulias, P., 2013. A review of PET normalization: striving for count rate uniformity. Nuclear medicine communications, 34(11), pp.1033-

1045.
https://doi.org/10.1097/MNM.0b013e328365ac1e

Thie, J.A., 2004. Understanding the standardized uptake value, its methods, and implications for usage. Journal of Nuclear Medicine, 45(9), pp.1431-1434. PMID: 15347707

Toga, A.W., Mazziotta, J.C. and Mazziotta, J.C. eds., 2002. Brain mapping: the methods (Vol. 1). Academic press.

Ullisch, M.G. and Moses, W.W., 2007. Multi-CFD timing estimators for PET block detectors. IEEE Transactions on Nuclear Science, 54(1), pp.55-59. https://doi.org/doi: 10.1109/TNS.2006.889171.

Uribe, C.F., Esquinas, P.L., Gonzalez, M., Zhao, W., Tanguay, J. and Celler, A., 2018. Deadtime effects in quantification of 177 Lu activity for radionuclide therapy. EJNMMI physics, 5, pp.1-16. https://doi.org/10.1186/s40658-017-0202-7

Usman, S. and Patil, A., 2018. Radiation detector deadtime and pile up: A review of the status of science. Nuclear Engineering and Technology, 50(7), pp.1006-1016. https://doi.org/10.1016/j.net.2018.06.014

van Velden, F.H., Kloet, R.W., van Berckel, B.N., Wolfensberger, S.P., Lammertsma, A.A. and Boellaard, R., 2008. Comparison of 3D-OP-OSEM and 3D-FBP reconstruction algorithms for High-Resolution Research Tomograph studies: effects of randoms estimation methods. Physics in Medicine & Biology, 53(12), p.3217. https://doi.org/10.1088/0031-9155/53/12/010

Veenith, Tonny & Menon, David. (2011). The cerebral circulation. https://doi.org/10.1017/CBO9780511977558.003

Vicente, E., Espana, S., Herraiz, J.L., Herranz, E., Desco, M., Vaquero, J.J. and Udias, J.M., 2008, October. Nonlinear effect of pile-up in the quantification of a small animal PET scanner. In 2008 IEEE Nuclear Science Symposium Conference Record (pp. 5391-5395). IEEE. https://doi.org/10.1109/NSSMIC.2008.4774451

Vicente, E., Herraiz, J.L., Espana, S., Herranz, E., Desco, M., Vaquero, J.J. and Udias, J.M., 2011, October. Deadtime and pile-up correction method based on the singles to coincidences ratio for PET. In 2011 IEEE Nuclear Science Symposium Conference Record (pp. 2933-2935).

IEEE.
https://doi.org/10.1109/NSSMIC.2011.6152523

Vicente, E., Herraiz, J.L., España, S., Herranz, E., Desco, M., Vaquero, J.J. and Udías, J.M., 2013. Improved dead-time correction for PET scanners: application to small-animal PET. *Physics in Medicine & Biology*, *58*(7),p.2059.
https://doi.org/10.1088/00319155/58/7/209

Vigneswaran, K., Neill, S. and Hadjipanayis, C.G., 2015. Beyond the World Health Organization grading of infiltrating gliomas: advances in the molecular genetics of glioma classification. Annals of translationalmedicine,3(7).
https://doi.org/10.3978/j.issn.2305-5839.2015.03.57

Wang, Q., Mikhaylova, E., Baikejiang, R. and Cherry, S.R., 2020. The reduction of 176Lu background in Lu-based PET scanners using optimized classification. Physics in Medicine & Biology, 65(17), p.175016. https://doi.org/10.1088/1361-6560/aba088

Wang, Z., Wu, Y., Li, X., Bai, Y., Chen, H., Ding, J., Shen, C., Hu, Z., Liang, D., Liu, X. and Zheng, H., 2022. Comparison between a dual-time-window

protocol and other simplified protocols for dynamic total-body 18F-FDG PET imaging. EJNMMI physics, 9(1), pp.1-17. https://doi.org/10.1186/s40658-022-00492-w

Wei, Q. (2015). Intrinsic radiation in lutetium based PET detector: Advantages and disadvantages. arXiv preprint arXiv:1501.05372. https://doi.org/10.48550/arXiv.1501.05372

Weirich, C., Brenner, D., Scheins, J., Besancon, É., Tellmann, L., Herzog, H., & Shah, N. J. (2012). Analysis and correction of count rate reduction during simultaneous MR-PET measurements with the BrainPET scanner. IEEE transactions on medical imaging,31(7),1372-1380. https://doi.org/10.1109/TMI.2012.2188903

Weirich, C., Scheins, J., Gaens, M., Herzog, H., & Shah, N. J. (2013). Combined Deadtime and Pile-up correction for the MR-compatible BrainPET Scanner. In 2013 IEEE Nuclear Science Symposium and Medical Imaging Conference (2013 NSS/MIC) (pp. 1-2).IEEE. https://doi.org/10.1109/NSSMIC.2013.6829401

Weirich, C., Scheins, J., Lohmann, P., Tellmann, L., Byars, L., Michel, C., Kops, E.R., Brenner, D., Herzog, H. and Shah, N.J., 2013. Quantitative PET imaging with the 3T MR-BrainPET. Nuclear Instruments and Methods in Physics Research Section A: Accelerators, Spectrometers, Detectors and Associated Equipment, 702,pp.26-28. https://doi.org/10.1016/j.nima.2012.08.068

Wilke, M., Krägeloh-Mann, I. and Holland, S.K., 2007. Global and local development of gray and white matter volume in normal children and adolescents. Experimental Brain Research, 178, pp.296-307. https://doi.org/10.1007/s00221-006-0732-z

Xu, G., Rowley, H.A., Wu, G., Alsop, D.C., Shankaranarayanan, A., Dowling, M., Christian, B.T., Oakes, T.R. and Johnson, S.C., 2010. Reliability and precision of pseudo-continuous arterial spin labeling perfusion MRI on 3.0 T and comparison with 15O-water PET in elderly subjects at risk for Alzheimer's disease. *NMR in Biomedicine*, *23*(3), pp.286-293. https://doi.org/10.1002/nbm.1462

Yamamoto, S., Amano, M., Miura, S., Iida, H., & Kanno, I. (1986). Deadtime correction method using random coincidence for PET. Journal of nuclear

medicine,27(12),1925-1928. https://jnm.snmjournals.org/content/jnumed/27/12/1925.full.pdf

Yang, J., Hu, C., Guo, N., Dutta, J., Vaina, L.M., Johnson, K.A., Sepulcre, J., Fakhri, G.E. and Li, Q., 2017. Partial volume correction for PET quantification and its impact on brain network in Alzheimer's disease. Scientific reports,7(1),pp.1-14. https://doi.org/10.1038/s41598-017-13339-7

Yu, X., Zhang, X., Zhang, H., Peng, H., Ren, Q., Xu, J., Peng, Q. and Xie, S., 2022. Requirements of Scintillation Crystals with the Development of PET Scanners. Crystals, 12(9), p.1302. https://doi.org/10.3390/cryst12091302

Zaidi, H. (Ed.). (2006). *Quantitative analysis in nuclear medicine imaging*. Springer Science & Business Media.

Zaidi, H. and Montandon, M.L., 2007. Scatter compensation techniques in PET. PET clinics, 2(2), pp.219-234. https://doi.org/10.1016/j.cpet.2007.10.003

Zaidi, H., 2006. Recent developments and future trends in nuclear medicine instrumentation. Zeitschrift für Medizinische Physik, 16(1), pp.5-17. https://doi.org/10.1078/0939-3889-00288

Zaidi, H., Montandon, M.L. and Alavi, A., 2007. Advances in attenuation correction techniques in PET. PET clinics, 2(2), pp.191-217. https://doi.org/10.1016/j.cpet.2007.12.002

Zgardzińska, B., Chołubek, G., Jarosz, B., Wysogląd, K., Gorgol, M., Goździuk, M., Chołubek, M. and Jasińska, B., 2020. Studies on healthy and neoplastic tissues using positron annihilation lifetime spectroscopy and focused histopathological imaging. Scientific Reports, 10(1), p.11890. https://doi.org/10.1038/s41598-020-68727-3

Zhang, K., Herzog, H., Mauler, J., Filss, C., Okell, T.W., Kops, E.R., Tellmann, L., Fischer, T., Brocke, B., Sturm, W. and Coenen, H.H., 2014. Comparison of cerebral blood flow acquired by simultaneous [15O] water positron emission tomography and arterial spin labeling magnetic resonance imaging. *Journal of cerebral blood flow & metabolism*, *34*(8), pp.1373-1380. https://doi.org/10.1038/jcbfm.2014.92

Zhang, N., Grazioso, R. F., Doshi, N. K., Corbeil, J. L., & Schmand, M. J. (2006, November). Quarter-trio mapping electronics readout scheme for APD block

detector in PET. In 2006 IEEE Nuclear Science Symposium Conference Record (Vol. 3, pp. 1912-1914).IEEE. https://doi.org/10.1109/NSSMIC.2006.354268.

8. Appendix

Table A.1 Dead time constants of the all blocks (192) in the BrainPET detector.

Block ID	1	2	3	4	5	6
Dead Time[ns]	205	203	202	199	209	216
Block ID	7	8	9	10	11	12
Dead Time[ns]	208	200	203	210	208	209
Block ID	13	14	15	16	17	18
Dead Time[ns]	204	202	203	200	198	204
Block ID	19	20	21	22	23	24
Dead Time[ns]	209	205	207	185	209	219
Block ID	25	26	27	28	29	30
Dead Time[ns]	214	217	210	209	212	231
Block ID	31	32	33	34	35	36
Dead Time[ns]	210	209	211	221	218	214
Block ID	37	38	39	40	41	42
Dead Time[ns]	200	201	201	202	199	198
Block ID	43	44	45	46	47	48
Dead Time[ns]	198	196	195	195	196	197
Block ID	49	50	51	52	53	54
Dead Time[ns]	201	201	198	195	194	196
Block ID	55	56	57	58	59	60
Dead Time[ns]	195	193	195	196	197	191
Block ID	61	62	63	64	65	66

Dead Time[ns]	188	187	191	187	190	186
Block ID	67	68	69	70	71	72
Dead Time[ns]	187	185	190	192	189	189
Block ID	73	74	75	76	77	78
Dead Time[ns]	195	194	194	192	192	191
Block ID	79	80	81	82	83	84
Dead Time[ns]	193	192	193	194	193	189
Block ID	85	86	87	88	89	90
Dead Time[ns]	188	188	190	187	188	182
Block ID	91	92	93	94	95	96
Dead Time[ns]	182	184	188	186	186	176
Block ID	97	98	99	100	101	102
Dead Time[ns]	187	189	189	188	186	184
Block ID	103	104	105	106	107	108
Dead Time[ns]	192	190	189	189	188	179
Block ID	109	110	111	112	113	114
Dead Time[ns]	190	190	191	190	190	186
Block ID	115	116	117	118	119	120
Dead Time[ns]	190	187	188	189	188	184
Block ID	121	122	123	124	125	126
Dead Time[ns]	183	187	187	187	183	179
Block ID	127	128	129	130	131	132
Dead Time[ns]	189	186	183	184	184	182
Block ID	133	134	135	136	137	138

Dead Time[ns]	192	189	191	188	193	192
Block ID	139	140	141	142	143	144
Dead Time[ns]	193	191	196	194	195	192
Block ID	145	146	147	148	149	150
Dead Time[ns]	190	191	191	188	187	185
Block ID	151	152	153	154	155	156
Dead Time[ns]	193	191	194	193	194	187
Block ID	157	158	159	160	161	162
Dead Time[ns]	200	200	207	199	203	210
Block ID	163	164	165	166	167	168
Dead Time[ns]	208	200	202	200	201	200
Block ID	169	170	171	172	173	174
Dead Time[ns]	200	201	201	201	201	203
Block ID	175	176	177	178	179	180
Dead Time[ns]	202	202	202	199	196	194
Block ID	181	182	183	184	185	186
Dead Time[ns]	195	196	196	196	196	199
Block ID	187	188	189	190	191	192
Dead Time[ns]	196	195	194	194	195	194

Figures. A.1 and A.2 show the time-dependent of the [^{18}F]-FET-PET TBR_{max} and TBR_{mean} between the global and the block-pairwise DTC methods.

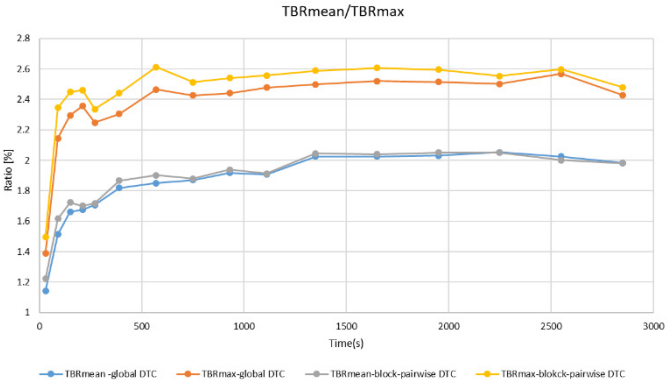

Figure A.1 Time-dependent of the [^{18}F]-FET-PET TBR_{max} and TBR_{mean} between the global and the block-pairwise DTC methods.

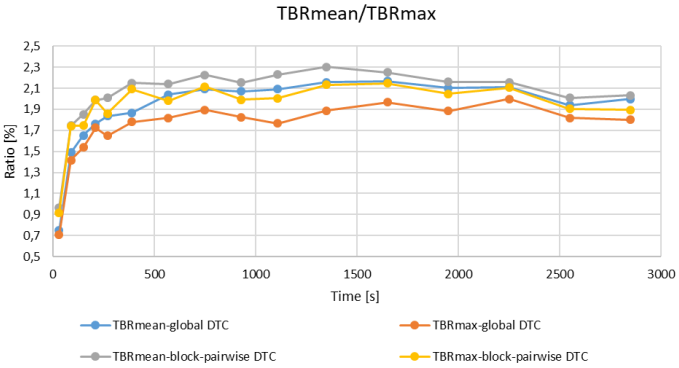

Figure A.2 Time-dependent of the [^{18}F]-FET-PET TBR_{max} and TBR_{mean} between the global and the block-pairwise DTC methods.

LIST OF PUBLICATIONS

1. **Issa, A.S.M.,** Scheins, J.J., Tellmann, L., Montes, A.L., Herraiz, J.L., Brambilla, C.R., Herzog, H., Neuner, I., Shah, N.J. and Lerche, C.W., 2022. A detector block-pairwise dead time correction method for improved quantitation with a dedicated BrainPET scanner. Physics in Medicine & Biology. https://doi.org/10.1088/1361-6560/aca1f3
2. **Issa, A.S.M.,** Scheins, J.J., Lutz Tellmann, Cláudia Régio Brambilla, Philipp Lohmann, Elena Rota-Kops, Hans Herzog, Irene Neuner, N. Jon Shah, and Christoph Lerche, as Impact of Improved Dead Time Correction on the Quantification Accuracy of a Dedicated BrainPET Scanner. PLOS ONE.
   https://doi.org/10.1371/journal.pone.0296357
3. Brambilla, C.R., Scheins, J., **Issa, A.,** Tellmann, L., Herzog, H., Rota Kops, E., Shah, N.J., Neuner, I. and Lerche, C.W., 2021. Bias evaluation and reduction in 3D OP-OSEM reconstruction in dynamic equilibrium PET studies with 11C-labeled for binding potential analysis. PloS one, 16(1), p.e0245580.
   https://doi.org/10.1371/journal.pone.0245580

4. Li, C., Scheins, J., Tellmann, L., **Issa, A.,** Wei, L., Shah, N.J. and Lerche, C., 2023. Fast 3D kernel computation method for positron range correction in PET. Physics in Medicine & Biology, 68(2), p.025004. https://doi.org/10.1088/1361-6560/acaa84

5. Régio Brambilla, C., Scheins, J., Tellmann, L., **Issa, A.,** Herzog, H., Shah, N.J., Neuner, I. and Lerche, C.W., 2023. Impact of framing scheme optimization and smoking status on binding potential analysis in dynamic PET with [11C] ABP688. EJNMMI research, 13(1), p.11. https://doi.org/10.1186/s13550-023-00957-8

6. **A. Issa ,** J. Scheins , L. Tellmann , C. Régio Brambilla, H. Xu , N. Shah, C. Lerche. Comparing the accuracy of global and blockwise deadtime correction for the BrainPET scanner. European Association of Nuclear Medicine. October 22 – 30, 2020.VirtualAbstracts. https://link.springer.com/content/pdf/10.1007/s00259-020-04988-4.pdf

7. **A. S. M. Issa**, L. Tellmann, J. Scheins, A. L. -Montes, J. L. Herraiz, N. J. Shah, C. Lerche. Deadtime Correction Method Using Random Coincidences in Block-Pairs for the Siemens 3T

MR/BrainPET Scanner. Poster Presentation & Oral Presentation. 2021 VIRTUAL IEEE NUCLEAR SCIENCE SYMPOSIUM AND MEDICAL IMAGINGCONFERENCE. https://www.eventclass.org/contxt_ieee2021/onlineprogram/search?search=Deadtime+Correction+Method+Using+Random+Coincidences+in+Block-Pairs+for+the+Siemens+3T+MR BrainPET+Scanner

8. **Ahlam S.M. Issa**, Jürgen Scheins, Lutz Tellmann, Philipp Lohmann, N. Jon Shah, Christoph Lerche. Improved Deadtime Correction Method Using Random Coincidences in Block-Pairs for the Siemens 3T MR/Brain PET Scanner. Accepted Abstract in 2022 IEEE Nuclear Science Symposium, Medical Imaging Conference and Room Temperature Semiconductor Detector Conference. 5 – 12 November 2022, Milano, Italy.

ACKNOWLEDGEMENT

I would like to express my deepest gratitude to the Palestinian-German Science Bridge (PGSB) to support this work by the German Federal Ministry of Education and Research (BMBFgrant 01DH16027), and to all others who provided support during my scholarship. I'm extremely grateful to Prof. Dr. N. Jon Shah for allowing me to carry out this project and be a member of the INM4 and for providing continuous support. This endeavor would not have been possible without Dr. Christoph W. Lerche, who always provided outstanding supervision and continuous support during this project, he was the featured teacher & supervisor for productive work. These words cannot express my gratitude to Prof. Dr. Hans Herzog & Prof. Dr. Irene Neuner for providing continuous support and help in data processing, and discussions about data analysis. I am deeply indebted to the PET Physics group, I would like to thank Dr. Jürgen Scheins for his support in data reconstruction and correction. I would like to thank

Dr. Cláudia Régio Brambilla for her support and help with data processing issues, discussions about [^{11}C]ABP688 measurements, and kinetic modeling. I am grateful to Mr. Lutz Tellmann for his help in the measurements and data acquisition. I would like to thank Dr. Philipp Lohmann for his help in the data processing. I could not have undertaken this journey without the nice support from Prof. Dr. Ghaleb Natour & Dr. Caitlin Morgan.

Affidavit according to § 5 (1) for Data Retention

I hereby declare that the original data forming the basis of this doctoral thesis are stored with my supervisor, Prof. Dr. N. Jon Shah, head of the "Institute of Neuroscience and Medicine (INM-4)", Forschungszentrum Jülich, Department of Neurology, Faculty of Medicine, RWTH Aachen University, Aachen, JARA - BRAIN - Translational medicine, Aachen. Institute of Neuroscience and Medicine 11, INM-11, JARA, Forschungszentrum Jülich, Germany, and Prof. Dr. med. Irene Neuner, Clinic for Psychiatry, Psychotherapy and Psychosomatics, University Hospital Aachen.

Ahlam Said Mohamad Issa

Affidavit according to § 5 (1) § 11 (3) 12 of the doctoral studies regulations

I, **Ahlam Said Mohamad Issa,** hereby declare on oath that I independently collected and prepared the following results portrayed in the dissertation "**A Detector Block-Pairwise Dead Time Correction Method for Improved Quantitation Accuracy for a Dedicated BrainPET Scanner**",
I had the following assistance with completing the dissertation

Names-→	Candidate (Ahlam S. M. Issa)	Practical supervisor/ (Lerche)	Collaborative group Nuclear Physics Group and IPARCOS (Lopez-Montes, L Herraiz)	Collaborative scientists (Scheins, Régio Brambilla, Herzog, Lohmann)	Assistant (Tellman)	Doctoral supervisor (Shah & Neuner)	Sum (%)
Study supervision		50				50	100
Study design/conception	50	30	5	5		10	100
Examination of the study participants	50	10		30	10		100
Data evaluation	100						100
Performing experiments of PET	80				20		100
Statistical evaluation	100						100
Delivery of materials		10			10	80	100

Interpretation of data evaluation	70	20				10	100
Writing the draft	100						100
Correction of the draft	40	40				20	

Ahlam Said Mohamad Issa

Signature of the doctoral candidate

As the supervisor of the above dissertation, I confirm the statements of [**Ahlam Said Mohamad Issa**].

Prof. Dr. rer. nat. Nadim Joni Shah

_____

Signature of the doctoral supervisor